

**RHODES UNIVERSITY**



**Observing cosmic reionization with  
PAPER: polarized foreground simulations  
and all sky images**

by

**Chuneeta Devi Nunhokee**

Submitted in fulfillment of the  
academic requirements for the degree of

Doctor of Philosophy

in

Physics

Rhodes University, Grahamstown

Supervised by Prof. G. Bernardi & Prof. O. M. Smirnov

March 2018

*Now unto him that is able to do exceeding abundantly above all that we ask or think, according to the power that worketh in us.*

*~Ephesians 3:20*

*For in him we live and move and have our being.*

*~Acts 17:28*

---

## Declaration of Non-Plagiarism

---

I, **Chuneeta Devi Nunhokee** declare that

1. The research reported in this thesis, except where otherwise indicated, is my original research.
2. This thesis has not been submitted for any degree or examination at any other university.
3. This thesis does not contain other persons' data, pictures, graphs or other information, unless specifically acknowledged as being sourced from other persons.
4. This thesis does not contain other persons' writing, unless specifically acknowledged as being sourced from other researchers.

---

## Publication List

---

Publications that form part and/or include research presented in this thesis:

1. Nunhokee, C. D., Bernardi, G., Kohn, S. A., Aguirre, J. E. et al., *Constraining Polarized Foregrounds for EoR Experiments. II. Polarization Leakage Simulations in the Avoidance Scheme*. The Astrophysical Journal, volume 484, 47, 2017.
2. Nunhokee, C. D., Bernardi, G. and PAPER collaboration, *All-sky Imaging with PAPER-128*, in preparation.

Publications resulting from work done in collaboration with other institutes:

1. Kohn, S. A., Aguirre, J. E., Nunhokee, C. D., Bernardi, G. et al., *Constraining Polarized Foregrounds for EoR Experiments I: 2D Power Spectra from the PAPER-32 Imaging Array*. The Astrophysical Journal, volume 823,88, 2016.
2. Dillon, J. S., Kohn, S. A., Parsons, A. R., Aguirre, J. E. et al., *Polarized Redundant-Baseline Calibration for 21 cm Cosmology Without Adding Spectral Structure*, ArXiv e-prints, arXiv:1712.07212.

---

## Abstract

---

*T*he Donald C. Backer Precision Array to Probe the Epoch of Reionization (PAPER, [Parsons et al., 2010](#)) was built with an aim to detect the redshifted 21 cm Hydrogen line, which is likely the best probe of thermal evolution of the intergalactic medium and reionization of neutral Hydrogen in our Universe. Observations of the 21 cm signal are challenged by bright astrophysical foregrounds and systematics that require precise modeling in order to extract the cosmological signal. In particular, the instrumental leakage of polarized foregrounds may contaminate the 21 cm power spectrum. In this work, we developed a formalism to describe the leakage due to instrumental widefield effects in visibility-based power spectra and used it to predict contaminations in observations. We find the leakage due to a population of point sources to be higher than the diffuse Galactic emission – for which we can predict minimal contaminations at  $k > 0.3 h \text{ Mpc}^{-1}$ . We also analyzed data from the last observing season of PAPER via all-sky imaging with a view to characterize the foregrounds. We generated an all-sky catalogue of 88 sources down to a flux density of 5 Jy. Moreover, we measured both polarized point source and the Galactic diffuse emission, and used these measurements to constrain our model of polarization leakage. We find the leakage due to a population of point sources to be 12% lower than the prediction from our polarized model.

---

## Acknowledgments

---

*“The Lord is my strength and my shield; My heart trusts in Him, and I am helped ~Psalms 28:7”*

*T*his note of thanks is the final touch on my dissertation dedicated to all those whose paths have crossed mine. I would like to reflect on the people who supported and helped me throughout my PhD journey.

I begin by thanking Gianni –throughout these three years, you have been not only a wonderful supervisor but also a marvelous person who always motivated me to look at the bigger picture and nurture the scientist in me with your calm demeanor and patience. I thank Oleg for believing in my academic skills without whom I would not have made it to South Africa. I also thank my colleagues – Griffin, Theo, Marcel, Arun, Ulrich, Kshitij and Trienko for their selfless helping attitude and great company during my stay in Grahamstown. I thank Mrs. Ronel Groenewald for making most of my paperworks appear extremely easy with her efficient management skills. I extend a special vote of thanks to the faculty and staff of the Physics and Electronics Department. Carina and Saul have been excellent companions on the analysis of the PAPER data. I thank James Aguirre for giving me the opportunity to work alongside him, it had been a great pleasure. I am grateful to the PAPER collaboration for their thoughtful insights. Jon and Cynthia –thank you for believing in my software skills and giving me the amazing opportunity to be part of

the deployment team of PRI<sup>Z</sup>M. I thank Sookia, my honors supervisor who believed in me and encouraged me to pursue higher studies and Dinesh for introducing me to one of the happening research fields. I thank SKA-SA for funding my studies.

Apart from academia, I am extremely grateful towards my loving family –mom, dad and brothers who backed me up all the times and helped me sail smoothly. My late grandfather Chandreeka and uncle Deoraj –I miss you guys, I still remember your glowing faces and encouraging speeches after hitting a milestone. Lee –you have been a blessing to me since the very first day we met, you always brought the best in me. Your constant encouragement and belief in me never let me give up! I thank Selven, Shandiv, Daryl and Veer for their constant love and support, genuine individuals on whom I can blindly fall on.

And above everything and everyone – I am grateful towards the Almighty for all His blessings in my life, and I conclude by saying – *the LORD has done this, and it is marvelous in our eyes.*  
~*Psalm 118:23.*

---

# Contents

---

<b>Declaration of Non Plagiarism</b>	<b>i</b>
<b>Declaration of Publications</b>	<b>ii</b>
<b>Abstract</b>	<b>iii</b>
<b>Acknowledgments</b>	<b>iv</b>
<b>1 Introduction</b>	<b>1</b>
1.1 Cosmic History . . . . .	1
1.2 The 21 cm hyperfine Hydrogen line . . . . .	3
1.3 Cosmic evolution of the 21 cm signal . . . . .	4
1.4 Fluctuations in the 21 cm signal . . . . .	6
1.5 Current observational status . . . . .	10
<b>2 Challenges of 21 cm experiments and thesis motivation</b>	<b>12</b>
2.1 Foreground Emission . . . . .	12
2.2 Foreground Separation . . . . .	16

2.2.1	Foreground Subtraction . . . . .	16
2.2.2	Foreground Avoidance . . . . .	17
2.3	Polarization Leakage . . . . .	21
2.3.1	Polarized Foregrounds . . . . .	22
<b>3</b>	<b>Constraining polarized foregrounds for EoR experiments: polarization leakage simulations in the avoidance scheme</b>	<b>27</b>
3.1	Formalism . . . . .	28
3.2	Simulations . . . . .	31
3.2.1	Point source all-sky model . . . . .	34
3.2.2	Galactic diffuse emission model . . . . .	37
3.3	Results . . . . .	39
3.3.1	Polarized Power Spectra . . . . .	40
3.3.2	Predictions of polarization leakage . . . . .	42
3.3.3	Constraining the polarization fraction . . . . .	46
3.4	Discussion and Conclusions . . . . .	48
<b>4</b>	<b>All-sky Imaging with PAPER-128</b>	<b>52</b>
4.1	Array configuration and data acquisition . . . . .	52
4.2	Flagging and calibration . . . . .	55
4.2.1	Absolute flux calibration . . . . .	59
4.3	All-sky images . . . . .	63
4.3.1	Rotation Measure synthesis . . . . .	70
4.4	Results . . . . .	77
4.4.1	Source Catalogue . . . . .	77
4.4.2	Point source polarization analysis . . . . .	79
4.5	Discussions and Conclusions . . . . .	82
<b>5</b>	<b>General conclusions</b>	<b>86</b>

# CHAPTER 1

---

## Introduction

---

Our understanding of cosmology has evolved significantly in the last two decades. The “concordance model”: a model with only six parameters can be used to describe the vast majority of the universe from its infancy, 13.7 billion years ago, through to its present state (Figure 1.1). Observations of the Cosmic Microwave Background radiation (CMB; [Planck Collaboration, 2015](#)), the large scale structures ([Tegmark et al., 2006](#)) and the baryonic acoustic oscillations ([Seo & Eisenstein, 2005](#)) are some of the best available probes to date that follows this model.

## 1.1 Cosmic History

In this section we discuss the cosmic evolution in a chronological order from its beginning to the present state as described in [Carroll & Ostlie \(1996\)](#) and [Bennett et al. \(2005\)](#).

Approximately  $10^{-43}$  seconds after the big bang, the temperature of the Universe was about  $10^{32}$  K and gravitational, electromagnetic, weak and strong nuclear interactions existed as a combined force ([Bennett et al., 2005](#)). Gravity then started to separate from all the other forces and elementary particles and anti-particles were created. The unification of all the basic forces

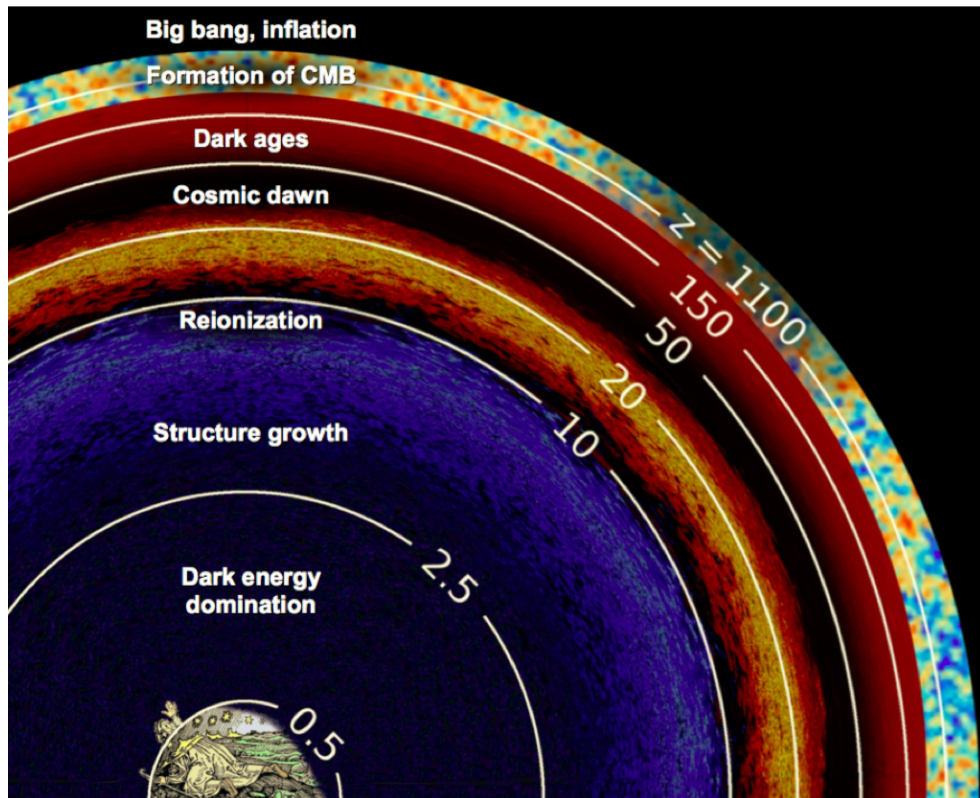


Figure 1.1: Timeline of the Universe's evolution with some of the milestones highlighted.

but gravity is referred to as the Grand Unified Theory (GUT; [Lyth & Stewart, 1995](#); [Kolb et al., 1996](#)). At  $t = 10^{-38}$  seconds, GUT predicts that the temperature had cooled down to  $10^{27}$  K when the strong nuclear force separated from the electroweak interaction. This force separation triggered cosmic inflation ([Linder, 1990](#); [Linde, 2008](#)) and consequently the Universe grew in size by a factor of  $10^{50}$  from  $t = 10^{-36}$  seconds to  $t = 10^{-32}$  seconds. The electroweak era lasted till  $t = 10^{-12}$  seconds ([Sather, 1996](#); [Rafelski & Birrell, 2014](#)) when the temperature dropped from  $10^{15}$  to  $10^{13}$  K and elementary particles (photons, gluons and quarks) were formed ([Kajantie & Kurki-Suonio, 1986](#); [Fuller et al., 1988](#); [Kolb & Turner, 1994](#); [Rafelski & Birrell, 2014](#)), and the electroweak force split into electromagnetic and weak nuclear force. Eventually, the four fundamental forces that govern all the processes in the Universe were separated from each other.

At  $t = 10^{-6}$  seconds, the temperature is estimated to be between  $10^{13}$  to  $10^{10}$  K, sufficiently low to allow baryogenesis. Nucleosynthesis began when the Universe was  $\sim 1$  second old, lasting

for  $\sim 17$  minutes (Fuller et al., 1988; Mathews et al., 1990; Malaney & Mathews, 1993), when the temperature dropped to  $10^7$  K. Photons and baryons remained tightly coupled till the Universe was  $\sim 380000$  years old, and the temperature was  $\sim 3000$  K, allowing electrons and protons to combine and form neutral Hydrogen (Kamionkowski, 2007). Radiation was now able to move freely after decoupling from matter, and the Universe became transparent. This relic radiation is known as the Cosmic Microwave Background (CMB; Planck Collaboration, 2015; Planck Collaboration et al., 2016a,b).

The first luminous sources likely formed only  $\sim 150$  million years afterwards (e.g., Yoshida et al., 2012; Bromm, 2013; Jeon, 2015) as very massive stars. These early massive stars emitted a background of ultraviolet radiation that, eventually, escaped the host galaxies and began to ionize the Hydrogen in the surrounding intergalactic medium (IGM). This phase transition is called the Epoch of Reionization (EoR; e.g., Zaroubi, 2013). The bubbles of ionized Hydrogen (HII) grew bigger until they merged with each other, eventually ionizing the IGM completely.

Evidences of cosmic reionization come from observations of the Gunn-Peterson trough towards distant quasars (Fan et al., 2006; Becker et al., 2015; Mortlock, 2015), the Ly $\alpha$  dropout in high-redshift galaxies (Stark et al., 2011; Dijkstra, 2014; Pentericci et al., 2014) and large scale CMB polarization anisotropies (Planck Collaboration et al., 2016a,b). The 21 cm hyperfine line from neutral Hydrogen (HI) is, however, the most promising tool to study reionization as it directly probes the evolution of the IGM (Madau et al., 1997; Barkana & Loeb, 2001; Furlanetto et al., 2006). In the next section, we will present a theoretical summary of the 21 cm line in the cosmological context.

## 1.2 The 21 cm hyperfine Hydrogen line

The energy difference between the proton-electron symmetric (hyperfine) and anti-symmetric configurations of the HI atom is radiated as a spectral line with a rest-frame wavelength of approximately 21 cm, or 1421 MHz. If emitted by a  $z > 6$  cloud, the 21 cm line is redshifted to frequencies  $\nu < 200$  MHz. The brightness temperature  $T_b$  of such a cloud can be expressed as

(Furlanetto et al., 2006):

$$\delta T_b(\nu) \approx 27 x_{\text{HI}} \left[ 1 - \frac{T_{\text{CMB}}(z)}{T_s} \right] (1 + \delta) \left[ \frac{H(z)/(1+z)}{d\nu_r/dr} \right] \left[ \frac{1+z}{10} \frac{0.15}{\Omega_M h^2} \right]^{1/2} \left[ \frac{\Omega_b h^2}{0.023} \right] \left[ \frac{1 - Y_p}{0.75} \right] \text{mK} \quad (1.1)$$

where  $x_{\text{HI}}$  is the HI neutral fraction,  $T_s$  is the 21 cm spin temperature that drives the population of the excited hyperfine level,  $T_{\text{CMB}}$  is the CMB temperature,  $\delta$  is the matter density contrast,  $d\nu_r/dr$  is the comoving gradient of the line of sight velocity component,  $H(z)$  is the Hubble constant,  $Y_p$  is the Helium mass fraction, and  $\Omega_M$  and  $\Omega_b$  are the matter and baryon density parameters respectively.

The 21 cm signal from neutral Hydrogen is therefore observable only if  $T_s \neq T_{\text{CMB}}$ , or, in other words, if it is coupled to the gas kinetic temperature  $T_k$ , which is the other variable at play. There are two mechanisms that can couple the spin temperature to the gas temperature. When the Universe's gas density is sufficiently high, collisions amongst atoms induce spin flip transitions that set  $T_s = T_k$ . The second coupling mechanism is known as the Wouthuysen-Field effect (Wouthuysen, 1952; Field, 1959) and is illustrated in Figure 1.2. When a Hydrogen atom in its singlet state ( $1S$ ) absorbs a  $\text{Ly}\alpha$  photon, it jumps to either of the  $2P$  states. However, when the electron decays to lower energy levels, the atom may not return to the hyperfine singlet ( $1_1S_{\frac{1}{2}}$ ) state but, instead, may emit a longer wavelength photon and transition to the hyperfine triplet state ( $1_0S_{\frac{1}{2}}$ ). Thus, Hydrogen atoms can change their hyperfine state through the absorption and spontaneous re-emission of  $\text{Ly}\alpha$  photons.

### 1.3 Cosmic evolution of the 21 cm signal

A fiducial model of the evolution of the spatially averaged (global) 21 cm signal is displayed in Figure 1.3. Different redshift ranges encode different physical IGM properties and we will briefly describe them as follows:

- $200 > z > 30$ : Before  $z \sim 200$ , Compton scattering kept the gas tightly coupled to the CMB preventing any 21 cm signal. When the ionization fraction drops to  $\sim 10^{-4}$ , Compton scattering is no longer effective (Furlanetto et al., 2006), and the gas begins to cool

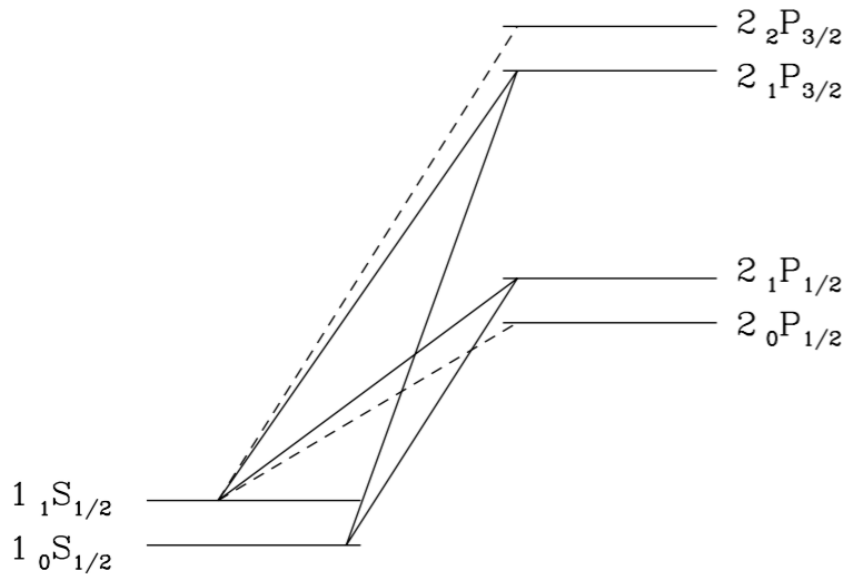


Figure 1.2: The Wouthuysen–Field effect schematic (Furlanetto et al., 2006) shows the fundamental S and the excited P levels. The solid lines represent the transition of the Hydrogen atom from the P states to the ground state while the dashed lines indicate the transition from the P state to the hyperfine triplet state.

adiabatically, i.e. faster than the CMB. At these redshifts the universe is still sufficiently dense that  $T_s = T_k$  via collisional coupling, allowing the 21 cm to appear in absorption against the CMB (“Dark Ages”);

- $z \sim 30$ : Collisional coupling became ineffective leading to  $T_s \sim T_{\text{CMB}}$  and the 21 cm signal to disappear;
- $30 > z > 20$ : The first luminous sources are expected to appear and emit a Ly $\alpha$  radiation background that coupled the spin temperature to the gas temperature through the Wouthuysen–Field effect. As the gas is colder than the CMB, the 21 cm signal is still visible in absorption against the CMB;
- $20 > z > 15$ : As star formation progresses in the first halos, stellar black holes are formed

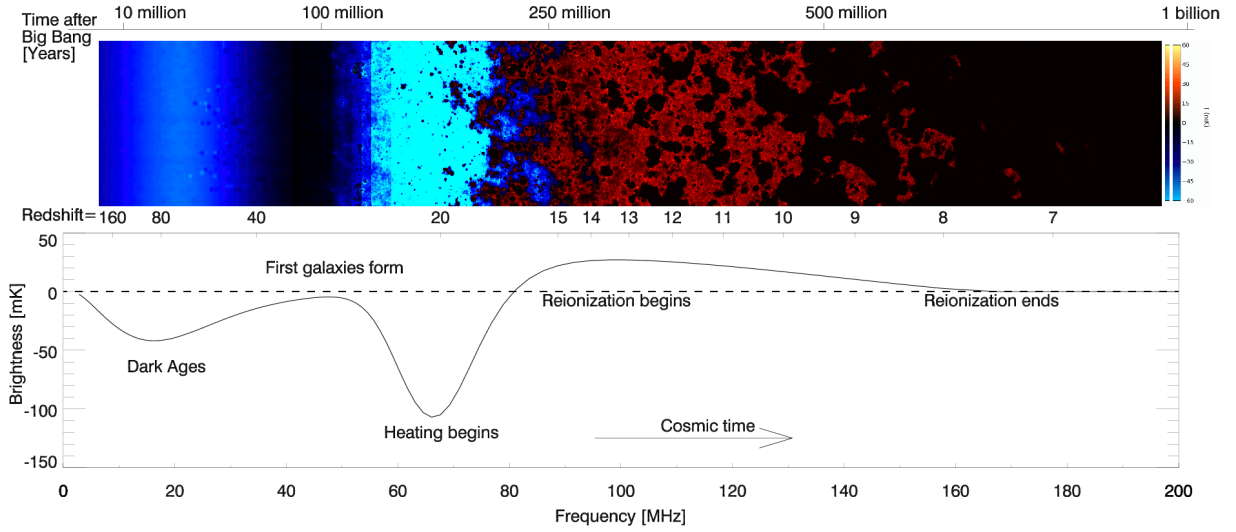


Figure 1.3: *Upper panel:* Time evolution of the 21 cm brightness temperature  $T_b$  (Mellema et al., 2006). *Lower panel:* Fiducial model of the global 21 cm brightness temperature with relevant epochs highlighted (Pritchard & Loeb, 2010).

and X-ray radiation is emitted from binary systems (Pritchard & Furlanetto, 2007). X-ray emission effectively heats the IGM, eventually driving  $T_k > T_{\text{CMB}}$  at  $z \sim 15$  (in this reference model) and the 21 cm signal is in emission with respect to the CMB;

- $15 > z > 6$ : Star formation progresses continuously and widespread reionization starts to take place until the IGM is fully ionized ( $z \sim 6$ ). The reionization process is driven by many factors. To name a few, the ultra-violet radiation from young, star-forming galaxies and quasars, the escape fraction (i.e. the fraction of ionizing radiation) and the radiative transfer (Ciardi & Ferrara, 2005; Zaroubi, 2013).

## 1.4 Fluctuations in the 21 cm signal

In the previous section we described the main milestones in the evolution of the global 21 cm signal. Once spatial fluctuations are considered, however, the 21 cm signal encodes a much greater wealth of information. Simulations of the three-dimensional evolution of 21 cm signal have been the subject of extensive work over the last two decades (Trac & Cen, 2007; Trac &

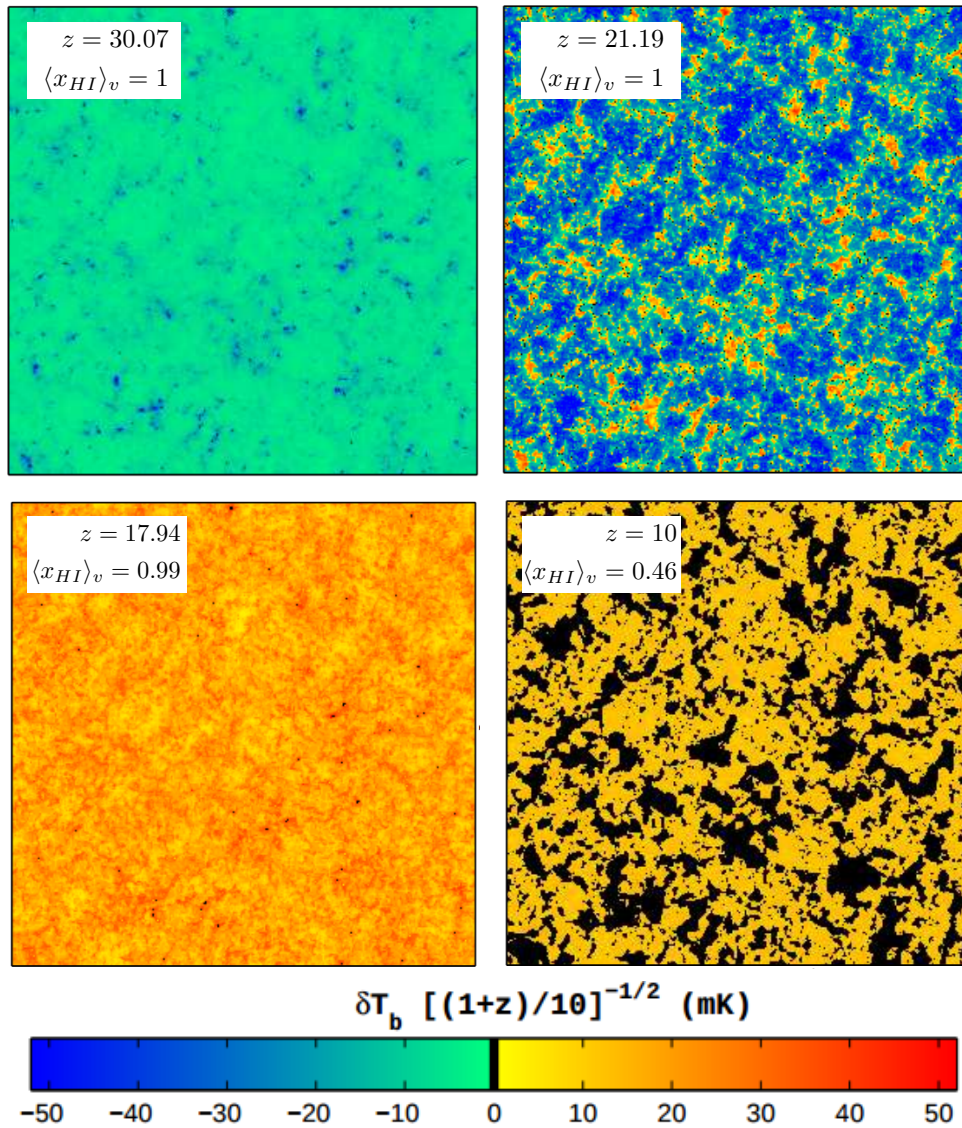


Figure 1.4: Slices from a “semi-numerical” simulation of the 21 cm signal (Mesinger et al., 2011) featuring  $\delta T_b$  at  $z = 30.1, 21.1, 17.9$  and  $10$ . The slices are 1 Gpc wide and 3.3 Mpc deep.

Gnedin, 2011; Mesinger et al., 2011). In this section I will summarize the evolutionary profile of 21 cm fluctuations that has emerged from the body of theoretical simulations. We use Figure 1.4 (Mesinger et al., 2011) to describe the main phases of the evolution of the 21 cm fluctuations similarly to what we did in the previous section:

- $z \sim 30$ : as we described in §1.3, the spin temperature became coupled to the gas temper-

ature through the Wouthuysen-Field effect once the first stars lit up. Fluctuations in the 21 cm signal are here driven by fluctuations in the Ly $\alpha$  emissivity (Furlanetto et al., 2006; McQuinn, 2016);

- $z \sim 21$ : X-ray emissions started heating the IGM, ultimately driving the gas temperature above the CMB temperature. Heating began first in pockets around the X-ray sources, leaving still large, cold IGM regions. 21 cm fluctuations are then driven by fluctuations in the gas temperature. The first, very small ionized regions began to appear around the brightest star forming galaxies (Barkana & Loeb, 2001; Pritchard & Loeb, 2012; McQuinn, 2016);
- $z \sim 18$ : Heating reached its point of saturation, that is,  $T_s \gg T_{\text{CMB}}$ . With the IGM quasi-uniformly heated, 21 cm fluctuations are now driven by large-scale density fluctuations (Barkana & Loeb, 2001);
- $z \sim 10$ : Reionization was then well underway and Mpc-size ionized regions were formed around the brightest sources. Fluctuations in the HI neutral fraction are the main driver of 21 cm fluctuations (Furlanetto et al., 2006; McQuinn, 2016).

Fluctuations in the 21 cm signal are commonly characterized through their power spectrum  $P(k)$  (e.g., Furlanetto et al., 2006; Morales et al., 2006):

$$\langle T_b(\vec{k}) \tilde{T}_b(\vec{k}') \rangle = (2\pi)^3 \delta(k - k') P(k) \quad (1.2)$$

where  $\langle \rangle$  denotes an ensemble average,  $\delta$  is the Dirac delta function and  $\vec{k}$  is the Fourier conjugate of the three dimensional spatial coordinate. Figure 1.5 (Lidz et al., 2008) shows the evolution of the dimensionless 21 cm power spectrum  $\Delta_{21}^2(k) = \frac{k^3}{2\pi^2} P(k)$  as a function of the average ionization fraction  $\langle x_i \rangle$ , that acts as a time coordinate. At the onset of reionization ( $\langle x_i \rangle = 0.02$ ) the 21 cm power spectrum still follows the matter density power spectrum, however, the power drops fairly quickly on large scales,  $k < 1 h \text{ Mpc}^{-1}$ , since the ionized bubbles appear in the densest regions first. By mid reionization, when  $\langle x_i \rangle \sim 0.5$ , the contrast between neutral and ionized gas becomes significant and the power increases again on large scales. On scales

smaller than the ionized bubbles, the 21 cm power spectrum is smaller than the expected matter power spectrum resulting in an overall flattening of  $\Delta_{21}^2(k)$  throughout reionization. The power spectrum amplitude gradually decreases with increasing  $\langle x_i \rangle$ . The variations in power spectrum amplitude and slope of the 21 cm signal, therefore, prove to be promising observables for current radio interferometers throughout reionization. Another powerful observable is the signal variance defined as the integral of the signal's power spectrum (Jelić et al., 2008; Harker et al., 2009; Iliev et al., 2008; Patil et al., 2014).

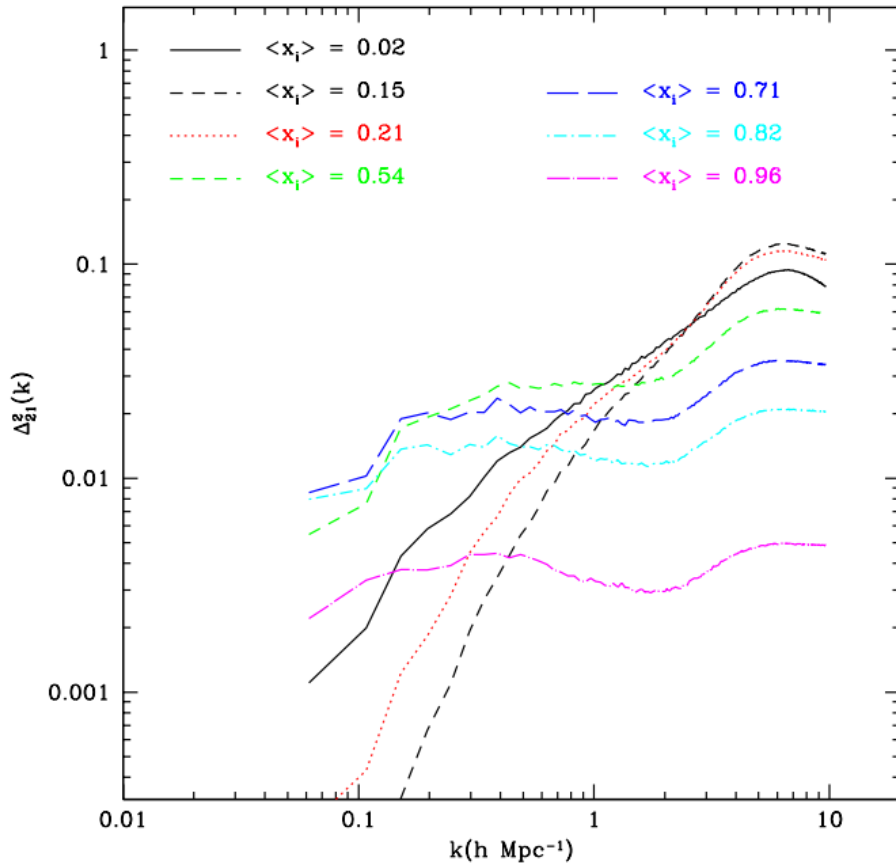


Figure 1.5: Evolution of the 21 cm dimensionless power spectrum  $\Delta_{21}^2(k)$  throughout reionization (Lidz et al., 2008).

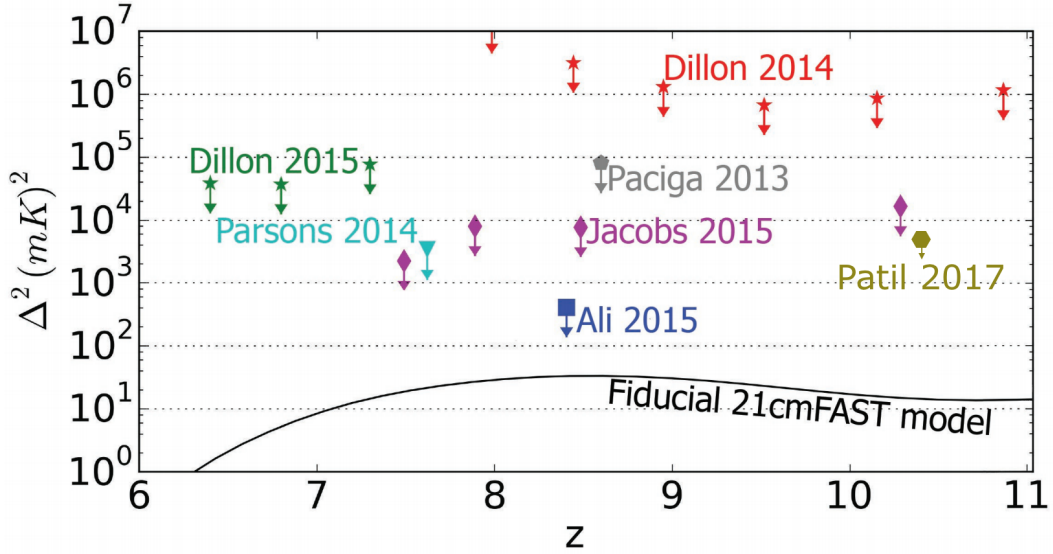


Figure 1.6: Best upper limits to the 21 cm power spectrum to date (DeBoer et al., 2017) from GMRT at  $z = 8.6$  (gray; Paciga et al., 2013), MWA at  $z = 6.8$  (green; Dillon et al., 2015) and  $z = 9.5$  (red; Dillon et al., 2014), PAPER at  $z = 7.5$  (purple; Jacobs et al., 2015),  $z = 7.7$  (cyan; Parsons et al., 2014) and  $z = 8.5$  (blue; Ali et al., 2015) and LOFAR at  $9.6 < z < 10.6$  (gold; Patil et al., 2017). Error bars are at the  $2\sigma$  confidence level.

## 1.5 Current observational status

The 21 cm signal is still eluding detection to date, despite the pursuit from an increasing number of instruments. On one side, arrays of radio telescopes search for 21 cm fluctuations (Dillon et al., 2015; Jacobs et al., 2015; Trott et al., 2016; Ewall-Wice et al., 2016; Beardsley et al., 2016). Such radio arrays include the Precision Array to Probe the Epoch of Reionization (PAPER; Parsons et al., 2010), Low Frequency Radio Array (LOFAR; van Haarlem et al., 2013), the Murchison Widefield Array (MWA; Tingay et al., 2013) and the Hydrogen Epoch of Reionization (HERA; DeBoer et al., 2017). On the other hand single dipole experiments look for the global 21 cm signal across the whole sky (refer to §1.3). Examples of such experiments are the Experiment to Detect the Global EoR Signature (EDGES; Bowman & Rogers, 2010; Monsalve et al., 2017), the Large aperture Experiment to detect the Dark Ages (LEDA; Bernardi et al., 2016; Price et al.,

2017), the Dark Ages Radio Explorer (DARE; Burns et al., 2017), Shaped Antenna measurement of background Radio Spectrum (SARAS; Patra et al., 2013; Singh et al., 2017) and the Broadband Instrument for Global Hydrogen Reionization Signal (BIGHORNS; Sokolowski et al., 2015).

Monsalve et al. (2017) provide significant improvements to the results in Bowman & Rogers (2010) and agrees with the upper limits on the reionization duration  $\Delta z > 3$  measured by George et al. (2015).

Figure 1.6 shows the current best 21 cm power spectrum upper limits. Paciga et al. (2013) presented an upper limit of  $(248 \text{ mK})^2$  at  $k = 0.50 \text{ h Mpc}^{-1}$  using 40 hours of data from GMRT. Dillon et al. (2015) set an upper limit of  $(\sim 173 \text{ mK})^2$  at  $k = 0.18 \text{ h Mpc}^{-1}$  using 3 hours of data from MWA. Patil et al. (2017) presented their first limit of  $(79.6 \text{ mK})^2$  at  $k = 0.053 \text{ h Mpc}^{-1}$  using 13 hours of data from LOFAR; they provide upper limits at the highest redshift and largest comoving scales amongst all 21 cm experiments. Ali et al. (2015) have placed the strongest upper limit of  $(22.4 \text{ mK})^2$  between  $0.15 < k < 0.15 \text{ h Mpc}^{-1}$  on the 21 cm power spectrum to date at  $z = 8.4$  (Ali et al., 2015) using 135 days of data,  $\sim 2$  orders of magnitude higher than the expected 21 cm signal. Their results are consistent with the IGM that is hotter than 10 K at  $z = 8.4$ , thus ruling out the reionization models for which the gas temperature is below 10 K. The comparison between the upper limits is difficult given the different redshift ranges,  $k$ -modes, integration times, antenna configurations and data processing methods.

We discuss challenges associated with 21 cm power spectrum observations in the next chapter.

---

### Challenges of 21 cm experiments and thesis motivation

---

*I*n the last decade, considerable efforts were made towards designing and improving the sensitivity of instruments dedicated to 21 cm observations. Along with improved instrumentation, control over systematic errors is essential and, perhaps, the biggest challenge. This chapter reviews the observational challenges pertaining to 21 cm experiments. Firstly, the astrophysical foregrounds that are a few orders of magnitude brighter than the expected 21 cm signal ([Shaver et al., 1999](#); [Jelić et al., 2008](#); [Bernardi et al., 2009](#); [Jelić et al., 2010](#); [Zaroubi et al., 2012](#)), and secondly, the systematics involved in separating the desired signal from the aforementioned foregrounds. Presently, cosmological signal separation is one of the most active areas of research in 21 cm cosmology ([Pober et al., 2013](#); [Dillon et al., 2014](#); [Parsons et al., 2014](#); [Chapman et al., 2015](#)).

#### **2.1 Foreground Emission**

The signal measured by a radio telescope at any given frequency and direction on the sky is a combination of Galactic and extragalactic emission, and the 21 cm signal against the CMB

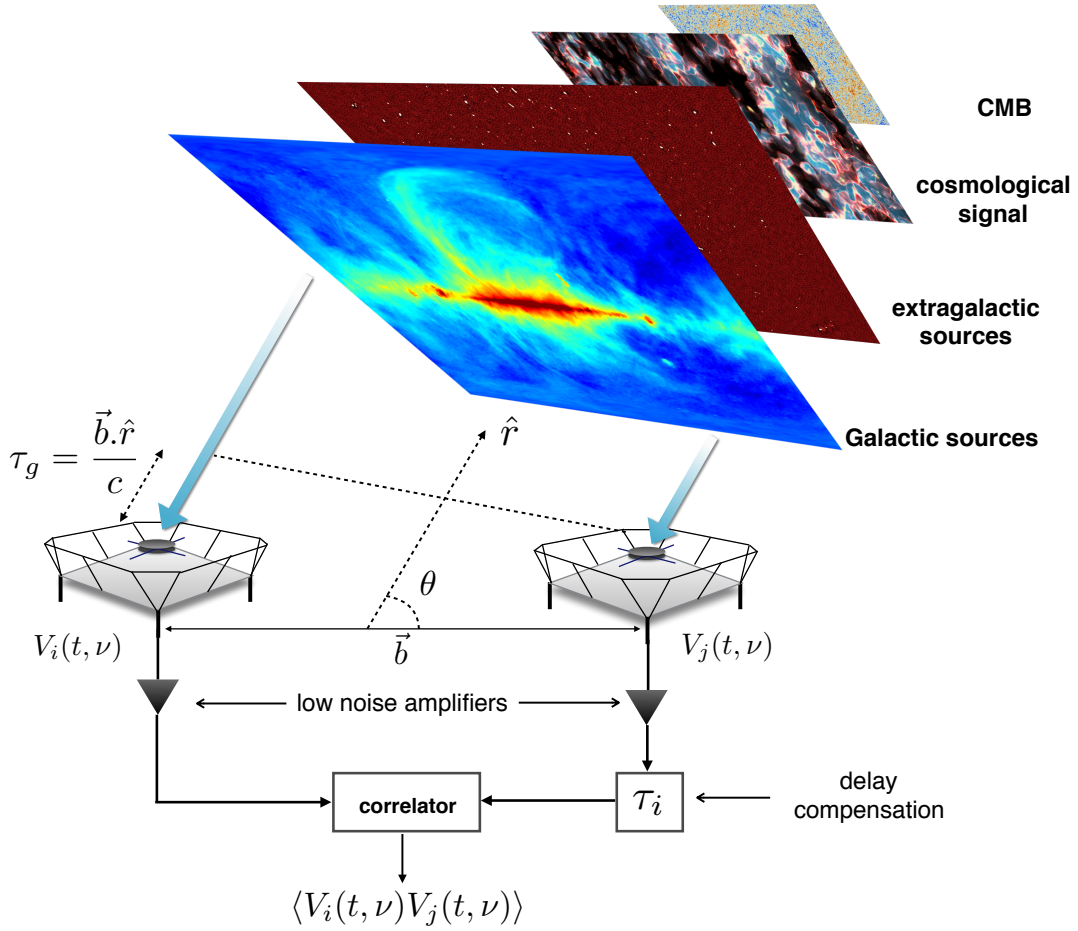


Figure 2.1: A cartoon showing different types of emissions that constitute the signal measured by a 2-element radio interferometer. A radio interferometer is formed by connecting multiple radio telescopes together.

background (Figure 2.1). Galactic emission is mainly due to the synchrotron radiation that arises when relativistic electrons are accelerated by magnetic fields. The radiation emitted by a single electron is beamed along the direction of motion and polarized along the plane perpendicular to the magnetic field. Synchrotron emission with energy  $E = \gamma m_e c^2$ , where  $\gamma$  is the Lorentz factor,  $m_e$  is the mass of the electron and  $c$  is the speed of light, is emitted over a range of frequencies  $\nu$  and it peaks at the critical frequency  $\nu_c$

$$\nu_c \sim \frac{\gamma^2 e H}{2\pi m_e c} \quad (2.1)$$

where  $H$  is the magnetic field strength. At radio frequencies, the synchrotron spectrum resulting from a population of spiraling electrons can be approximated by a power law

$$S_\nu \propto \nu^\alpha \quad (2.2)$$

where  $\alpha$  can be related to the spectral energy distribution of the emitting electrons (Ginzburg & Syrovatskii, 1965).

Galactic synchrotron emission is dominant at frequencies below 2 GHz (Lawson et al., 1987). Haslam et al. (1982) presented an all-sky map at 408 MHz, showing that the Galactic synchrotron emission varies significantly across the sky, ranging from the thick disk around the Galactic plane to features like spurs and cirrus outside the plane. The spectral index varies across the sky and it steepens away from the Galactic plane (Shaver et al., 1999). At 150 MHz, the Galactic synchrotron emission constitutes  $\sim 70\%$  of the sky emission.

Extragalactic sources also emit synchrotron radiation and their integrated emission is estimated to lie between 30 to 50 K at 150 MHz (Bridle, 1967; Cane, 1979; Lawson et al., 1987; Reich & Reich, 1988). The latter constitutes  $\sim 27\%$  of the radio power in the sky (Shaver et al., 1999). The remainder of the power is a combination of free-free emission and the CMB. The extragalactic sky has been studied at low frequencies with different angular resolutions by various surveys, namely, the Westerbork Northern Sky Survey (WENSS; Rengelink et al., 1997), the Very Large Array Low-Frequency Sky Survey (VLSS; Cohen et al., 2007), the Multifrequency Snapshot Sky Survey (MSSS; Heald et al., 2015), the Galactic and Extragalactic All-sky MWA (GLEAM; Hurley-Walker et al., 2017) survey, etc. The deepest all-sky survey of the Southern sky to date is the GLEAM survey with an angular resolution of  $\sim 2'$ . The GLEAM survey is of particular interest for this thesis as the instrument used throughout this work, PAPER (see §4.1) also observes the Southern sky.

Calibration has always been a limiting factor in achieving high dynamic range imaging (Noordam & Smirnov, 2010; Smirnov, 2011b). Understanding the EoR can be considered as an extreme high dynamic imaging problem; there has been growing evidences that calibration could be one of the limiting factors in measuring the 21 cm HI line (Barry et al., 2016; Patil et al., 2016; Ewall-Wice et al., 2017). All-sky surveys are helpful in characterizing extragalactic sources,

however, uncertainties in the flux densities, positions, and spatial morphologies of sources can lead to wrong measurements (Barry et al., 2016; Procopio et al., 2017). On the other hand unmodeled sources can introduce artefacts such as ghost sources and frequency structures into the gain solutions (Grobler et al., 2014; Ewall-Wice et al., 2017).

The GLEAM survey records the spectral index distribution for sources with flux densities greater than 160 mJy (Table 2.1), which are useful in characterizing foregrounds between 100–200 MHz. We may expect deviations from the spectral smoothness of extragalactic radio sources – a fundamental property used in separating foregrounds from the 21 cm signal, because of spectral curvature due to synchrotron self-absorption at low frequencies (Zheng et al., 2012). According to the median spectral index of NVSS<sup>1</sup>-Texas<sup>2</sup> reported by DeBreuck et al. (2000);  $-0.879 \pm 0.04$  for  $S > 1$  Jy and  $-0.879 \pm 0.07$  for  $S > 0.15$  Jy between 365–1400 MHz, the results in Table 2.1 do not support any deviation from spectral smoothness of radio sources. In addition, recent studies of the peaked spectrum sources, constituting to approximately 4.5% of the extragalactic population from the GLEAM survey showed no spectral curvature in the EoR band (Callingham et al., 2017).

Flux density $S$ (Jy)	Spectral index $\alpha$
$S < 0.16$	$-0.78 \pm 0.20$
$0.16 \leq S < 0.5$	$-0.79 \pm 0.15$
$0.5 \leq S < 1.0$	$-0.83 \pm 0.11$
$S \geq 1.0$	$-0.83 \pm 0.11$

Table 2.1: Average spectral index as a function of source flux density (Hurley-Walker et al., 2017).

<sup>1</sup>The NVSS survey was carried out using the Very Large Array interferometer at 1.4 GHz (Condon et al., 1998).

<sup>2</sup>The Texas survey was carried out using the Texas interferometer at 365 MHz (Douglas et al., 1996).

## 2.2 Foreground Separation

All the methods to separate the 21 cm signal from foregrounds rely on the different spectral behavior between foregrounds and the cosmological signal. The foreground synchrotron spectrum is expected to vary smoothly over scales of tens of MHz, contrary to the 21 cm signal, which is coherent only on kHz scales (i.e., [Matteo et al., 2002](#); [Santos et al., 2005](#)). Foreground separation techniques take two different flavors: foreground subtraction and foreground avoidance.

### 2.2.1 Foreground Subtraction

Foreground subtraction (removal) is a well-established method whereby one attempts to model the foregrounds that are subsequently removed from the data. In particular, bright sources are modeled and subtracted from the visibility data, the domain where interferometric measurements are made, and this approach has proven to be very effective ([Smirnov, 2011b](#)). For widefield observations, the varying beam shape and ionospheric effects contribute to variation in errors in the data. Therefore, various schemes have been proposed to subtract sources along with their calibration solutions or corrections ([Mitchell et al., 2008](#); [Bernardi et al., 2010](#); [Yatawatta et al., 2013](#); [Bernardi et al., 2013](#)). However, the brightest sources tend to be resolved below 2 arcmins and therefore improper modeling can lead to errors in the subtraction that are significant in contaminating the residuals and potentially limit the diffuse foreground mitigation ([Procopio et al., 2017](#)).

Even after removing the bright sources, the foreground diffuse emission is well above the EoR signal ([Morales et al., 2006](#); [Bernardi et al., 2010, 2013](#)). Although strong foreground diffuse emission can be deconvolved and subtracted from visibilities or images, it is more effective to model the diffuse emission through spectral fitting and subtract it from an image cube along each line of sight or each image pixel. Spectral fitting methods are classified as parametric and non-parametric. Parametric methods assume an priori foreground spectrum model and fit the spectrum coefficients to the data ([Wang et al., 2006](#); [Bowman et al., 2009](#); [Liu et al., 2009](#); [Petrovic & Oh, 2011](#); [Price et al., 2017](#)). The most commonly adopted parametric method is polynomial fitting in frequency or log frequency ([McQuinn et al., 2006](#); [Bowman et al., 2009](#)).

Parametric techniques are simple to implement, but may induce errors if the assumptions of the known model are incorrect. On the contrary, non-parametric ones use the properties of foregrounds to define the foreground model and they include minimization of spectral inflection points (Harker et al., 2009), spectral single value decomposition (Paciga et al., 2011, 2013) and the Generalized Morphological Component Analysis (Chapman et al., 2014). Such techniques are preferred as they do not require any priori model, but limited calibration accuracy can impart deviations from the spectral smoothness of the observed spectrum (Morales & Hewitt, 2004).

As foreground removal may be accompanied by subtraction errors, Morales et al. (2006) suggests residual error mitigation by fitting them in the power spectrum space.

### 2.2.2 Foreground Avoidance

The avoidance method leverages on the fact that foregrounds and the EoR signal have different footprints in power spectrum space and there is a region (the EoR window), potentially, where the EoR signal dominates over foregrounds. Figure 2.2 shows a cartoon representation of foreground avoidance – a 2D cylindrical power spectrum in  $k$  space, an effective representation of foreground contaminations (Morales & Hewitt, 2004; Vedantham et al., 2012; Liu et al., 2014a,b). The usual representation of  $k$ -space divides  $k$  modes between modes along the line of sight and modes parallel to the plane of the sky. The  $k$  modes along the line of sight are denoted by  $k_{\parallel}$  and those perpendicular to the line of sight are denoted by  $k_{\perp}$  and defined as

$$\begin{aligned} k_{\perp} &= \frac{2\pi \left(\frac{|b|}{\lambda}\right)}{D} \\ k_{\parallel} &= \eta \frac{2\pi f_{21} H_0 E(z)}{c(1+z)^2} \end{aligned} \quad (2.3)$$

where  $\lambda$  is the observing wavelength,  $\eta$  is the Fourier conjugate of frequency  $\nu$ ,  $k_B$  is the Boltzmann constant,  $D$  is the transverse comoving distance,  $B$ ,  $f_{21}$  is the 21 cm line rest frequency,  $z$  is the redshift,  $H_0$  is the Hubble constant and  $E(z) = \sqrt{\Omega_M(1+z)^3 + \Omega_k(1+z)^2 + \Omega_\Lambda}$ , where  $\Omega_M$ ,  $\Omega_k$  and  $\Omega_\Lambda$  are the matter density, curvature and radiation parameters respectively. The boundaries of the  $(k_{\perp}, k_{\parallel})$  space are (Vedantham et al., 2012; Chapman et al., 2014):

$$k_{\perp \min} = \frac{2\pi b_{\min} f_{21}}{c(1+z)D_M} \quad (2.4)$$

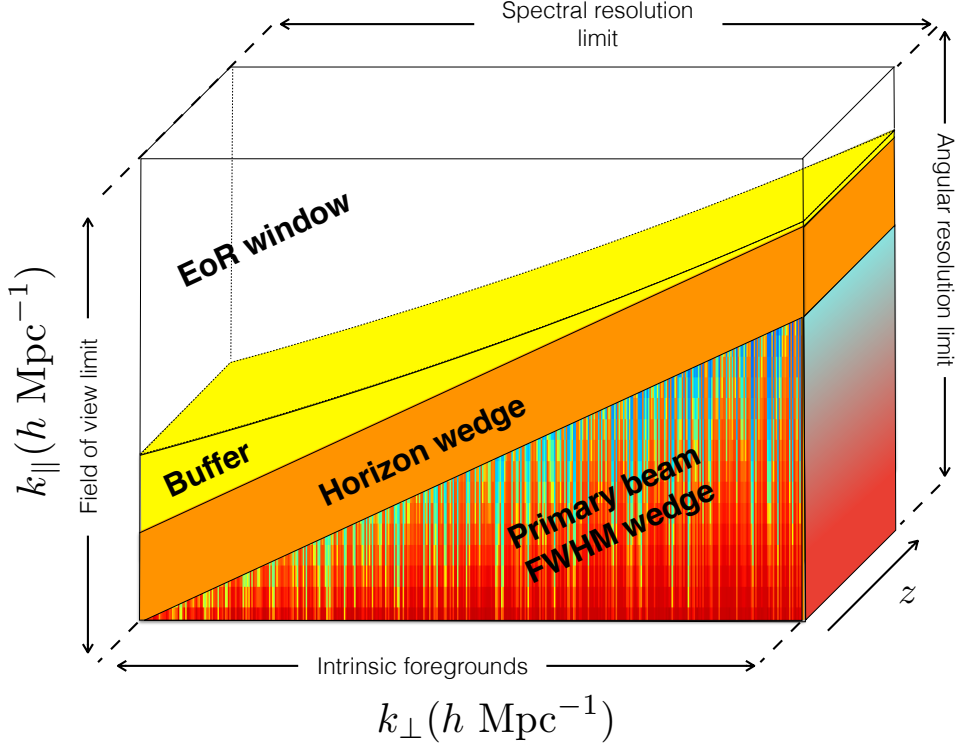


Figure 2.2: The foreground avoidance paradigm. Foregrounds are confined to the lower region of the power spectrum. The orange line marks the horizon limit and the yellow line marks the supra-horizon limit.

$$k_{\perp \max} = \frac{2\pi b_{\max} f_{21}}{c(1+z)D_M} \quad (2.5)$$

$$k_{\parallel \min} = \frac{2\pi H_0 f_{21} E(z)}{c(1+z)^2 \Delta\nu} \quad (2.6)$$

$$k_{\parallel \max} = \frac{2\pi H_0 f_{21} E(z)}{c(1+z)^2 B} \quad (2.7)$$

where  $\Delta\nu$  is the frequency resolution,  $b_{\min}$  and  $b_{\max}$  are the minimum and maximum baseline lengths respectively.

The intrinsic chromaticity of the instrumental response determines the “wedge” shape that we see in Figure 2.2: spectrally smooth foregrounds are confined to the lower part of the 2D power spectrum, and the power spreads at longer baselines or high  $k_{\perp}$  modes. Power from diffuse Galactic emission is concentrated at low  $k_{\perp}$  and  $k_{\parallel}$  values while emission from point sources lies

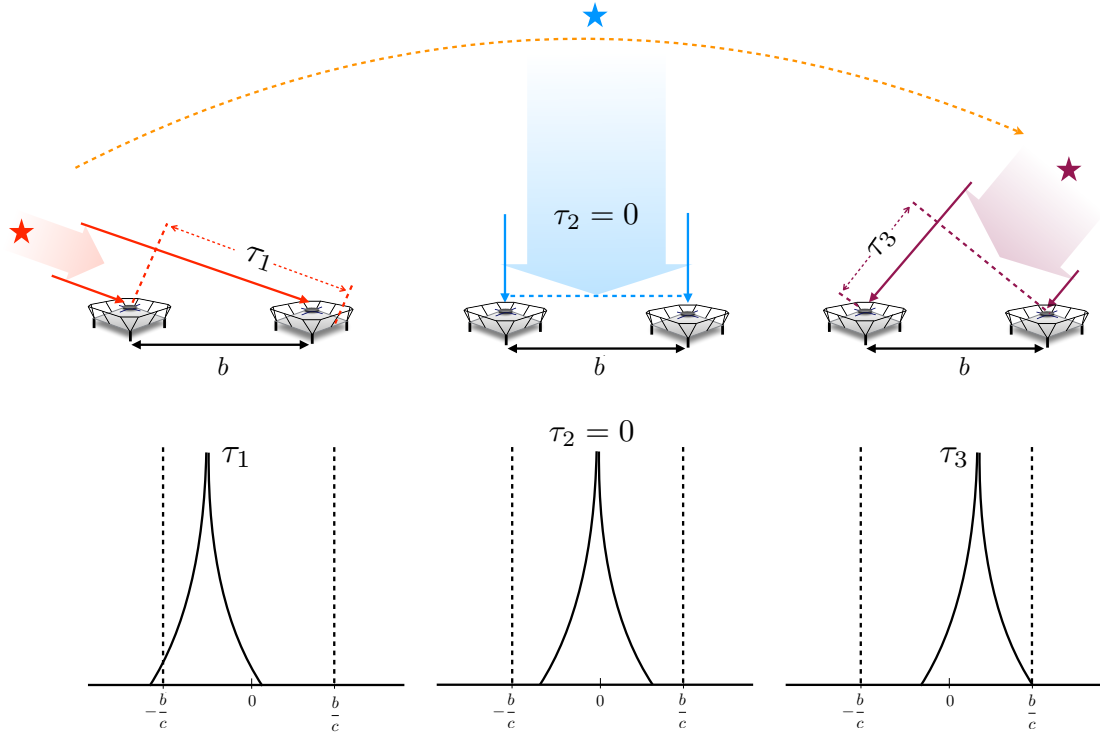


Figure 2.3: Cartoon illustrating changes in the delay transform of a point source as the sky drifts overhead. The delay transform of the visibility corresponding to the source peaks at the corresponding delay, bound by the horizon limit  $\frac{b}{c}$ , where  $b$  is the baseline length.

at all  $k_{\perp}$ , but are downweighted by the wide primary beam. The orange line marks the horizon limit in  $k_{\parallel}$  for a baseline of corresponding length  $k_{\perp}$  (e.g., [Thyagarajan et al., 2013](#)):

$$k_{\parallel} = \frac{H_0 E(z) D}{c(1+z)} k_{\perp}. \quad (2.8)$$

The foreground emission extends beyond the horizon limit because of the intrinsic spectral behavior of the foregrounds, thus, describing a “supra-horizon” limit (yellow line). The supra-horizon limit does not necessarily have a constant width along  $k_{\perp}$  ([Pober et al., 2013](#)), more emission extends beyond the horizon at low  $k_{\perp}$  modes (i.e. shorter baselines) as short baselines do not tend to resolve diffuse Galactic emission. [Parsons et al. \(2012\)](#) proposed a specific foreground avoidance technique where each baseline is treated separately and Fourier transformed along the frequency axis (“delay transform”) to generate a single measurement of the power

spectrum. This approach utilizes the frequency dependence on the baseline sampling to relate frequency to the geometric delay (or lag)  $\tau_g = \frac{\mathbf{b} \cdot \hat{\mathbf{r}}}{c}$ , where  $\mathbf{b}$  is baseline vector and  $\hat{\mathbf{r}}$  is the direction cosines on the celestial sphere (Thompson et al., 2008). As an example, the delay transform of a point source is a  $\delta$ -function convolved with the antenna response and the sampling function in the delay domain. Sidelobes due to the incomplete delay sampling (for instance due to flagged channels contaminated by radio frequency interference) that can spread smooth spectrum emission in the EoR window can be deconvolved (Parsons & Backer, 2009) and the EoR window, in principle, preserved.

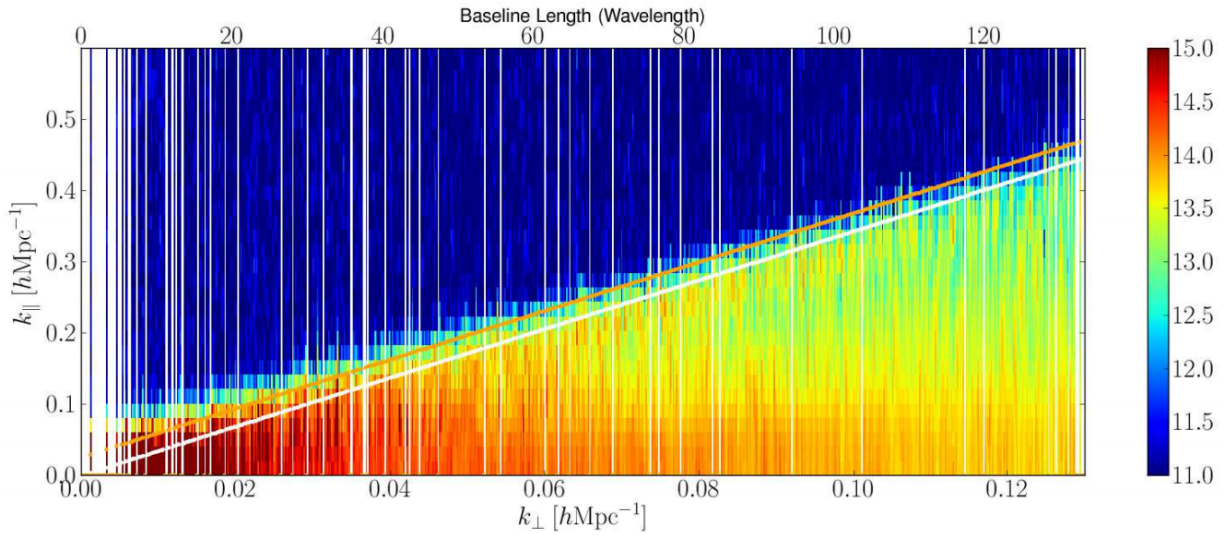


Figure 2.4: 2D power spectrum from PAPER data (Pober et al., 2013). The EoR window is clearly visible as a  $\sim 4$  order of magnitude drop in power with respect to inside-the-wedge emission. We can see that there is evidence of emission that extends  $\sim 50$  ns (orange line) beyond the horizon limit (white line). The colorbar is in logarithmic scale with units  $(\text{mK})^2 h \text{ Mpc}^{-3}$ .

This “wedge” behaviour has been observed in real data (Pober et al., 2013; Thyagarajan et al., 2015, Figures 2.4 and 2.5 respectively). In particular, Thyagarajan et al. (2015) underlined a ‘pitchfork’ signature near the horizon, where the array is sensitive to large-scale structures on all baselines. This behavior is due to the interaction between the foreground emission, particularly, Galactic diffuse emission and the properties of widefield instruments, and is depicted by the enhanced power at the horizon (Thyagarajan et al., 2015).

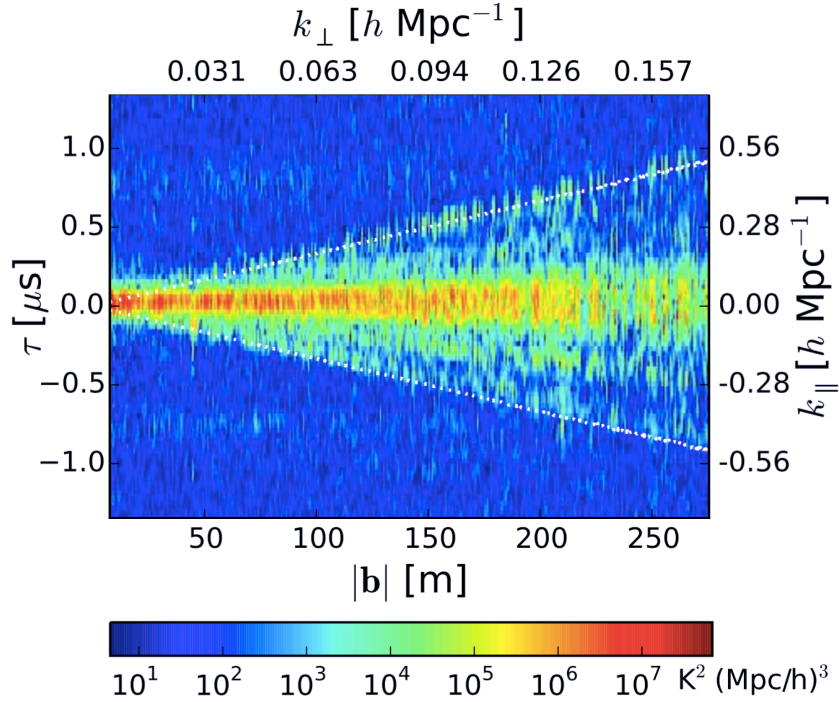


Figure 2.5: Similar to Figure 2.4, but using MWA data and retaining the negative delay values that show a “pitchfork” shape (Thyagarajan et al., 2015). The white lines mark the horizon limit.

Deviations from spectral smoothness are likely to invalidate the assumptions behind foreground separation methods. Amongst them, the leakage from polarized foregrounds into the EoR window as they are Faraday rotated in the interstellar medium, can jeopardize EoR measurements (Bernardi et al., 2010; Jelić et al., 2010; Geil et al., 2011; Asad et al., 2015, 2016).

## 2.3 Polarization Leakage

Polarized emissions are usually described in terms of Stokes parameters (Kraus, 1966) where  $I$  is the total intensity of the incoming radiation,  $Q$  and  $U$  describe the linear polarizations, and  $V$  denotes the circular polarization.

### 2.3.1 Polarized Foregrounds

Faraday rotation is the effect of rotation of the polarization angle  $\chi$  when a linearly polarized electromagnetic wave passes through ionized plasma. This rotation can be described as

$$\chi = \chi_0 + \phi\lambda^2 \quad (2.9)$$

where  $\chi_0$  is the intrinsic polarization angle and  $\phi$  is the Faraday depth in  $\text{rad m}^{-2}$  (Brentjens & de Bruyn, 2005)

$$\phi = 0.81 \int_{\text{source}}^{\text{observer}} n_e B_{\parallel} dl \quad (2.10)$$

where  $n_e$  the electron density,  $B_{\parallel}$  the magnetic field along the line of sight to the source and  $dl$  is the infinitesimal path length.

Significant efforts have been made in the past years to characterize polarized emission from both our Galaxy and extragalactic objects. Observations of polarized emission suggest that most of the emission is contained in diffuse structures (Bernardi et al., 2009, 2010; Jelić et al., 2015). Examples of polarized Galactic observations at 150 MHz include the Fan region observed by the Westerbork Synthesis Radio Telescope (WSRT; Bernardi et al., 2009), the 3C 196 field observed by both WSRT (Bernardi et al., 2010) and LOFAR (Jelić et al., 2015) on different angular scales and, linearly polarized point sources observed by MWA (Lenc et al., 2017). The Fan region refers to a patch of sky centered at Galactic longitude  $130^\circ$  and latitude  $5^\circ$  (Wielebinski & Shakeshaft, 1962), where fluctuations of 14 K rms had been discovered on scales greater than 13 arcmins in the Galactic diffuse emission for the first time (Bernardi et al., 2009).

The 3C 196 field is centered around the bright quasar 3C 196 at Galactic longitude  $171^\circ$  and latitude  $33^\circ$  in one of the coldest regions of the Galactic halo. Polarized emissions measured around 3C 196 field by WSRT and LOFAR are shown in Figure 2.6. WSRT measurements reveal only faint patchy emission while LOFAR measurements unfold a straight filament running from North to South through the center of the field and this morphology is believed to be due to depolarization that happens via vector addition (Jelić et al., 2015). The difference in morphologies is thought to result from two separate effects. Firstly, the Faraday depth resolution of LOFAR observations is three times better than WSRT observations (Jelić et al., 2015). Secondly,

the instrumental artefacts measured by WSRT (left panel of Figure 2.6; Bernardi et al., 2010) that contaminate the  $\phi$  cubes (Jelić et al., 2015).

Jelić et al. (2015) used the measurements of a  $3^\circ \times 3^\circ$  inner patch of the 3C 196 field to estimate the angular power spectrum of the integrated emission (evaluated by integrating the polarized intensity at each pixel along different Faraday depths). A power law was fitted to the angular power spectrum between  $150 < l < 2700$ , where  $l = \frac{180}{\theta}$  and  $\theta$  is the angular scale in degrees. This yielded a slope similar to that of Bernardi et al. (2009) on the same angular scales and frequency range, despite different emission morphologies of the two fields. This implies that power is distributed in a similar fashion along Faraday depths in both fields. Moreover, Jelić et al. (2015) calculated the observed polarization level to be  $\sim 4\%$  using the all-sky map at 408 MHz (Haslam et al., 1982) scaled to 160 MHz and a spectral index of  $-2.5$ .

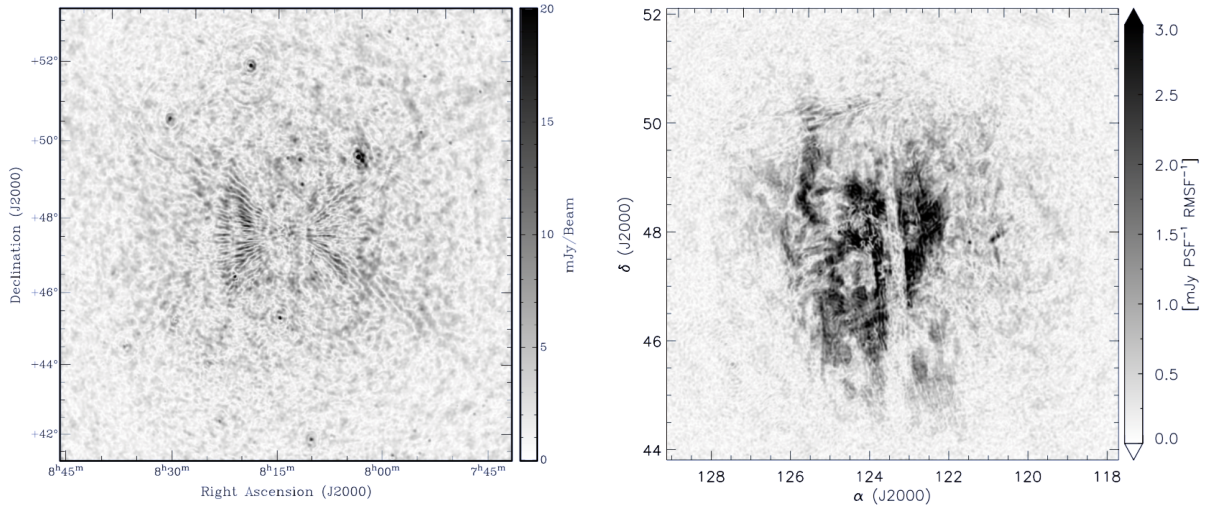


Figure 2.6: Polarized intensity of the 3C 196 field measured by Bernardi et al. (2010) (left) and Jelić et al. (2015) (right) at  $\phi = 4$  and  $1.5 \text{ rad m}^{-2}$  respectively.

The largest polarization survey to date below 200 MHz by Bernardi et al. (2013) studied a  $20^\circ$  strip at Galactic latitude  $b < -20^\circ$ , covering 2400 square degrees using MWA. They found diffuse polarized emission over many degrees across the sky in the  $0 < \phi < 10 \text{ rad m}^{-2}$  Faraday range that reveal a wealth of patchy and filamentary structures. Furthermore, the diffuse polarized emission decreases significantly at right ascensions greater than  $2^{\text{h}}30^{\text{m}}$ , and the rms fluctuations

reduce by a factor of 4 as we move away from the South Galactic pole (Bernardi et al., 2013).

One of the most comprehensive polarized point source catalogues is the NRAO VLA Sky Survey (NVSS; Condon et al., 1998), covering 82% of the sky above declination  $-40^\circ$  at 1.4 GHz. The catalogue lists discrete sources down to a flux density of 2 mJy. Recently, Lenc et al. (2017) discovered six linearly polarized sources in a 6000 square degree field observed by MWA, out of which four are pulsars and the brightest one measured by MWA to date being PKS J0636-2036 (peak flux density of 1283 Jy). The spectra along Faraday depth of these sources peak at different rotation measures (RM) that are consistent with the RM values found in the literature (Johnston et al., 2005; Taylor et al., 2009; Bernardi et al., 2013; Dai et al., 2015) within  $\pm 2$  rad  $\text{m}^{-2}$ . The discovery of these polarized point sources aids in constraining the mean polarized flux at respective frequencies.

Jelić et al. (2010) predicted polarization leakage into the EoR signal. They considered a model of Galactic polarization tailored to match the observations of the Fan region (Bernardi et al., 2009). Assuming a 1% calibration error, fluctuations along the line of sight due to polarization leakage clearly occur on frequency and amplitude scales that can mimic an EoR signal (Figure 2.7).

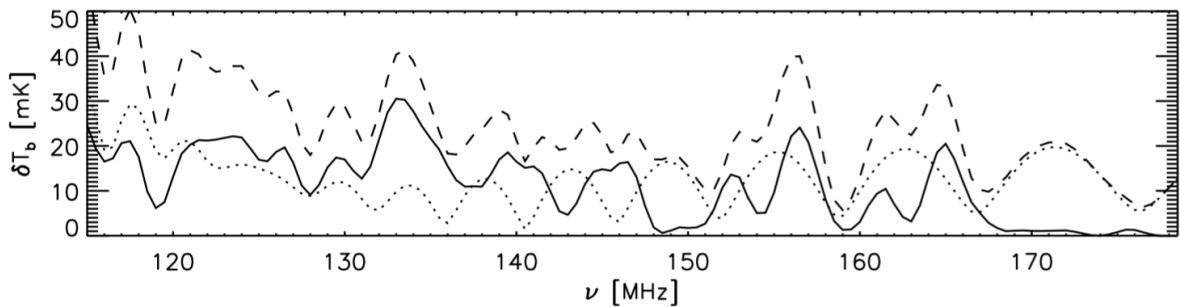


Figure 2.7: Spectral behaviour along a random line of sight through a simulated 21 cm cube (solid line). The dotted line shows the leakage from Galactic polarized emission to total intensity. The dashed line represents the sum of the 21 cm signal and the leakage; (Figure 7 of Jelić et al. (2010)).

Asad et al. (2015, 2016) extended this work by including more realistic simulations of LO-

FAR observations on 3C 295, 3C 196 and the North Celestial Pole, where compact polarized sources are less contaminated by diffuse polarized emission. They found that neither polarized point sources nor polarized diffuse Galactic emission seem to contaminate the EoR window. However, the impact of polarized foreground on the EoR window might be potentially severe for larger field of view instruments like PAPER as they are unable to isolate sky regions with intrinsically low Galactic polarization. [Moore et al. \(2013\)](#) constructed power spectra from a three-month observing campaign of the 32-element configuration of PAPER, and estimated the polarization leakage to be  $\sim 10^3$  and  $10^2$  mK<sup>2</sup> at 126 ( $z = 10.3$ ) and 164 ( $z = 7.66$ ) MHz respectively.

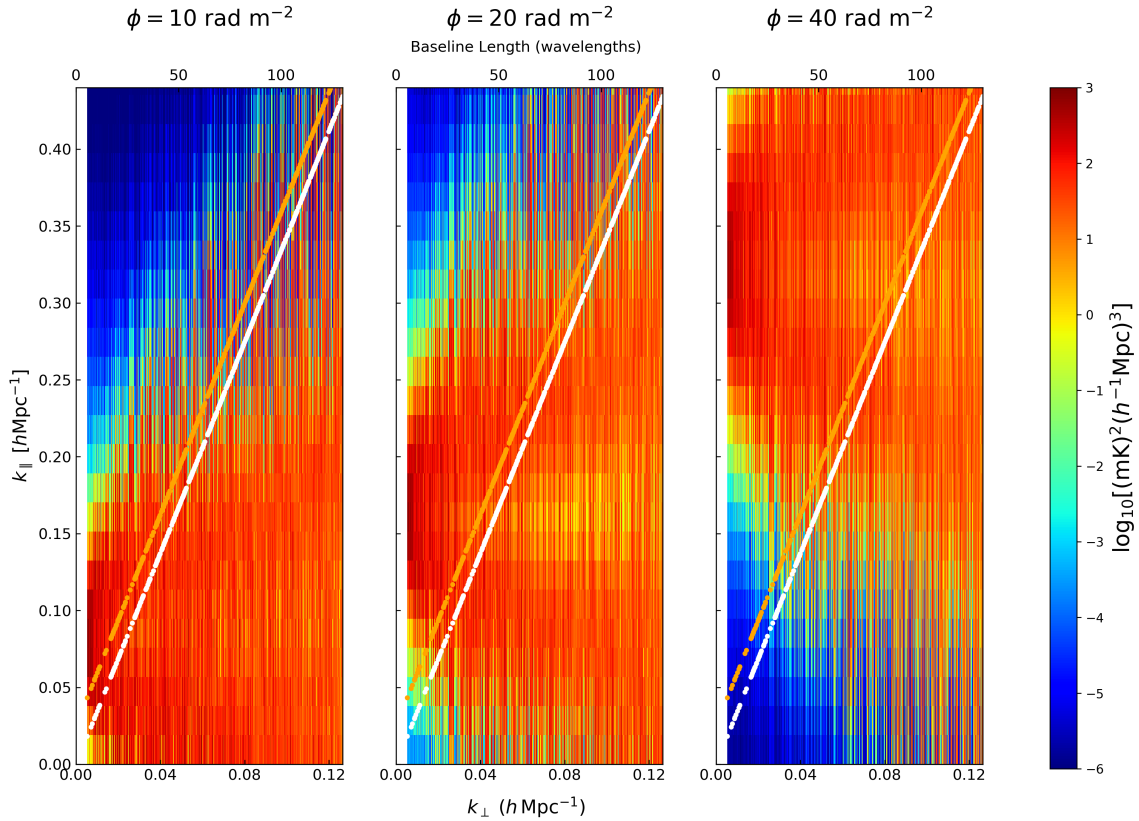


Figure 2.8: 2D Stokes Q power spectra generated from a 10 Jy polarized point source at  $\phi = 10$ , 20 and 40 rad m<sup>-2</sup>.

Polarization leakage may be even more dangerous for foreground avoidance as the latter does

not permit foreground modeling and subtraction of sources and thus,  $\phi$  directly maps into  $k_{\parallel}$ :

$$k_{\parallel} = \frac{4 \lambda^2 H(z)}{c(1+z)} \phi. \quad (2.11)$$

Sources at high  $\phi$  will therefore have power peaking directly into the EoR window. To demonstrate the relationship between  $\phi$  and  $k_{\parallel}$ , in short, equation 2.11, we constructed 2D Stokes  $Q$  power spectra at  $z = 8.5$  for different  $\phi$  values from a 10 Jy polarized point source simulation (Figure 2.8). We see that at high  $\phi$  values, Stokes  $Q$  power spreads outside the horizon limit, as a result any leakage from Stokes  $Q$  will most likely contaminate the EoR window.

It is, therefore, crucial to understand the impact of polarization leakage to the EoR signal for wide field of view observations where foreground avoidance is used and this is the goal and motivation of this thesis. In chapter 3, we developed a formalism that allows the simulation of the impact of polarization leakage in the EoR power spectrum in wide field of view observations and carried out simulations for PAPER-like observations. We developed models for both diffuse and point like polarized emission at low frequencies. In chapter 4, we analyzed the final PAPER observations in order to provide constraints to the polarization models and, therefore, provide improved estimates to the expected polarization leakage to the EoR power spectrum.

## CHAPTER 3

---

### Constraining polarized foregrounds for EoR experiments: polarization leakage simulations in the avoidance scheme<sup>1</sup>

---

The leakage from polarized foregrounds into the EoR window may contaminate the 21 cm measurements as discussed in chapter 2. In this chapter, we develop a formalism to describe the leakage due to instrumental widefield effects in the visibility–based power spectra measured with redundant arrays. The delay–spectrum approach presented in [Parsons et al. \(2012\)](#) is extended to include polarized emission. We then construct polarized sky models and propagate them through the instrument model in order to simulate realistic full–sky observations with PAPER ([Parsons et al., 2010](#)).

---

<sup>1</sup>originally published as: *C.D. Nunhokee, G. Bernardi, S.A. Kohn, J.E. Aguirre, N. Thyagarajan, J.S. Dillon, G. Foster, T.L. Grobler, J.Z.E. Martinot, A.R. Parsons, 2017, ApJ, 848, 11*

### 3.1 Formalism

The relationship between the sky brightness distribution  $s$  and the visibility  $v$  measured by a two–element interferometer is described by (e.g. [Thompson et al., 2008](#)):

$$v(\mathbf{b}, \nu) = \int_{\Omega} a(\hat{\mathbf{r}}, \nu) s(\hat{\mathbf{r}}, \nu) e^{-2\pi i \nu \frac{\mathbf{b} \cdot \hat{\mathbf{r}}}{c}} d\Omega, \quad (3.1)$$

where  $s$  is the Stokes I parameter,  $\mathbf{b} = (u, v, w)^2$  is the vector representing the coordinates in meters in the plane of the array,  $\hat{\mathbf{r}} = (l, m, n)$  is the unit vector representing the direction cosines on the celestial sphere (see [Thompson et al., 2008](#), for further details),  $\nu$  is the observing frequency,  $a$  describes the telescope primary beam response,  $c$  is the speed of the light and  $\Omega$  is the solid angle subtended by the source. Throughout the chapter we will assume array coplanarity and simulate zenith observations, leading to  $\mathbf{b} = (u, v)$ ,  $\hat{\mathbf{r}} = (l, m)$ ,  $wn = 0$ , and reducing equation 3.1 to a two dimensional Fourier transform relationship.

Equation 3.1 does not specify a polarization frame but it can be generalized to include the polarization state of the sky brightness using the measurement equation formalism ([Hamaker et al., 1996](#); [Smirnov, 2011a](#)), where the input radiation field is related to the sampled voltages via  $2 \times 2$  Jones matrices (also known as Mueller matrices). If the intrinsic sky brightness distribution towards a line of sight  $\hat{\mathbf{r}}$  at the frequency  $\nu$  is described by the usual Stokes parameters  $\mathbf{s} = (I, Q, U, V)^T$ , with  $T$  the transpose operator, the sky brightness distribution observed through the telescope primary beam  $\mathbf{s}' = (I', Q', U', V')^T$  becomes (e.g. [Ord et al., 2010](#)):

$$\begin{aligned} \mathbf{s}'(\hat{\mathbf{r}}, \nu) &= \mathbf{A}(\hat{\mathbf{r}}, \nu) \mathbf{s}(\hat{\mathbf{r}}, \nu) \\ &= \mathbf{S}^{-1} [\mathbf{J}(\hat{\mathbf{r}}, \nu) \otimes \mathbf{J}^*(\hat{\mathbf{r}}, \nu)] \mathbf{S} \mathbf{s}(\hat{\mathbf{r}}, \nu) \end{aligned} \quad (3.2)$$

where  $\mathbf{J}$  is the  $2 \times 2$  Jones matrix representing the polarized primary beam response,  $\otimes$  is the outer (Kronecker) product operator,  $*$  denotes the complex conjugate and  $\mathbf{S}$  is the matrix that

---

<sup>2</sup>Throughout this chapter, capital boldface letters are used to indicate matrices, small boldface letters to indicate vectors and small normal letters to indicate scalars.

relates the Stokes parameters to the orthogonal  $x - y$  linear feed frame:

$$\mathbf{S} = \frac{1}{2} \begin{pmatrix} 1 & 1 & 0 & 0 \\ 0 & 0 & 1 & i \\ 0 & 0 & 1 & -i \\ 1 & -1 & 0 & 0 \end{pmatrix}.$$

The  $4 \times 4$  matrix  $\mathbf{A}$  can be seen as a mixing matrix between intrinsic and observed (primed) Stokes parameters:

$$\begin{pmatrix} I' \leftarrow I & I' \leftarrow Q & I' \leftarrow U & I' \leftarrow V \\ Q' \leftarrow I & Q' \leftarrow Q & Q' \leftarrow U & Q' \leftarrow V \\ U' \leftarrow I & U' \leftarrow Q & U' \leftarrow U & U' \leftarrow V \\ V' \leftarrow I & V' \leftarrow Q & V' \leftarrow U & V' \leftarrow V \end{pmatrix}.$$

Equation 3.1 can be extended to the polarized case by defining the four ‘‘Stokes’’ visibility products  $\mathbf{v} = (v_I, v_Q, v_U, v_V)^T$ :

$$\begin{aligned} \mathbf{v}(\mathbf{b}, \nu) &= \mathbf{S}^{-1} \mathbf{v}_c(\mathbf{b}, \nu) \\ &= \mathbf{S}^{-1} \int_{\Omega} [\mathbf{J}(\hat{\mathbf{r}}, \nu) \otimes \mathbf{J}^*(\hat{\mathbf{r}}, \nu)] \mathbf{S} \mathbf{s}(\hat{\mathbf{r}}, \nu) e^{-2\pi i \nu \frac{\mathbf{b} \cdot \hat{\mathbf{r}}}{c}} d\Omega \\ &= \int_{\Omega} \mathbf{A}(\hat{\mathbf{r}}, \nu) \mathbf{s}(\hat{\mathbf{r}}, \nu) e^{-2\pi i \nu \frac{\mathbf{b} \cdot \hat{\mathbf{r}}}{c}} d\Omega \end{aligned} \quad (3.3)$$

where  $\mathbf{v} = (v_{xx}, v_{xy}, v_{yx}, v_{yy})^T$  contains the four cross-polarization correlator outputs. Equation 3.3 recasts the full sky formalism developed by Smirnov (2011a) in the Mueller matrix form.

We are now in the position to define four polarization power spectra by applying the delay transform to equation 3.3. The delay-transform is the Fourier transform of a single visibility along frequency (Parsons & Backer, 2009; Parsons et al., 2012):

$$\tilde{\mathbf{v}}(\mathbf{b}, \tau) = \int_B w(\nu) \mathbf{v}(\mathbf{b}, \nu) e^{-2\pi i \nu \tau} d\nu, \quad (3.4)$$

where  $B$  is the observing bandwidth,  $w$  is the window function and  $\tau$  represents the geometric delay between antenna pairs:

$$\tau = \frac{\mathbf{b} \cdot \hat{\mathbf{r}}}{c}. \quad (3.5)$$

The delay transform is related to the 21 cm power spectrum  $p(k)$  as (Parsons et al., 2012; Thyagarajan et al., 2016):

$$\begin{aligned} p(k) &= p\left(\sqrt{k_{\perp}^2 + k_{\parallel}^2}\right) \\ &= \left(\frac{\lambda^2}{2k_B}\right)^2 \left(\frac{D^2 \Delta D}{B}\right) \frac{1}{q} |\tilde{\mathbf{v}}(|\mathbf{b}|, \tau)|^2, \end{aligned} \quad (3.6)$$

with

$$k_{\perp} = \frac{2\pi |\mathbf{b}|}{D} \quad (3.7)$$

$$k_{\parallel} = \eta \frac{2\pi f_{21} H_0 E(z)}{c(1+z)^2} \quad (3.8)$$

where  $\lambda$  is the observing wavelength,  $k_B$  is the Boltzmann constant,  $D$  is the transverse comoving distance,  $\Delta D$  is the comoving depth along the line of sight corresponding to the bandwidth  $B$ ,  $f_{21}$  is the 21 cm line rest frequency,  $z$  is the redshift,  $H_0$  is the Hubble constant and  $E(z) = \sqrt{\Omega_M(1+z)^3 + \Omega_k(1+z)^2 + \Omega_{\Lambda}}$ . In this work, we use  $H_0 = 100 h \text{ km s}^{-1}$ ,  $\Omega_M = 0.27$ ,  $\Omega_k = 0$  and  $\Omega_{\Lambda} = 0.73$ . The power spectrum normalization volume  $q$  is (Thyagarajan et al., 2016):

$$q = \int_{\Omega} \int_B |a(\hat{\mathbf{r}}, \nu) w(\nu)|^2 d\Omega d\nu. \quad (3.9)$$

The polarized case is obtained by substituting equation 3.3 in the delay transform:

$$\tilde{\mathbf{v}}(\mathbf{b}, \tau) = \int_B w(\nu) \mathbf{v}(\mathbf{b}, \nu) e^{-2\pi i \nu \tau} d\nu \quad (3.10)$$

and by using the Hadamard (or element-wise) product  $\circ$  in order to extend equation 3.6 to four power spectra  $\mathbf{p} = (p_I, p_Q, p_U, p_V)^T$ :

$$\mathbf{p}(k) = \left(\frac{\lambda^2}{2k_B}\right)^2 \frac{D^2 \Delta D}{B} \mathbf{Q}^{-1} \{\tilde{\mathbf{v}}(|\mathbf{b}|, \tau) \circ \tilde{\mathbf{v}}(|\mathbf{b}|, \tau)^*\}. \quad (3.11)$$

As the off-diagonal elements of the  $\mathbf{A}$  matrix are much smaller than the diagonal elements, the normalization matrix  $\mathbf{Q}$  may be written as a diagonal matrix with diagonal elements:

$$\text{diag}(\mathbf{Q}) \approx \int_{\Omega} \int_B \text{diag}(\mathbf{A} w) [\text{diag}(\mathbf{A} w)]^* d\Omega d\nu. \quad (3.12)$$

Dimensionless polarized power spectra  $\Delta^2 = (\Delta_I^2, \Delta_Q^2, \Delta_U^2, \Delta_V^2)$  can be defined in analogy with the scalar case:

$$\Delta^2(k) = \frac{k^3}{2\pi^2} \mathbf{p}(k). \quad (3.13)$$

Equation 3.11 is one of the main results of our work: if the sky emission is unpolarized,  $p_I(k)$  reduces to  $p(k)$ , but appropriately combines the two orthogonal polarizations and their relative primary beams to form the total intensity power spectrum estimator. The remaining terms represent the visibility–based polarization power spectra which are dominated by leaked total intensity foreground emission.

In the presence of a polarized sky,  $p_I(k)$  naturally includes the leakage of polarized emission due to widefield primary beams. Equation 3.11 therefore generalizes the approach of Moore et al. (2013) to full polarization and provides a framework to simulate the expected leakage to the 21 cm power spectrum given both a polarized foreground and an instrument model.

## 3.2 Simulations

In order to evaluate equation 3.11 we need three ingredients: a model of the PAPER dipole beam, an array configuration and a polarized sky model.

We used the FEKO<sup>3</sup> package in order to obtain a model of the PAPER x–y complex dipole patterns in the 100–200 MHz range, spaced 10 MHz apart. The model is based on the dipole physical dimensions and includes a reflective mesh positioned above the ground. Examples of the corresponding  $\mathbf{A}(\hat{\mathbf{r}}, \nu)$  matrices are shown in Figure 3.1 whereas Figure 3.2 shows the frequency behavior of the first row of  $\mathbf{A}(\hat{\mathbf{r}}, \nu)$  (first three elements) for a few selected lines of sight. The  $A_{00}(\hat{\mathbf{r}}, \nu)$  term has a smooth frequency behavior that decreases slowly and monotonically from zenith to the horizon. This behavior is qualitatively in agreement with the beam model presented in Parsons et al. (2010), although we defer a more quantitative comparison to future work. The off-diagonal terms representing the leakage to Stokes I have a more complex spatial and spectral behavior: their magnitude is essentially negligible at zenith (where the instrument

<sup>3</sup><https://www.feko.info/product-detail>

points) whereas it becomes more than 10% already at  $70^\circ$  altitude.

We used the configuration of the PAPER 32-element imaging array (Stefan et al., 2013; Jacobs et al., 2013; Kohn et al., 2016, Figure 3.3) to simulate a baseline distribution that covers a relatively wide range of  $k_\perp$  values while retaining the 30 m baseline sample used in the estimate of the 21 cm power spectrum (Parsons et al., 2014; Jacobs et al., 2015; Ali et al., 2015).

We simulated a drift scan observation corresponding to actual PAPER 21 cm observations, i.e. spanning the  $0^{\text{h}} < \text{LST} < 8.5^{\text{h}}$  range with a 10 minute cadence, covering the 120–180 MHz frequency range with 500 kHz wide channels. For each frequency channel, the simulated  $\mathbf{A}$  matrices were obtained by averaging over the two closest frequencies at which the FEKO simulations were carried out.

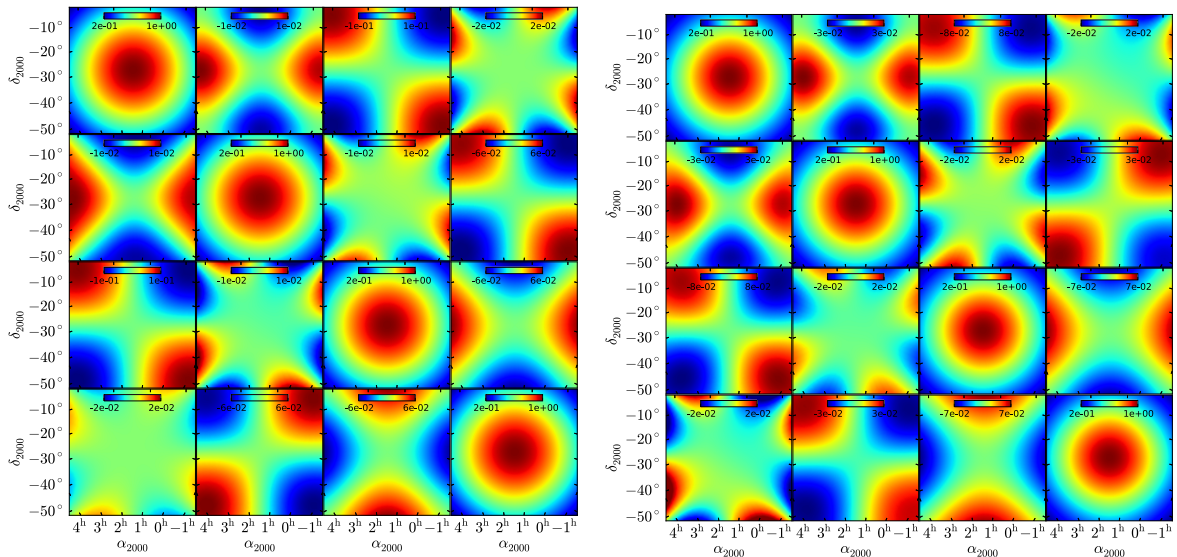


Figure 3.1:  $\mathbf{A}$  matrices simulated at 130 (left) and 150 MHz (right) respectively. From the simulated complex dipole patterns,  $\mathbf{A}$  matrices are computed in the altitude–azimuth coordinate system with the  $x$  dipole assumed to be aligned East–West. Here they are resampled on an  $(l, m)$  regular grid over a  $45^\circ$  field of view, centered at an arbitrary right ascension  $\alpha = 1^{\text{h}}24^{\text{m}}$  - the declination remains fixed at the telescope location  $\delta = -30^\circ43'17''$ . Resampling is carried out through a weighted average amongst the three closest points, with weights equals to the inverse distance to the  $(l, m)$  grid point.

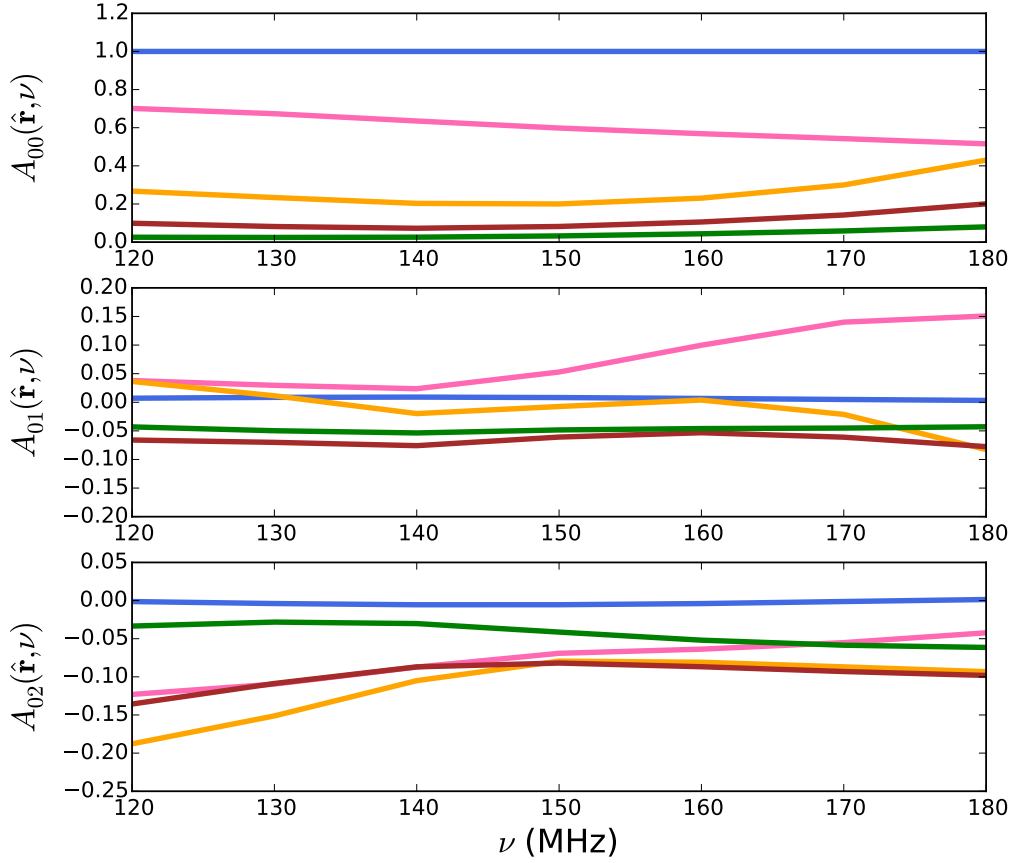


Figure 3.2: Spectral behavior of the  $\mathbf{A}$  matrix (first row only) along a few selected lines of sight  $\hat{\mathbf{r}}$  corresponding to a  $20^\circ$  azimuth and  $90^\circ$  (blue),  $70^\circ$  (pink),  $50^\circ$  (orange),  $30^\circ$  (brown) and  $10^\circ$  (green) altitude respectively. The  $A_{00}(\hat{\mathbf{r}}, \nu)$  term is normalized to unity at zenith by construction. The  $A_{03}(\hat{\mathbf{r}}, \nu)$  term is not included as no Stokes V sky emission is assumed throughout the chapter.

For each time sample, frequency channel and baseline we performed the following operations:

1. generated the sky emission evaluating equation 3.2, where the sky model consists of either a catalogue of point sources or a realization of diffuse Galactic emission (see Sections 3.2.1 and 3.2.2 below);

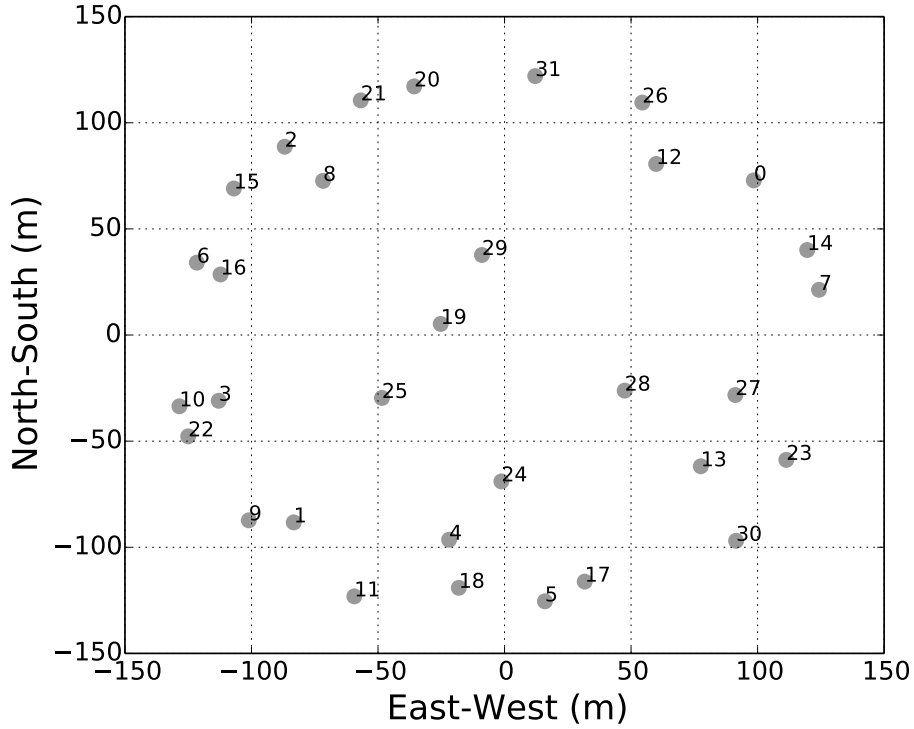


Figure 3.3: Array layout used for our simulations.

2. simulated visibilities via a discrete Fourier transform implementation of equation 3.3;
3. generated delay-transformed visibilities via a fast Fourier transform implementation of equation 3.10 where we used a Blackmann–Harris window function;
4. computed power spectra using equation 3.11.

In the following sections we describe the input foreground models to our simulations.

### 3.2.1 Point source all-sky model

Our simulations of polarized point sources are completely defined by a catalogue that includes both the polarization fraction and the rotation measure (RM) values. Stokes  $Q$  and  $U$  parameters

at any frequency  $\nu$ , for any source  $i$  can indeed be computed as:

$$\begin{aligned} Q_{\nu,i} &= \gamma_i I_{\nu,i} \cos(2\chi_i) = \gamma_i I_{\nu_0,i} \left(\frac{\nu}{\nu_0}\right)^{\alpha_i} \cos\left(2 \text{RM}_i \frac{c^2}{\nu^2}\right) \\ U_{\nu,i} &= \gamma_i I_{\nu,i} \sin(2\chi_i) = \gamma_i I_{\nu_0,i} \left(\frac{\nu}{\nu_0}\right)^{\alpha_i} \sin\left(2 \text{RM}_i \frac{c^2}{\nu^2}\right) \end{aligned} \quad (3.14)$$

where  $\chi_i$  is the polarization angle,  $\gamma$  is the polarization fraction,  $I_{\nu_0}$  is the flux density at the  $\nu_0$  reference frequency and  $\alpha$  is the spectral index. We note that the knowledge of the absolute polarization angle is not necessary for the purpose of estimating the 21 cm power spectrum leakage, therefore we set it to be zero along each line of sight. The change in the polarization angle as the source moves across the telescope beam does not need to be taken into account in our simulations as we compute the power spectra for each instant.

For the total intensity properties we used the [Hurley-Walker et al. \(2014\)](#) catalogue that lists all the sources brighter than 120 mJy at 150 MHz and covers the Southern Hemisphere at  $-58^\circ < \delta < -14^\circ$ . Although this catalogue is only somewhat deep, it has the advantage of providing the actual source locations, flux densities and spectral indexes in the 100–200 MHz band. From the [Hurley-Walker et al. \(2014\)](#) catalogue it is possible to generate a polarized catalogue assuming the RM and polarization fraction statistics respectively. Detailed, wide-area information on the low-frequency polarization properties of radio sources are still lacking to date, therefore we constructed a polarized catalogue derived from statical properties measured at higher frequencies.

The RM distribution was taken from the 1.4 GHz catalogue by [Taylor et al. \(2009\)](#), one of the most comprehensive polarization catalogues to date. For high Galactic latitude sources ( $|b| > 20^\circ$ ), the RM distribution fairly follows a Gaussian profile, with values as high as  $\sim |100| \text{ rad m}^{-2}$  (Figure 3.4). As the rotation measure is the integral of the magnetic field along the line of sight weighted by the electron density, we do not expect it to change with frequency, therefore, for each simulated source, we assigned an RM value drawn from the Gaussian best fit to the RM distribution of the high Galactic latitude sources in the [Taylor et al. \(2009\)](#) catalogue.

The statistics of the polarization fraction  $\gamma$  is more uncertain as it is, instead, expected to

decrease with frequency due to internal Faraday dispersion (Burn, 1966). It is not, therefore, straightforward to extrapolate the average polarization fraction at 1.4 GHz as Faraday depolarization depends on the specific source physical conditions (e.g., geometry and magnetic field strength, Tribble, 1991). Recent observations (Bernardi et al., 2013; Mulcahy et al., 2014; Asad et al., 2016) have indeed started to show that the average polarization fraction of radio sources decreases from a few percent value at 1.4 GHz to less than 1% at 150 MHz. Lenc et al. (2016) present the most stringent constraints to date to be  $\langle \gamma \rangle \leq 0.32\%$  at 154 MHz, derived from a sample of 187 sources. We conservatively treated this result as a measurement rather than an upper limit and assigned a polarization fraction value drawn from a uniform distribution between 0 and 0.32% to each simulated source.

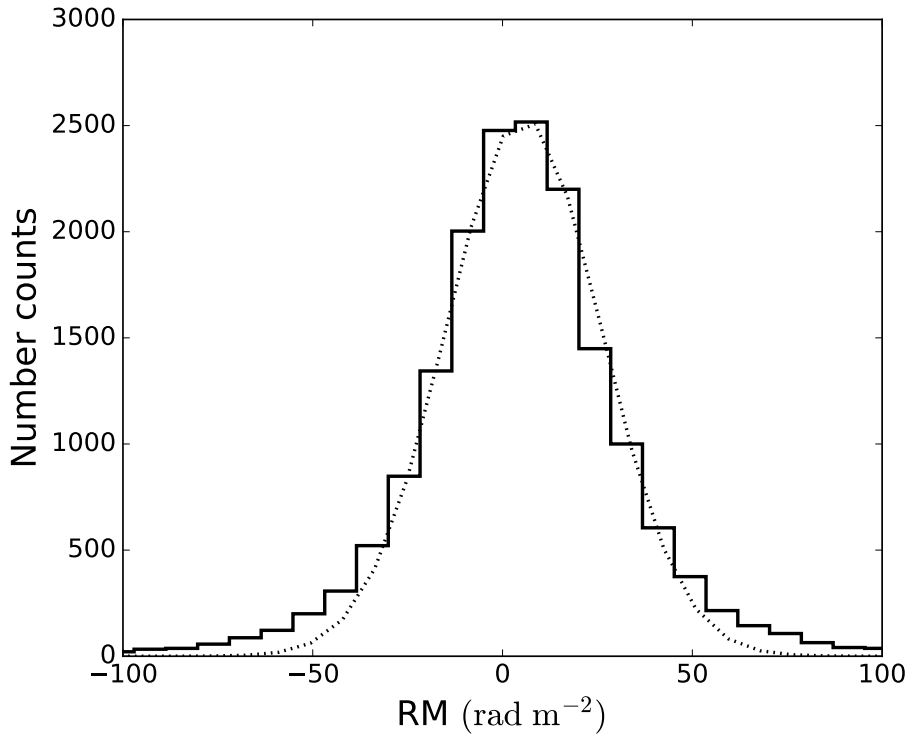


Figure 3.4: The RM distribution for sources at Galactic latitude  $|b| > 20^\circ$  from the Taylor et al. (2009) catalogue. The dotted line shows the Gaussian best fit with a  $5.6 \text{ rad m}^{-2}$  mean and a  $20 \text{ rad m}^{-2}$  standard deviation.

### 3.2.2 Galactic diffuse emission model

Observations of diffuse, Galactic polarized emission reveal a wealth of spatial structures in the interstellar medium (ISM) that are strongly frequency dependent. In particular, recalling that the Faraday depth  $\phi$  of a synchrotron emitting region between two points  $l_1$  and  $l_2$  along an arbitrary line of sight  $\hat{r}$ , given the electron density  $n_e$  and magnetic field along the line of sight  $B_{\parallel}$  is defined as (Burn, 1966; Brentjens & de Bruyn, 2005):

$$\phi(\hat{r}, l_1, l_2) = 0.81 \int_{l_1}^{l_2} n_e B_{\parallel} dl, \quad (3.15)$$

observations below a few hundred MHz show multiple polarized structures in the ISM at different Faraday depth values for almost any given line of sight. Jelić et al. (2010) and Alonso et al. (2014) have recently attempted to model this complexity, although a realistic description requires the knowledge of the distribution of the polarized emission both on angular scales and in Faraday depth, which is only partially emerging from recent observations (Bernardi et al., 2013; Jelić et al., 2014, 2015; Lenc et al., 2016).

In this work, we made the simplifying assumption to ignore the spatial and line-of-sight Faraday depth structure and consider the contribution from two representative Faraday depths integrated all the way to the observer’s location. With this approximation, the Faraday depth coincides with the RM and equation 3.14 can be used to obtain Stokes  $Q$  and  $U$  all-sky maps too:

$$\begin{aligned} Q(\hat{r}, \nu) &= P(\hat{r}) \cos\left(2\phi \frac{c^2}{\nu^2}\right) \\ U(\hat{r}, \nu) &= P(\hat{r}) \sin\left(2\phi \frac{c^2}{\nu^2}\right). \end{aligned} \quad (3.16)$$

The all-sky, polarized intensity map  $P$  could be, in principle, derived from a total intensity one, however, interferometric observations of polarized Galactic emission at all radio frequencies are known to suffer from the so called “missing short spacing problem”: they filter out the large scale, smooth background emission and retain the small scale, Faraday-rotated foreground structures introduced by local ISM fluctuations in either the electron density or the magnetic field (e.g., Wieringa et al., 1993; Gaensler et al., 2011). This effect leads to the lack of correlation between

total intensity and polarized diffuse emission, with an apparent polarization percentage exceeding 100% (e.g. [Gaensler et al., 2001](#); [Haverkorn et al., 2003](#); [Bernardi et al., 2003](#); [Schnitzeler et al., 2009](#); [Iacobelli et al., 2013](#); [Bernardi et al., 2010](#)), preventing us from using a total intensity template for polarization simulations.

In order to overcome this problem, we follow an approach similar to [Alonso et al. \(2014\)](#), who simulated a polarized foreground map  $P(\hat{r})$  at a reference frequency  $\nu_0$  from the polarized spatial power spectrum  $C_\ell^P$ :

$$\langle \tilde{P}(\mathbf{l}) \tilde{P}(\mathbf{l}')^* \rangle = (2\pi)^2 C_\ell^P \delta^{(2)}(\mathbf{l} - \mathbf{l}') \quad (3.17)$$

where  $\tilde{P}$  is the Fourier transform of  $P$ ,  $\mathbf{l}$  is the two dimensional coordinate in Fourier space,  $\langle \rangle$  is the ensemble average,  $\ell = \frac{180}{\Theta}$  with  $\Theta$  the angular scale in degrees and  $\delta^{(2)}$  is the two-dimensional Dirac function.

The synchrotron polarized power spectrum obtained from large-area, GHz-frequency surveys is well described by a power law (e.g., [La Porta et al., 2006](#); [Carretti et al., 2010](#)):

$$C_\ell^P = A_{\ell_0}^P \left( \frac{\ell}{\ell_0} \right)^{-\beta^P}, \quad (3.18)$$

down to  $\ell \sim 100 - 1000$ , with  $2 < \beta^P < 3$ . Due to the strong frequency dependence of the polarized emission (e.g. [Carretti et al., 2005](#)), the extrapolation to low frequencies is very uncertain.

[Bernardi et al. \(2009\)](#) and [Jelić et al. \(2015\)](#) measured the polarized spatial power spectrum at 150 MHz and found it to follow a power law with  $\beta^P = -1.65$  in the  $100 \leq \ell \leq 2700$  range, somewhat flatter than the higher frequency values. We therefore adopted this value for our simulations. As they both observed a relatively small ( $6^\circ \times 6^\circ$ ) sky patch, their measurement of the power spectrum amplitude  $A_{\ell_0}^P$  may be sample variance limited, therefore we constrained it by using the 2400 square degree survey carried out at 189 MHz by [Bernardi et al. \(2013\)](#). The survey shows significant difference in the levels of polarized emission as a function of Galactic latitude, with maximum emission around the south Galactic pole and mostly concentrated at  $|\phi| < 12 \text{ rad m}^{-2}$ . We identified the  $20^\circ \times 20^\circ$  area centered at  $(l, b) \sim (200^\circ, -80^\circ)$  to be the brightest polarized emission region in the survey and selected the  $\phi = 6, 12 \text{ rad m}^{-2}$  frames

as the brightest frame and the representative of a typical high  $\phi$  value for diffuse emission, in good agreement with the distribution of Faraday depth peaks recently measured in the Southern Galactic pole area at 154 MHz by [Lenc et al. \(2016\)](#). We labeled the models corresponding to these two frames as  $D6$  and  $D12$  and measured their polarized intensity root-mean-square (rms) to be  $P_{\text{rms},D6} = 1$  K and  $P_{\text{rms},D12} = 0.21$  K at  $\phi_{D6} = 6$  rad m<sup>-2</sup> and  $\phi_{D12} = 12$  rad m<sup>-2</sup> respectively. The power spectrum amplitude  $A_{D6,D12}$  was obtained through its relationship with the measured rms value (e.g., [Zaldarriaga et al., 2004](#)):

$$\begin{aligned} P_{\text{rms},D6,D12} &= \sqrt{\sum_{\ell_1}^{\ell_2} \frac{(2\ell + 1)}{4\pi} C_{\ell,D6,D12}^P} \\ &= \sqrt{\sum_{\ell_1}^{\ell_2} \frac{(2\ell + 1)}{4\pi} A_{D6,D12} \left(\frac{\ell}{\ell_0}\right)^{-\beta_P}}, \end{aligned} \quad (3.19)$$

where we dropped the  $\ell_0$  subscript for clarity and the exclusion of short baselines and the angular resolution of the [Bernardi et al. \(2013\)](#) survey set  $\ell_1 \sim 100$  and  $\ell_2 \sim 680$  respectively.

At this point we have all the necessary ingredients to generate the two  $D6$  and  $D12$  realizations of the diffuse polarized emission model using equation 3.16. We generated a map  $P_{D6}(\hat{\mathbf{r}})$  ( $P_{D12}(\hat{\mathbf{r}})$ ) from the polarized power spectrum  $C_{\ell,D6}^P$  ( $C_{\ell,D12}^P$ ) using the Healpix ([Górski et al., 2005](#)) routine SYNFAST. We chose an  $N_{\text{side}} = 128$  parameter that retains sufficient sampling for the 30 m baseline used for power spectrum estimation. We then substituted  $\phi_{D6}$  ( $\phi_{D12}$ ) in equation 3.16 to generate the Stokes  $Q$  and  $U$  full-sky maps corresponding to the  $D6$  ( $D12$ ) model realization.

### 3.3 Results

In this section, we compare our simulations with existing observations ([Kohn et al., 2016](#)), following which we predict the leakage expected in 21 cm power spectrum measurements. We then provide constraints on the average point source polarization fraction based on the data from [Moore et al. \(2015\)](#).

### 3.3.1 Polarized Power Spectra

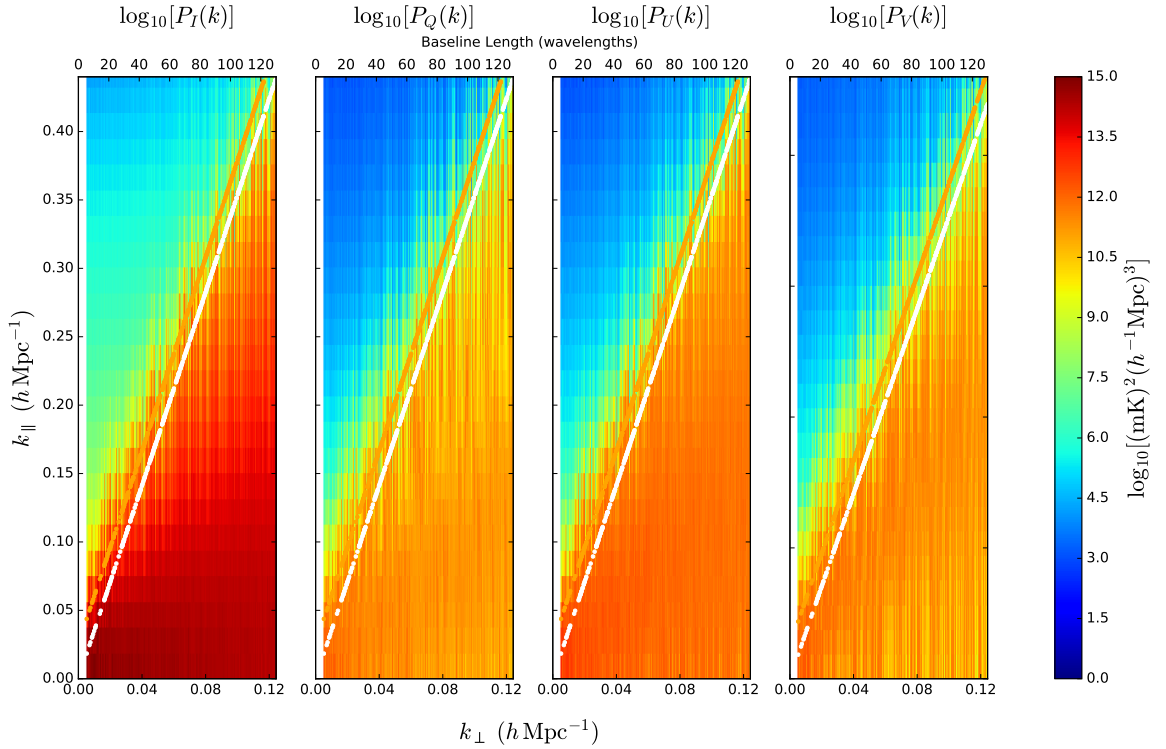


Figure 3.5: Two–dimensional power spectra  $\mathbf{p} = (p_I, p_Q, p_U, p_V)$  (left to right) over a 25 MHz bandwidth centered at 150 MHz, obtained from the brightest 1500 unpolarized total intensity sources from the [Hurley-Walker et al. \(2014\)](#) catalogue. The simulation only includes Stokes I; Stokes Q, U and V are leakages due to the instrumental widefield effects. The white line marks the horizon limit and the orange line is 50 ns beyond.

We first tested our simulation framework with a sky model composed of total intensity sources from the [Hurley-Walker et al. \(2014\)](#) catalogue. In this case we expected to reproduce the well established two–dimensional wedge–like total intensity power spectrum  $p_I$  observed, for example, in [Pober et al. \(2013\)](#), [Thyagarajan et al. \(2015\)](#) and [Kohn et al. \(2016\)](#). Figure 3.5 displays power spectra from this simulation using only the 1500 brightest sources down to a flux density threshold of 2 Jy. Power spectra change by only a few percent with the inclusion of all the sources down to the 120 mJy catalogue threshold, therefore the decreased computing load in using only the 1500 brightest sources merits the small loss in accuracy for the aim of this work.

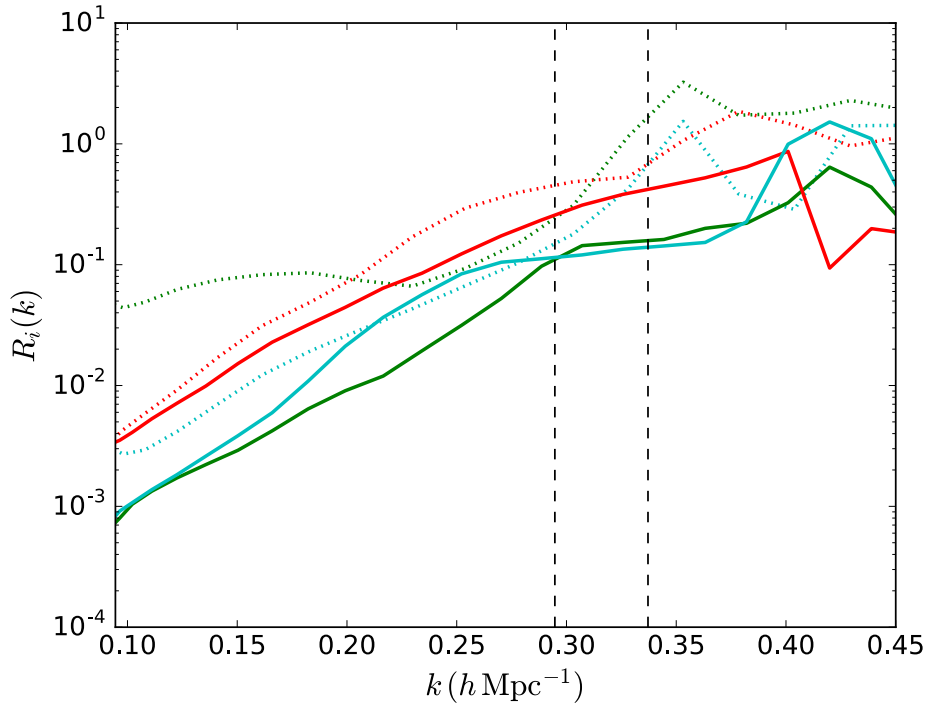


Figure 3.6: Ratios of Stokes  $Q$  (solid green),  $U$  (solid red) and  $V$  (solid cyan) versus  $I$  power spectra averaged over a  $0.092 < k_{\perp} < 0.097 h \text{ Mpc}^{-1}$  region, whose centre corresponds to a 175 m baseline. The dotted lines represent the corresponding power spectrum ratios from [Kohn et al. \(2016\)](#) observations (Figure 7 in [Kohn et al. \(2016\)](#))

. The left and right vertical dashed lines mark the horizon limit and 50 ns beyond it respectively.

The simulated total intensity power spectrum  $p_I$  shows the wedge-like morphology and power levels similar to [Pober et al. \(2013\)](#), confirming that our formalism is consistent with previous works that are limited to the total intensity case. Polarized power spectra display, in this case, the leakage from total intensity due to widefield polarized primary beams. All polarized power spectra have a similar behavior, with emission confined in a wedge-like shape very similar to total intensity. The power ratio between the emission inside and outside the wedge is at the  $10^9 - 10^{10}$  level, indicating that very little chromatic structure has been introduced by the primary beam outside the wedge.

In order to provide a first order validation of the beam models used in simulations, we com-

pared the ratio  $R_i$  of polarized versus total intensity power spectra defined as

$$R_i(k) = \frac{p_i(k)}{p_I(k)}, \quad \text{with } i = Q, U, V \quad (3.20)$$

calculated from our simulations and from power spectra measured in a 5 hour transit observation with PAPER (Kohn et al., 2016). The ratio is insensitive to a possible different absolute normalization between the simulation and data. Figure 3.6 shows that simulated  $R_i$  ratios are generally fainter than the measured ones, although the simulated  $R_U$  and  $R_V$  substantially agree with the measured ones. The measured power spectra show emission that extends up to 50 ns beyond the horizon limit, after which they appear to be noise-dominated (Kohn et al., 2016). As our simulations essentially have no emission beyond the horizon limit, this explains why both simulated and measured  $R_i$  approach unity outside the wedge. The largest difference between simulations and data appears in  $R_Q$  at  $k < 0.2 h \text{ Mpc}^{-1}$ , where our model underpredicts the measured value by more than one order of magnitude. This is the consequence of an excess of power found in  $p_Q$  at small  $k$  values by Kohn et al. (2016) that may be attributable to a calibration mismatch of the two orthogonal polarizations and, possibly, to intrinsic sky polarization not included in our simulations.

### 3.3.2 Predictions of polarization leakage

The simulation framework developed in this thesis eventually aims to predict the amount of leakage expected in the measured 21 cm power spectra. In order to do so, we carried out two sets of simulations for the models described in Sections 3.2.1 and 3.2.2 respectively, where we explicitly set the point source total intensity model to zero, so that  $p_I$  directly measures the leakage from polarized foregrounds. The resulting power spectra at  $z = 8.5$  (150 MHz) for a fiducial 30 m baseline are shown in Figure 3.7 and 3.8 respectively.

Polarized power spectra generated from the point source simulation exhibits significant super-horizon emission, i.e. almost constant power outside the  $k \sim 0.06 h \text{ Mpc}^{-1}$  horizon limit for a 30 m baseline (Figure 3.7). This behavior is expected from Faraday rotated foregrounds whose leakage is not confined in  $k_{\parallel}$  space. Power spectra also appear featureless in  $k$  space and this can

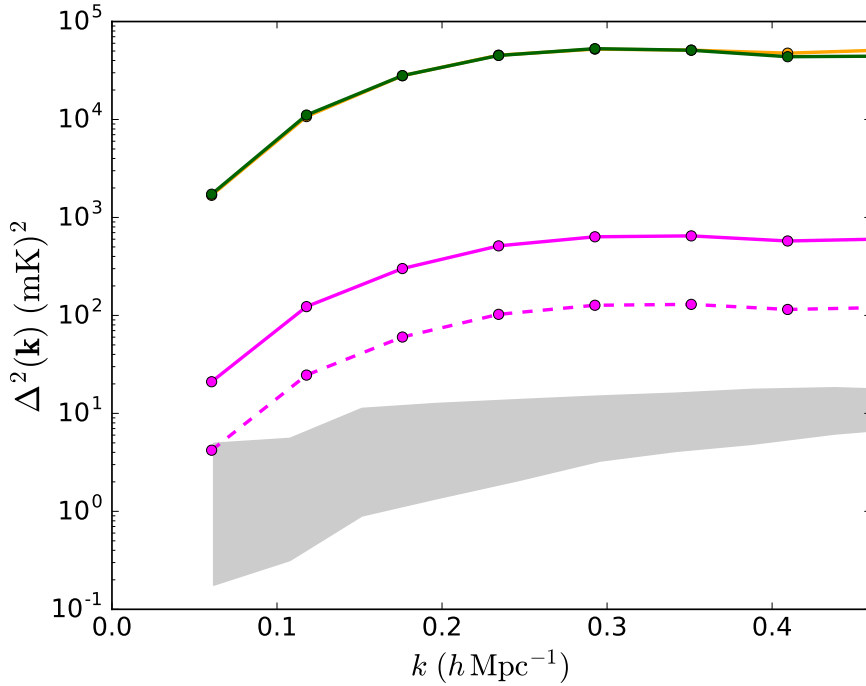


Figure 3.7: Polarized power spectra  $\Delta_{Q,U}^2$  (orange and green lines respectively) for a 30 m baseline and an 8 MHz bandwidth centered at 150 MHz ( $z = 8.5$ ) from a polarized point source sky model with the total intensity intentionally set to zero (see text for details). The magenta line represents  $\Delta_I^2$ , i.e. the predicted leakage to total intensity. The magenta dashed line shows the leakage when we assumed the polarization fraction to be distributed between 0 and 0.14%. The shaded gray region represents power spectra of the 21 cm fiducial model from Lidz et al. (2008) with HI neutral fractions ranging between 0.21 and 0.82.

be intuitively understood as a single RM value corresponds to a specific  $k_{\parallel}$  value (Moore et al., 2015):

$$k_{\parallel} = \frac{4 \lambda^2 H(z)}{c(1+z)} \text{RM}, \quad (3.21)$$

therefore, a population of point sources distributed over a broad range of RM values essentially displays power at any  $k_{\parallel}$  value. This is the reason why diffuse emission power spectra show a characteristic knee–shape as a function of  $k$  (Figure 3.8): by construction, they only have structure at  $\phi = 6$  and  $12 \text{ rad m}^{-2}$  corresponding to  $k_{\parallel} \approx 0.02$  and  $0.06 \text{ h Mpc}^{-1}$  respectively and their

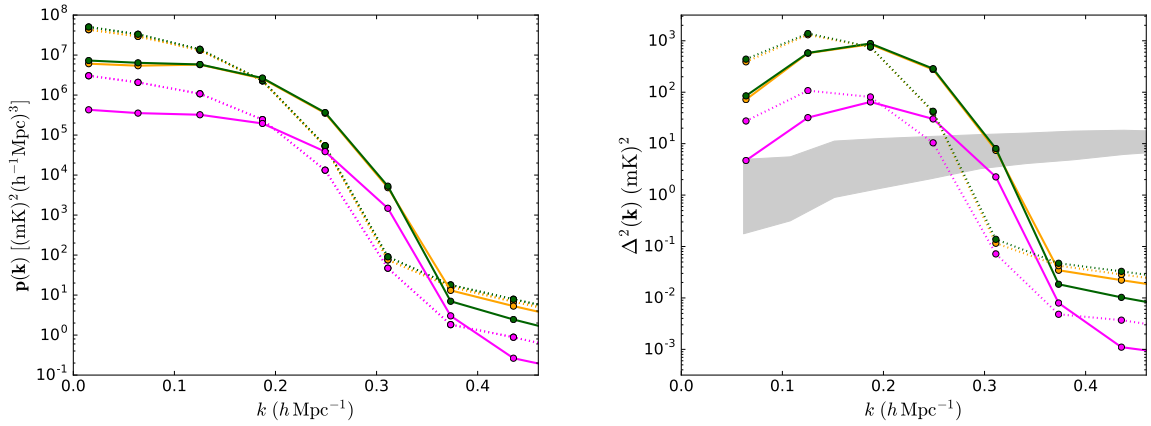


Figure 3.8: *Left panel:* Polarized power spectra  $P_{Q,U}$  (orange and green lines respectively) for a 30 m baseline and an 8 MHz bandwidth centered at 150 MHz ( $z = 8.5$ ) from the diffuse polarized foreground  $D12$  (solid) and  $D6$  (dotted). The magenta line represents the leaked power spectra  $P_I$ . *Right panel:* Same as left panel but for  $\Delta_{I,Q,U}^2(k)$ . The shaded gray region represents power spectra of the 21 cm fiducial model from Lidz et al. (2008) with HI neutral fractions ranging between 0.21 and 0.82.

power, therefore, falls off at higher  $k_{\parallel}$  values as illustrated in Figure 3.9. Noticeably, the  $D12$  model power spectrum is brighter than the  $D6$  one at  $k > 0.2 h \text{ Mpc}^{-1}$  despite its normalization being five times smaller (see Section 3.2.2), showing that the super-horizon contamination depends more on the  $\phi$  value rather than the intrinsic foreground brightness.

In terms of contamination to the 21 cm power spectrum, our predictions should be regarded as worst case scenarios, due to our conservative model assumptions. In both foreground models, leaked power spectra approximately behave as scaled versions of polarized power spectra, however, in the diffuse emission case, the leaked power spectrum is  $\sim 0.03 (\text{mK})^2$  for  $0.3 < k < 0.5 h \text{ Mpc}^{-1}$ , a reasonably negligible contamination to the 21 cm power spectrum. Bright, diffuse polarized foregrounds are therefore not a concerning contamination to the 21 cm power spectrum as long as their emission is confined at low Faraday depths as all the existing observations are showing (e.g. Bernardi et al., 2009, 2010, 2013; Jelić et al., 2014, 2015; Lenc et al., 2016). From a pure avoidance perspective, therefore, knowledge of the polarized point source

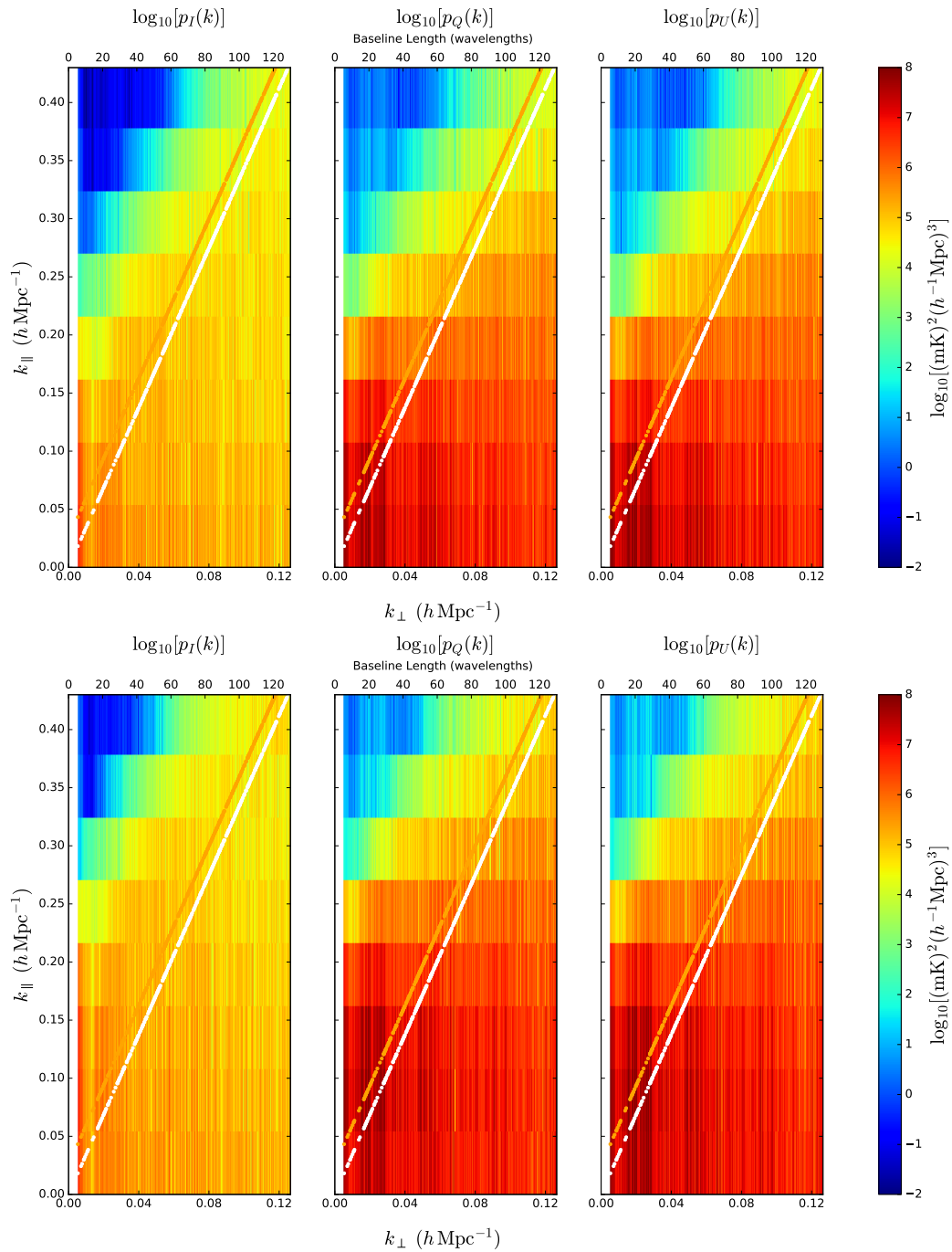


Figure 3.9: Polarized power spectra  $P_{I,Q,U}$  for an 8 MHz bandwidth centered at 150 MHz from the diffuse polarized foreground  $D6$  (upper panel) and  $D12$  (lower panel).

distribution is more relevant as it may contaminate high  $k$  modes too: its leakage magnitude is a strong function of the average point source polarization fraction, becoming one order of magnitude smaller if a uniform distribution with a maximum value of 0.14% is assumed (Figure 3.7, magenta dashed line). We will return to this point in the next section.

One natural by product of our formalism is the predicted fractional leakage  $f$  per  $k$  mode defined as the reciprocal of  $R_i$ :

$$f_i(k) = \frac{1}{R_i} = \frac{p_I(k)}{p_i(k)} \quad (3.22)$$

Figure 3.10 shows that the fractional leakage contributed by Stokes  $Q$  and  $U$  is less than 3% for  $k < 0.5 h \text{ Mpc}^{-1}$  in the  $8 < z < 10$  range and tends to increase with redshift. Moore et al. (2015) gave a simplified estimate of the fractional leakages that is consistent with ours within a factor of two.

Finally, we note that  $f_i$  has a rather different behavior as a function of  $k$  than  $R_i$ , while they should be, in first approximation, similar, due to the fact that the  $\mathbf{A}$  matrices are nearly symmetrical (Figure 3.1). There is an intrinsic difference due to the fact that the simulations presented here pertain to two different baselines, however, most of their difference is due to the input model. The unpolarized point source model (Figure 3.6) is very smooth in frequency by construction, leading to a very bright Stokes  $I$  power spectrum at small  $k_{\parallel}$  values and, therefore, a corresponding  $R_i$  at those modes; conversely, as mentioned above, the polarized point source model has power at essentially any  $k_{\parallel}$  value by construction, leading to an almost flat  $f_i$  as a function of  $k_{\parallel}$ .

### 3.3.3 Constraining the polarization fraction

We compared our predictions for the point source model - the worst expected contamination - with the polarized power spectrum measurements from a 30 m baseline deep integration with the PAPER-32 array (Moore et al., 2015). Their  $\Delta_{Q_m}^2$  and  $\Delta_{U_m}^2$  at 126 and 164 MHz (reported here in Figure 3.11) are essentially consistent with the noise level in the  $\Delta k = [0.2, 0.45] h \text{ Mpc}^{-1}$  range. We used these results to constrain our polarized power spectrum  $\Delta_Q^2$  to  $\Delta_{Q'}^2$  at the same

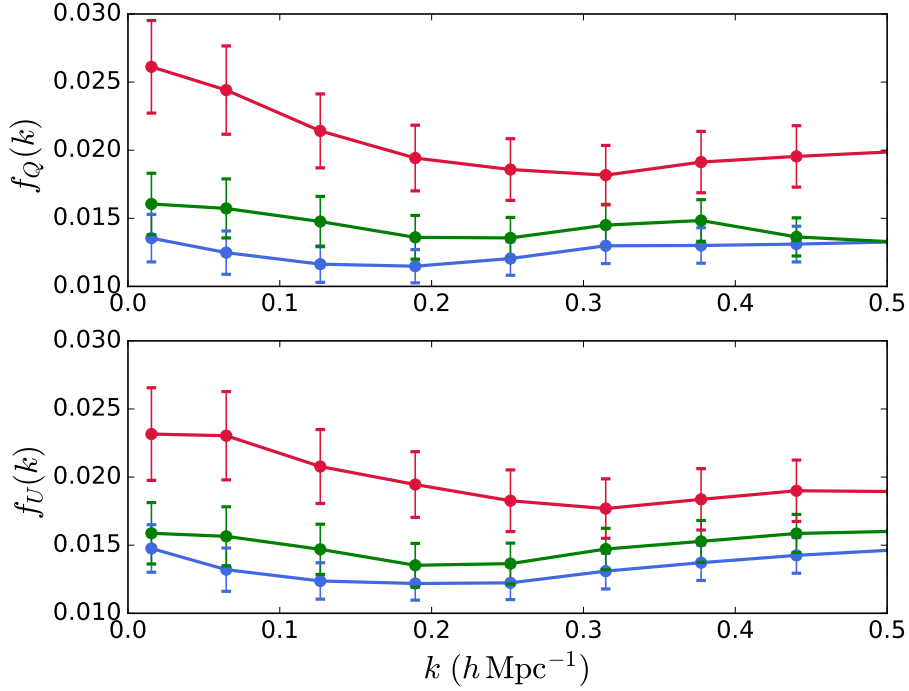


Figure 3.10: Stokes  $Q$  (top panel) and  $U$  (bottom panel) fractional leakage per  $k$  mode for a 30 m baseline estimated from the polarized point source model at  $z = 8$  (blue line),  $z = 9$  (green line) and  $z = 10$  (red line) respectively. Error bars were calculated as the standard deviation of ten random realizations of the model.

frequencies to be:

$$\Delta_{Q'}^2 = \frac{\langle \Delta_{Q,U}^2 \rangle_{\Delta k}}{\langle \Delta_{Q_m, U_m}^2 \rangle_{\Delta k}} \Delta_Q^2 = r \Delta_Q^2 \quad (3.23)$$

where  $\langle \rangle_{\Delta k}$  indicates the average over the  $\Delta k$  range for both Stokes parameters. Similarly,  $\Delta_{U'}^2$  is constrained to  $\Delta_{U'}^2$  at the corresponding frequencies. In order to be consistent with the data, the simulated power spectra need to be scaled down by, at least,  $r \sim 0.1$  at 126 MHz (Figure 3.11; left panel), whereas they are already consistent (i.e. fainter) with the measurements at 164 MHz (Figure 3.11; right panel).

These results can be used to improve our assumptions on the point source polarization fraction, allowing it to evolve with frequency. Defining  $\gamma_{126}$  the polarization fraction at 126 MHz

and recalling from equation 3.14 that

$$\Delta_{Q,U}^2 \propto \langle \gamma^2 \rangle \quad (3.24)$$

and

$$\langle \gamma^2 \rangle = \frac{2b}{3} \langle \gamma \rangle \quad (3.25)$$

if  $\gamma$  follows a uniform distribution between 0 and  $b$  ( $b = 0.32\%$  in this work), the comparison with the Moore et al. (2015) power spectra yields  $\langle \gamma_{126} \rangle \leq 0.1\%$ , approximately a factor of three smaller than our model assumption. It is interesting to note that such constraint qualitatively meets the expectations of Faraday depolarization models (Burn, 1966; Tribble, 1991) that predict the polarization fraction to decrease at longer wavelengths. Although the estimated leaked power spectra may still remain above the expected 21 cm power spectra, they are now more than one order of magnitude fainter than the initial model predictions.

One caveat of our comparison with real data is related to the role of ionospheric Faraday rotation. Moore et al. (2015) already pointed out that averaging visibilities over many days of observations to form polarized power spectra leads to significant depolarization due to time variable ionospheric Faraday rotation. Without any correction, polarized power spectra measured in an actual observation (e.g. Moore et al., 2015) can still be used to predict the leakage as we showed above, although they cannot be used to model the intrinsic sky properties and, therefore, straightforwardly predict the leakage contamination in a different 21 cm observation. In this respect, the constraints we placed on the average polarization fraction of extragalactic radio sources should be seen as constraints on the *effective* (i.e. modulated by ionospheric Faraday rotation) rather than the intrinsic fraction.

The effect of ionospheric Faraday rotation could be directly included in our formalism in equation 3.2 but we leave this for future work (Aguirre et al., in prep.).

### 3.4 Discussion and Conclusions

We have presented a formalism to extend the delay–spectrum, visibility–based power spectrum estimator to full polarization, including the effect of polarized foreground leakage due to wide-

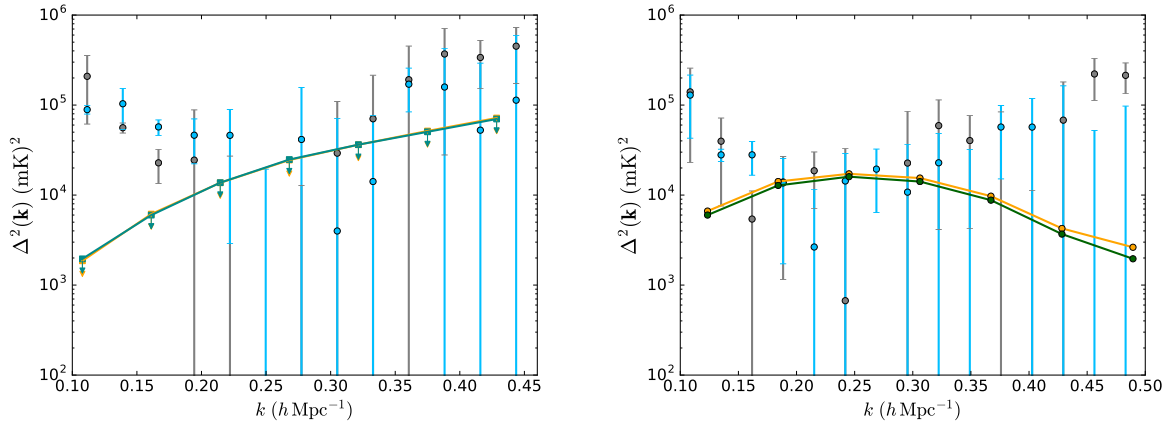


Figure 3.11: *Left panel:* Polarized power spectra  $\Delta_{Q'}^2$  and  $\Delta_{U'}^2$  (orange and green respectively) from our point source simulation scaled down to match the observed  $\Delta_{Q_m}^2$  and  $\Delta_{U_m}^2$  (blue and gray circles respectively) from Moore et al. (2015) at 126 MHz ( $z = 10.3$ ). *Right panel:* Polarized power spectra  $\Delta_{Q'}^2$  and  $\Delta_{U'}^2$  predicted from our point source simulation at 164 MHz ( $z = 7.7$ ) compared with the observed  $\Delta_{Q_m}^2$  and  $\Delta_{U_m}^2$  (blue and gray circles respectively) from Moore et al. (2015) at the same frequency. We note that our predictions are compatible with the observed upper limits.

field primary beams. We applied our formalism to simulate power spectra from PAPER-like observations. We first used a total intensity source catalogue, predicting polarized power spectra in general agreement with observations in Kohn et al. (2016). We then modeled polarized (Galactic and extragalactic) foregrounds using recent low frequency observations and predicted the corresponding power spectrum leakage, particularly focusing on the contamination for a 30 m baseline.

We found that an ‘‘EoR window’’ can be defined in terms of polarization leakage from diffuse Galactic foreground as its contamination falls quickly below  $\sim 1 \text{ (mK)}^2$  at  $k > 0.3 \text{ h Mpc}^{-1}$ , i.e. significantly below the fiducial range of 21 cm models. The existence of such EoR window is due to the fact that current observations find significant diffuse polarization only at low Faraday depths, i.e.  $\phi \lesssim 12 \text{ rad m}^{-2}$  corresponding to  $k_{\parallel} \lesssim 0.06 \text{ h Mpc}^{-1}$ . Bright, diffuse emission found at high Faraday depth values would appear at proportionally higher  $k_{\parallel}$  modes, narrowing

(or jeopardizing) the EoR window. Current deep observations, however, set the presence of polarized diffuse emission to be below  $\sim 0.1$  K at  $\phi > 5$  rad m<sup>-2</sup> (Jelić et al., 2015), supporting our model assumptions.

In the case of point source leakage, an EoR window cannot be identified because point sources show emission essentially at any  $k_{\parallel}$  value due to their broad RM distribution, making polarized point sources a potentially more serious contamination than diffuse emission. The magnitude of such leakage depends, however, significantly on the average point source polarization fraction for which only upper limits are currently available in the 100-200 MHz range. By treating such upper limits as actual measurements, our model predicts a worse case scenario where point source polarization leakage is higher than the contamination due to Galactic emission at any  $k$  mode for a 30 m baseline. For  $k > 0.15$  hMpc<sup>-1</sup> our predicted upper limits are at the same level as the 21 cm upper limits measured by Ali et al. (2015).

The comparison with polarized power spectra from Moore et al. (2015) constrains the observed (i.e. uncorrected for ionospheric Faraday depolarization) average polarization fraction at  $\nu = 126$  MHz to be  $\langle \gamma \rangle < 0.1\%$ , leaving upper limits to the 21 cm leakage that are between one and two orders of magnitude greater than the 21 cm signal in the  $7.7 < z < 10.3$  range.

Our current simulations do not include the depolarization effect due to ionospheric Faraday rotation average over multiple nights of observations, therefore all our predictions should be regarded as worst cases in terms of contamination to the 21 cm power spectrum.

Finally, our work provides a tool to predict the level of leakage expected in actual 21 cm observations by *forward modeling* the polarized foreground emission through the instrument model (see Pindor et al., 2011; Bernardi et al., 2011; Sullivan et al., 2012, for relevant examples): in the case of polarized point sources, for example, the observed average polarization fraction needs to be known in order to predict the leakage. We indicate three ways to determine the observed average polarization fraction:

- by best fitting the predicted polarized power spectra to the polarized power spectra measured in actual observations as we showed here with the Moore et al. (2015) data;
- by imaging the polarized sky without correcting for ionospheric Faraday rotation: this

directly provides a measurement of the average point source polarization fraction;

- by applying an ionospheric Faraday rotation model to a polarized point source model realization whose average polarization fraction is provided by independent observations.

Although future predictions might require further corrections to this first order picture, our model offers a way to account for polarization leakage in 21 cm power spectrum observations to be applied to future observations with PAPER, the Hydrogen Epoch of Reionization Array ([DeBoer et al., 2017](#)) and, potentially, the Square Kilometre Array ([Koopmans et al., 2015](#)).

---

## All-sky Imaging with PAPER-128<sup>1</sup>

---

The Donald C. Backer Precision Array to Probe the Epoch of Reionization (PAPER, [Parsons et al., 2010](#)) is a radio interferometer built to detect the 21 cm Hydrogen line from cosmic reionization. It is located in the Karoo desert ( $S30^{\circ}43'17.5''$   $E21^{\circ}25'41.9''$ ) in the Northern Cape province of South Africa, about 60 km west of the town called Carnarvon where the Karoo Array Telescope ([Foley, 2010](#)) and the MeerKAT telescope ([Foley, 2010](#); [Brederode et al., 2016](#)) are located. In this chapter we present the analysis of the data taken with the 128-element PAPER array with a view to characterize the EoR foregrounds.

### 4.1 Array configuration and data acquisition

The PAPER array with 128 elements (Figure 4.1) consists of 112 dipoles arranged in a  $16 \times 7$  rectangular grid to offer maximum redundancy and 16 dipoles, referred to as outriggers, placed along a perimeter of 300 m (Figure 4.2). The purpose of the outriggers is to improve the  $uv$ -coverage (Figure 4.3). The antenna feed consists of crossed dipoles sandwiched between aluminum sleeves

---

<sup>1</sup>*Nunhokee, C. D. et al., in prep*

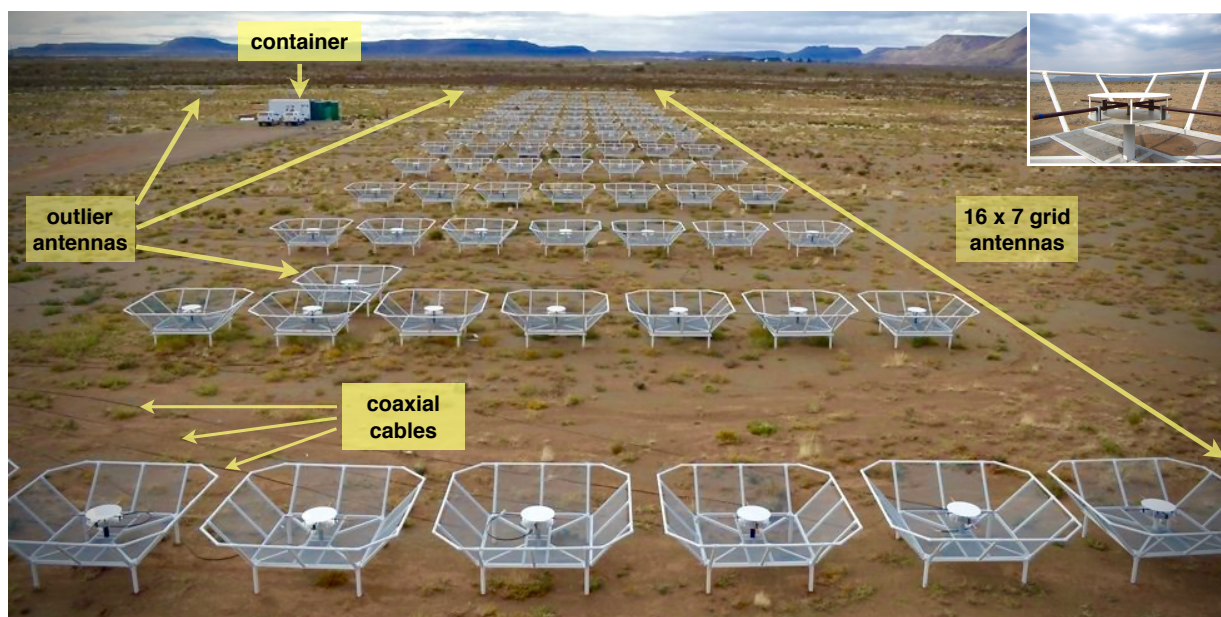


Figure 4.1: PAPER-128 site in the Karoo desert, shows the redundant grid layout. The container houses the backend electronics of the array. *Inset*: PAPER crossed dipoles sandwiched between aluminum sleeves.

to broaden the frequency range in order to span the 100–200 MHz range. This assembly is mounted on a 45° elevated wire-mesh that acts as a ground screen. Figure 4.4 illustrates the signal chain and the digital backend of PAPER.

	<b>Epochs</b>	<b>Julian Dates</b>	<b>Calendar Dates</b>
<b>Season 1</b>	1	2456617 - 2456673	Nov 20, 2013 - Jan 15, 2014
	2	2456678 - 2456724	Jan 20, 2014 - Mar 7, 2014
<b>Season 2</b>	1	2456725 - 2456835	Mar 8, 2014 - Jun 26, 2014
	2	2456836 - 2456875	Jun 27, 2014 - Aug 5, 2014
	3	2456881 - 2456929	Aug 11, 2014 - Sep 28, 2014
	4	2456941 - 2457995	Oct 10, 2014 - Dec 3, 2014
	5	2457996 - 2457073	Dec 9, 2014 - Feb 19, 2015

Table 4.1: Breakdown of PAPER-128 observing seasons.

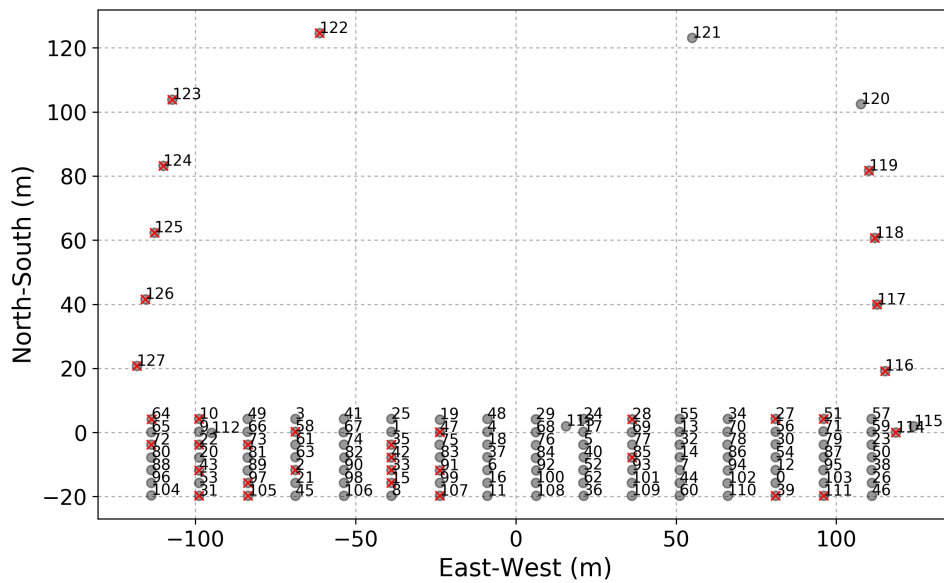


Figure 4.2: Antenna layout of PAPER-128. Antennas highlighted in red were found to be malfunctioning.

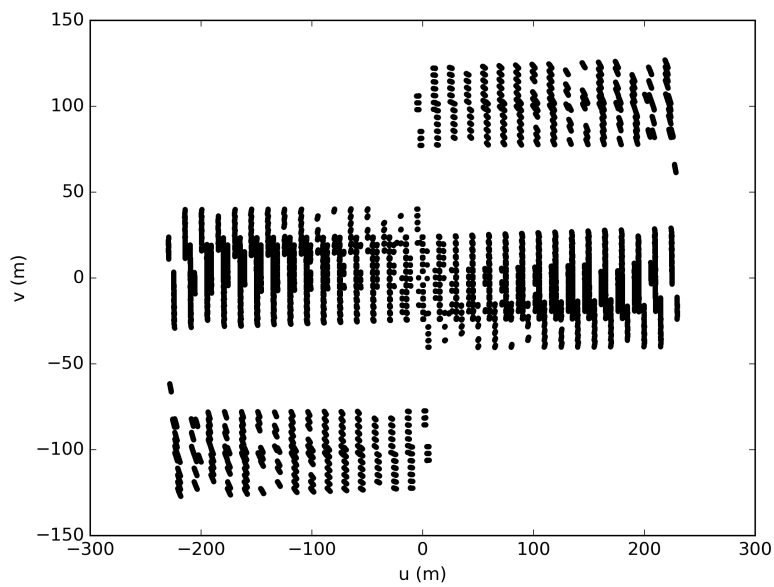


Figure 4.3:  $uv$  coverage for a 10 minute observation at 150 MHz.

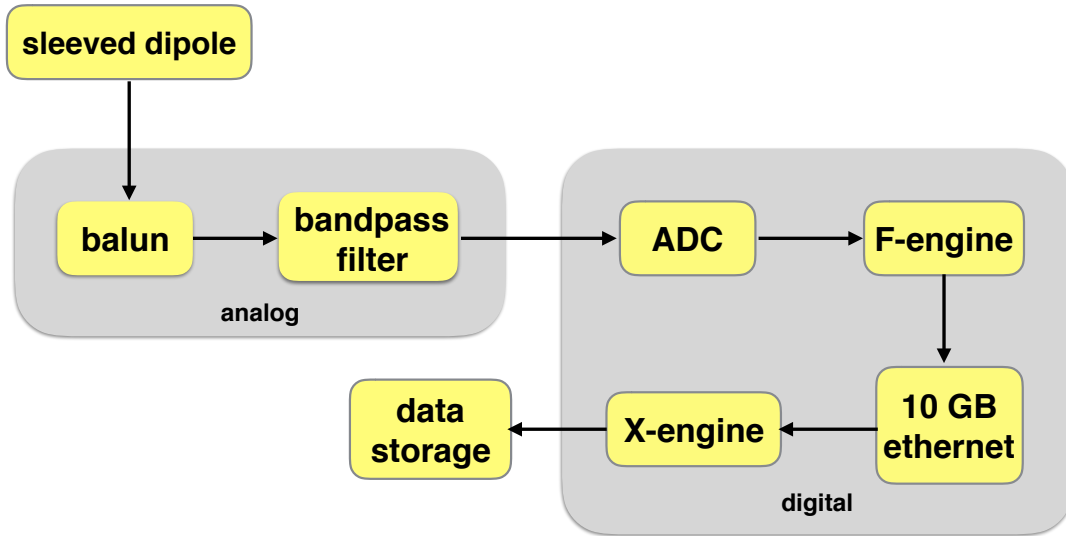


Figure 4.4: Schematic of the stages involved in processing the signal received at one sleeved PAPER dipole.

Observations using PAPER-128 were carried out from November 2013–January 2015. The entire duration of the observation is split into two seasons that consists of multiple epochs (refer Table 4.1). In this chapter we present the analysis of the first epoch of the first season, corresponding to 40 days.

## 4.2 Flagging and calibration

The first stage of the data analysis is identification and excision of bad data. Initially, we flagged the frequency band edges due to bandpass filter roll-off and the channels known to be affected by RFI due to satellite transmissions. All of the malfunctioning dipoles were permanently flagged (Figure 4.2). Impulsive and narrow-frequency RFI was further flagged using the *tfcrop* algorithm implemented in the Common Astronomy Software Applications (CASA) package. The *tfcrop* algorithm auto detects and flags outliers from the data on a 2D time-frequency plane. Each per baseline and per polarization visibility spectrum is averaged across all the timestamps for a 10 minute snapshot to construct an average bandpass. Further, an estimate of RFI-free band-

pass via a robust piecewise polynomial is fitted to the previously computed average bandpass (for more details refer <https://casa.nrao.edu/Release3.4.0/docs/userman/UserMansu161.html>). The RFI-free bandpass is then divided from visibilities for each timestamp to distinguish the narrow-band RFI spikes from a smoothly-varying bandpass. Any resulting value that deviates significantly from a mean of one is treated as RFI and thus, flagged.

After flagging, we carried out interferometric calibration. The inclusion of outrigger dipoles make the array non redundant, therefore we could not take advantage of redundant calibration (i.e., [Zheng et al., 2014](#)) unlike previous PAPER observations ([Parsons et al., 2014](#); [Ali et al., 2015](#)), but employed a more traditional sky-based approach.

Traditional sky-based calibration is based on the observation of a calibrator, a point source with known properties, isolated from other sources so that it essentially constitutes the whole sky model. This condition is not easily met in PAPER observations as its field of view is so large that no source is isolated. As a result, a fairly complex sky model may be needed for accurate calibration. As a first step towards calibration, we used a sky model constituted by the Pictor A ( $\alpha = 5^{\text{h}}20^{\text{m}}24^{\text{s}}$ ,  $\delta = -45^{\circ}46^{\text{m}}48^{\text{s}}$ ) radio source alone. The motivation behind this choice is that Pictor A is the brightest source (still unresolved at the angular resolution of our observations) within the field of view and for which a well measured spectrum is available ([Jacobs et al., 2013](#)). We will show that, despite its shortcomings ([Yatawatta et al., 2013](#); [Grobler et al., 2014](#)), this simple approach leads to a satisfactory first order calibration.

For each day we performed the following calibration steps:

1. selected the 10 minute-long (“snapshot”) observation where Pictor A is closest to transit as it has the highest signal to noise ratio;
2. generated model visibilities by Fourier transforming the Pictor A point source model, assumed to have a constant 1 Jy flux density across the observing band;
3. solved for antenna-based complex gains as a function of frequency using the CASA *bandpass* task. The solution interval was set to 10 minutes and all the baselines shorter than  $12\lambda$  were excluded as they are more sensitive to diffuse emission that was not included in the sky model;

4. applied the complex gains to form calibrated visibilities.

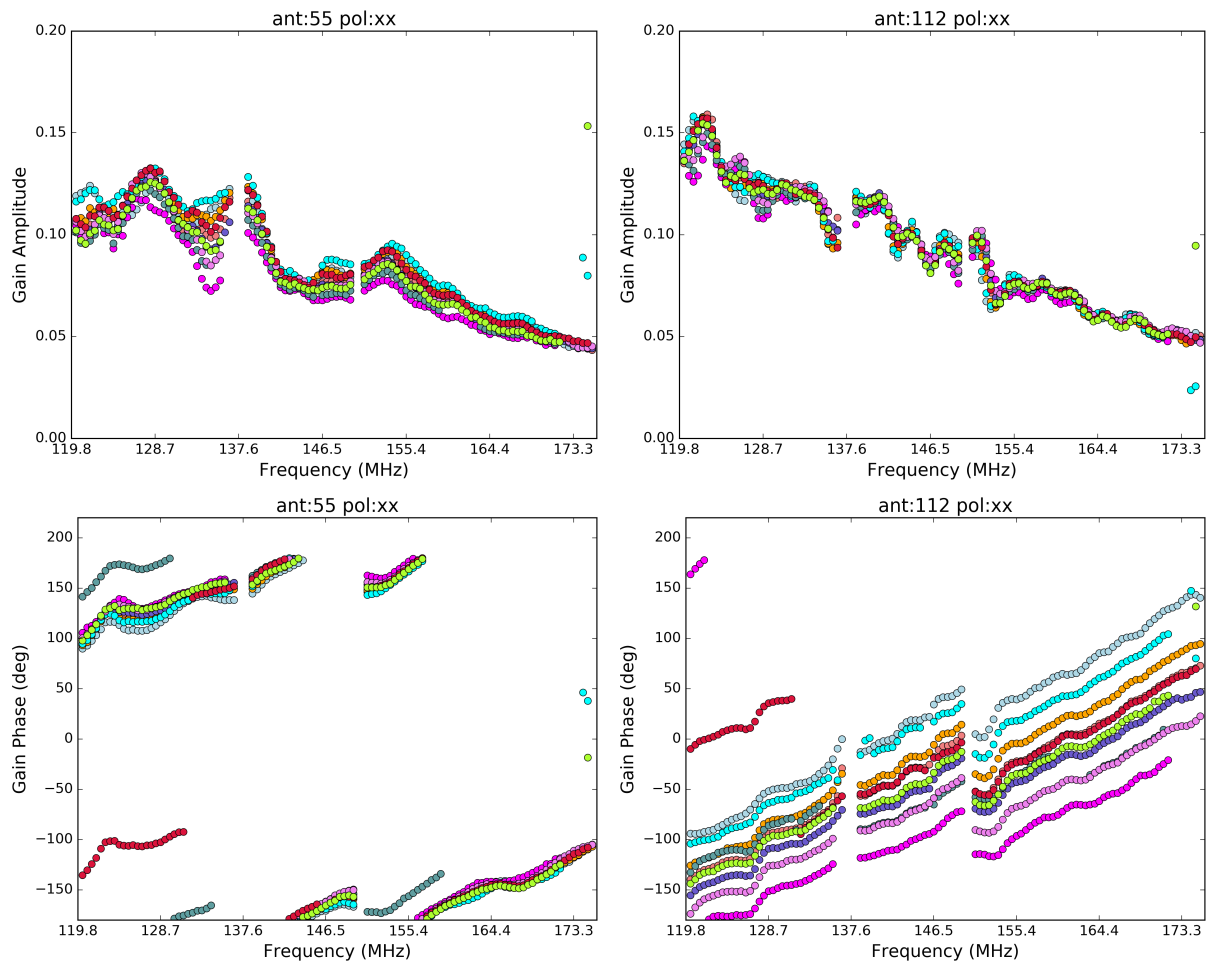


Figure 4.5: Gain amplitudes (top) and phases (bottom) for the xx polarization as a function of frequency for dipoles 55 (left column) and 112 (right column) respectively. Different days are identified with different colors.

Solutions for the yy polarization were persistently bad between 120 and 132 MHz, therefore, the corresponding frequency channels were flagged. There is no obvious RFI contaminations in those channels, therefore further investigation is required as we did not obtain meaningful gain solutions for them. Examples of solutions are shown in Figure 4.5 and 4.6. Gains solutions are fairly similar for different days, showing a fair instrument stability. Slopes in the gain phases are due to uncorrected cable delays.

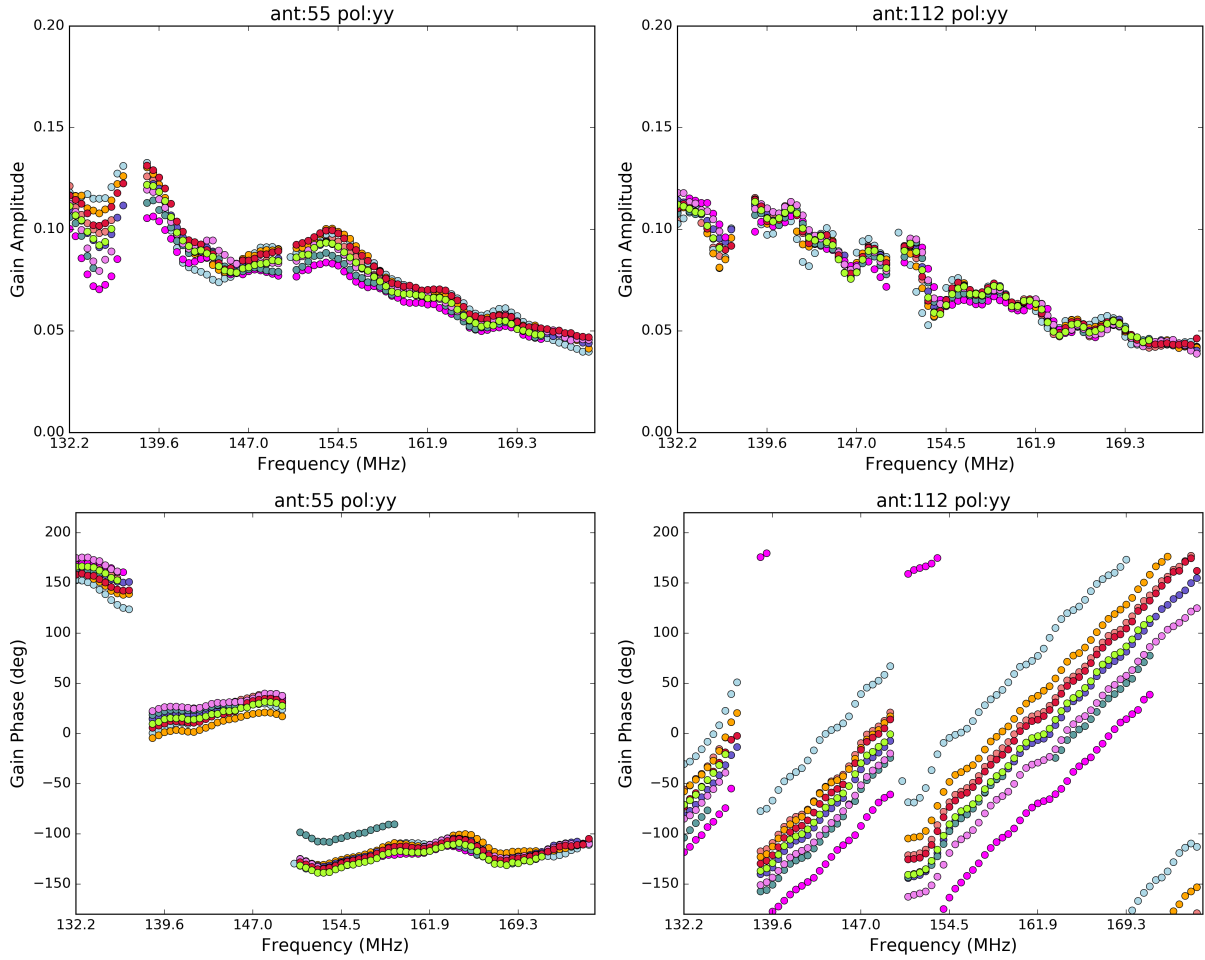


Figure 4.6: Same as Figure 4.5 for the yy polarization.

Calibrated visibilities for each snapshot were Fourier transformed into individual images with a  $\sim 51^\circ$  field of view. Uniform weighting was applied to the gridded visibilities in order to minimize contaminations from sidelobes. The multi-frequency synthesis algorithm (Conway & Sault, 1995) was used on a bandwidth between 120 and 175 MHz generating images centered at 146.5 MHz. The non-coplanarity of the array was corrected through the  $w$ -projection algorithm (Cornwell & Bhatnagar, 2005) by setting the  $w$  terms to 32. Each image was deconvolved using the Cotton-Schwab algorithm iteratively until a threshold of 100 mJy was reached, when the deconvolution model had its first negative component. The resulting models were used to generate model visibilities, which were subtracted from the calibrated data to form residual visibilities.

The real part of residual visibilities was then binned and a Gaussian profile was fitted to the distribution (plotted in Figure 4.7). Only baselines greater than 30 m were used. The distributions follow a fairly good Gaussian profile, as expected in the case of instrumental thermal noise. Data points below and above  $5\sigma$  were flagged and bandpass solutions were derived again.

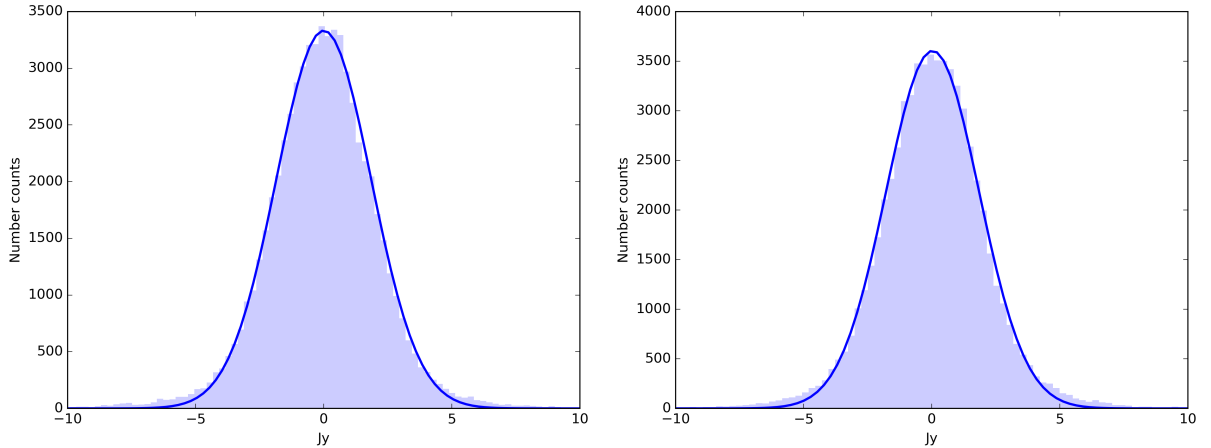


Figure 4.7: Distribution of the real part of the residual visibilities at 150 MHz (left) and 160 MHz (right) for baselines greater than 30 m (see text for details). The blue line is the Gaussian profile fitted to the distribution.

### 4.2.1 Absolute flux calibration

The initial bandpass calibration did not tie the visibility amplitude to an absolute flux scale. We used Pictor A to set the absolute flux density scale according to the [Jacobs et al. \(2013\)](#) model:

$$S(\nu) = S_0 \left( \frac{\nu}{\nu_0} \right)^{\alpha_0} \quad (4.1)$$

where  $S(\nu)$  is the predicted flux density,  $S_0 = 382$  Jy is the source flux density at  $\nu_0 = 150$  MHz, and  $\alpha_0 = -0.76$  is the spectral index. If  $a(\hat{\mathbf{r}}, \nu)$  describes the telescope primary beam response evaluated at frequency  $\nu$  and in the direction of Pictor A, then we can write the scaling factor  $s(\nu)$  for each day as

$$s(\nu) = \frac{S(\nu)a(\hat{\mathbf{r}}, \nu)}{S_m(\nu)}. \quad (4.2)$$

where  $S_m(\nu)$  is the measured spectrum. For each of the linear orthogonal polarizations xx and yy, the primary beam response  $a(\hat{\mathbf{r}}, \nu)$  is defined as

$$a(\hat{\mathbf{r}}, \nu) = j(\hat{\mathbf{r}}, \nu)j^*(\hat{\mathbf{r}}, \nu) \quad (4.3)$$

where  $j(\hat{\mathbf{r}}, \nu)$  defines the multiple propagation effects along the signal path (Smirnov, 2011a).

The visibility  $v(\mathbf{b}, \nu)$  is scaled such that the absolutely calibrated visibility can be represented as

$$v^a(\mathbf{b}, \nu) = s(\nu)v(\mathbf{b}, \nu). \quad (4.4)$$

We then derived Pictor A spectrum  $S_m$  for each of the 40 days of observation in order to test the accuracy of the absolute calibration. Following processes were carried out for each polarization (x and y) per day:

1. calibrated visibilities were rotated in the direction of Pictor A;
2. a  $2^\circ \times 2^\circ$  image was made for each frequency channel including only baselines greater than  $12\lambda$ . The three-dimensional Fourier transform in widefield imaging was accounted for by using the w-stacking algorithm implemented in WSclean (Offringa et al., 2014). Uniform weights were used and the snapshot image was deconvolved down to a flux threshold of 20 Jy through the Cotton-Schwab algorithm;
3. the source peak value was extracted from each image;
4. residual visibilities were formed by subtracting Pictor A from the calibrated visibilities, which were rotated in the direction of Pictor A.  $2^\circ \times 2^\circ$  images were generated from the residual visibilities for each frequency channel including only baselines greater than  $12\lambda$ . Same imaging specifications as in step 2 was used. The rms values evaluated from the resulting residual images provide uncertainties associated with the extracted flux density values.

We eventually average the spectra over 40 days of observation. The rms difference between the model and our average spectrum  $\tilde{S}_m(\nu)$  yielded a 7.7 Jy rms, which is slightly greater than the

5.5 Jy uncertainty on the model spectrum (Jacobs et al., 2013). We therefore applied a further correction to the absolute calibration in the form of a polynomial fit. A fifth order polynomial was fitted to the ratio  $r(\nu)$ :

$$r(\nu) = \frac{S(\nu)a(\hat{\mathbf{r}}, \nu)}{S_m(\nu)}. \quad (4.5)$$

The 3.5 Jy rms obtained after a fifth order polynomial fit is now smaller than uncertainty on the model spectrum.

The absolutely calibrated visibilities are thus given by

$$v^c(\mathbf{b}, \nu) = \tilde{r}(\nu)v^a(\mathbf{b}, \nu) \quad (4.6)$$

where the fitted ratio  $\tilde{r}(\nu)$  is equal to

$$\tilde{r}(\nu) = \sum_{i=0}^{n=5} r_i \nu^i \quad (4.7)$$

with  $r_i$  representing the coefficients of the polynomial fit.

The average spectrum  $\tilde{S}_m(\nu)$  of Pictor A is again derived from  $v_c(\mathbf{b}, \nu)$  in a similar fashion by repeating steps (1) to (4). The top panel of Figure 4.8 shows  $\tilde{S}_m(\nu)$  for xx and yy polarizations and the bottom panel displays the associated percentage error  $e(\nu)$ :

$$e(\nu) = \frac{|S(\nu) - \tilde{S}_m(\nu)|}{S(\nu)} \times 100. \quad (4.8)$$

The variations in the spectrum (Figure 4.8) are significantly larger than the errors for some frequencies, they may be due to calibration limitations of our model and this will subject of future investigation. As the gain solutions do not vary significantly over consecutive days, it is fair to assume that these variations are more contained within 24 hours. Hence, the derived calibration solutions for each day were applied to all the observations carried out that particular day.

Crossed polarized visibilities for each antenna pair  $\{i, j\}$  were calibrated as follows:

$$\begin{aligned} v_{xy\{i,j\}}^c(\mathbf{b}, \nu) &= (g_{\{i\}x}(\nu)g_{\{j\}y}^*(\nu))^{-1} v_{xy\{i,j\}}^m(\mathbf{b}, \nu) \\ v_{yx\{i,j\}}^c(\mathbf{b}, \nu) &= (g_{\{i\}y}(\nu)g_{\{j\}x}^*(\nu))^{-1} v_{yx\{i,j\}}^m(\mathbf{b}, \nu) \end{aligned} \quad (4.9)$$

where  $v_{xy}^m$  and  $v_{yx}^m$  are the measured crossed polarized correlator outputs,  $g_x$  and  $g_y$  are the gain solutions for x and y polarizations respectively. The gain solutions in equation 4.9 include the scaling factors from equations 4.2 and 4.7.

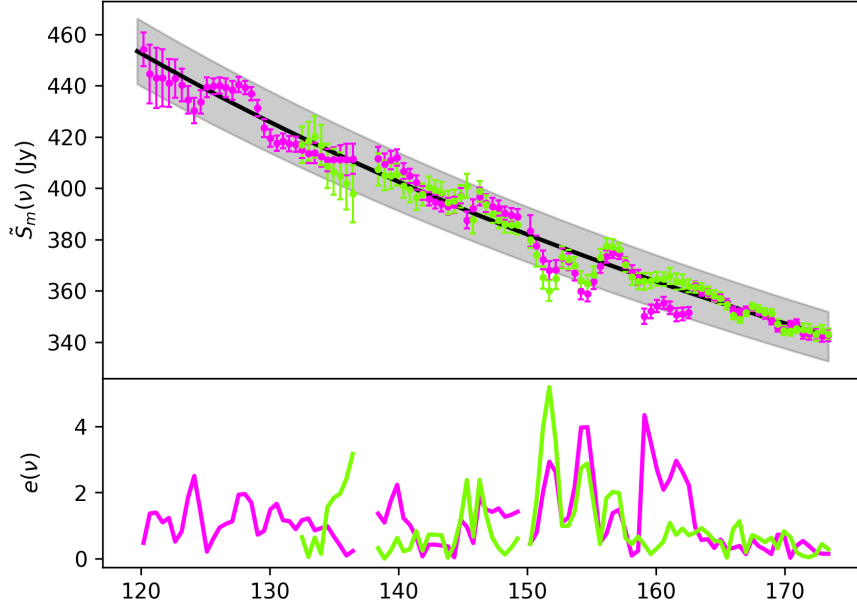


Figure 4.8: *Top panel:* Spectrum of Pictor A averaged over 40 days of observations for xx (magenta) and yy (green) polarizations. The black line represents the model spectrum (Jacobs et al., 2013) and the shaded region its  $2\sigma$  uncertainty. *Bottom panel:* Relative error.

We then formed images with uniform weighting using the  $w$ -projection algorithm from the individual snapshots. Each image was obtained from multi-frequency synthesis (Conway & Sault, 1995) between 120 and 175 MHz and deconvolved down to a flux density of 10 Jy. The resulting images exhibited “whiskers” like structures around the brightest sources (left panel; Figure 4.9) and, they were first believed to arise due to undeconvolved sidelobes. Nevertheless, we did not observe any whiskers associated with the faint sources (or they might be below the noise level). Hence, we subtracted the brightest sources with which they appeared to be associated. The sources were modeled using the CLEAN components obtained through deconvolution and subtracted from the calibrated visibilities. The whiskers did not fade even after the bright source subtraction. They might be due to ionospheric distortions that cause phase errors in time scales shorter than 10 minutes and this will be investigated in the future. Furthermore, they are different

for two sources, artefacts near Fornax A look like alternating positive and negative stripes (top left panel of Figure 4.9), and those associated with Taurus A are positive stripes  $\sim 30$  arcmins apart (bottom left panel of Figure 4.9). Bernardi et al. (2010) also found similar whiskers (see left panel of Figure 2.6) associated with the bright source 3C 196 and the cause is still a mystery to them as well. Despite the fact that we do not know the origin of these artefacts, we attempt to model and subtract them from the individual xx and yy snapshots. The area around the whiskers were masked and models were constructed using CLEAN components generated by the Cotton-Schwab algorithm. While the subtraction was effective in few of the snapshots (shown in right panels of Figure 4.9) it was not adequate to eliminate the whiskers from others.

An intriguing question now would be – do these structures have an impact on foreground avoidance. Although we do not attempt any power spectrum analysis in this chapter, we are interested in acquiring a first order approximation of the frequency behavior of these structures beyond the horizon. Therefore, we Fourier transformed the per-baseline visibilities before and after subtracting the whiskers along the frequency axis to construct delay spectra (Parsons et al., 2012). If  $\tilde{v}^c$  and  $\tilde{v}_w^c$  are the per baseline delay transformed visibilities before and after subtracting these structures respectively, the ratio  $r_w$  can be expressed as

$$r_w = \frac{(|\tilde{v}^c(\mathbf{b})| - |\tilde{v}_w^c(\mathbf{b})|)}{|\tilde{v}^c(\mathbf{b})|}. \quad (4.10)$$

The comparatively higher  $r_w$  values beyond the horizon (Figure 4.10) reveal scattering of power beyond the horizon. This may be disadvantageous to foreground avoidance, in particular, when using the delay transform technique (Parsons et al., 2012) as it attempts to separate spectrally smooth foregrounds from the data, without proper attention to the morphology. Further analysis is required to describe these structures in order to escape systematics that are not captured by the delay transform approach, however, this effort is beyond the scope of this work.

### 4.3 All-sky images

After calibration, we generated full polarization all-sky images. We used an “optimal map-making” approach (Morales & Matejtek, 2009; Ord et al., 2010). Given  $n$  individual measure-

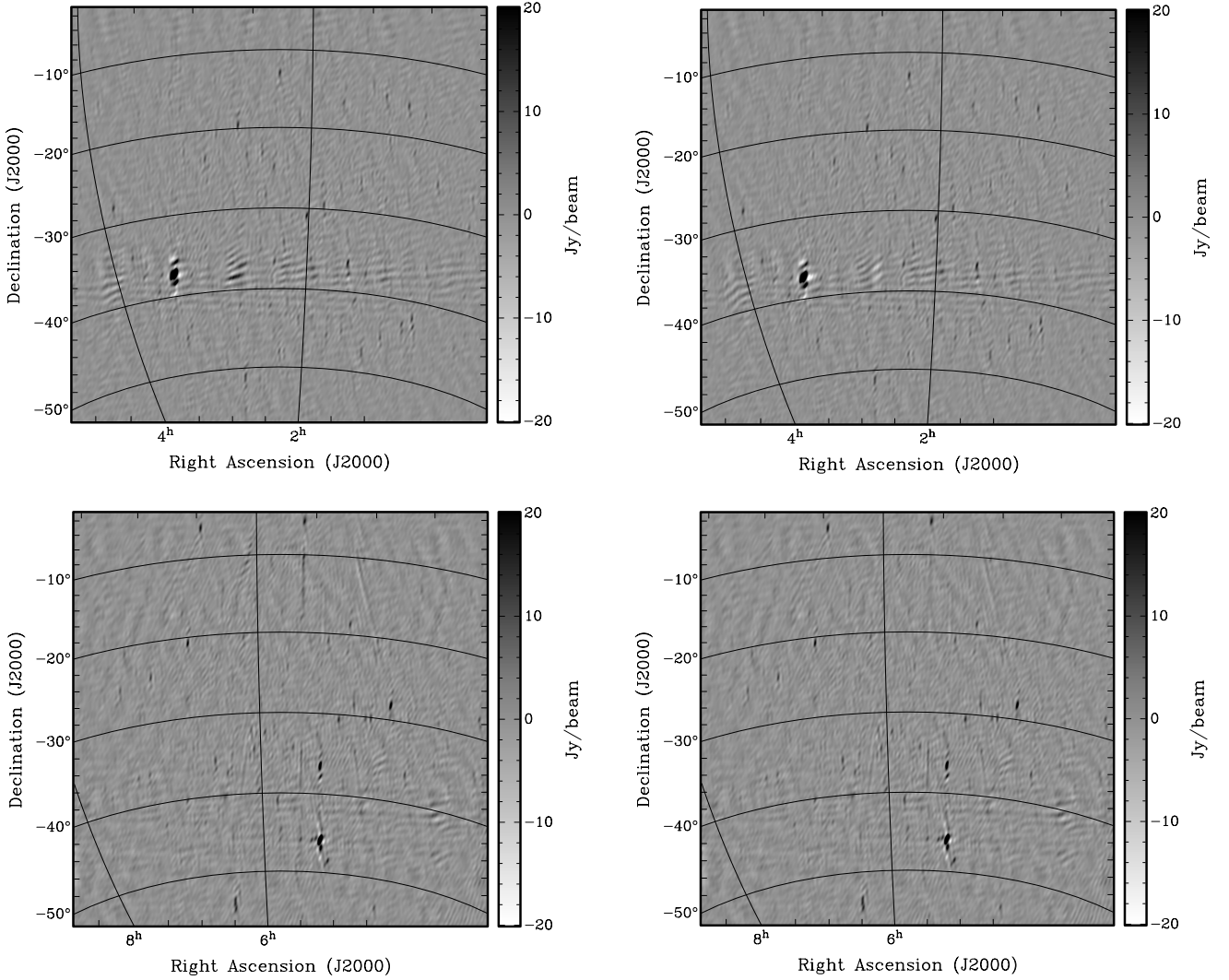


Figure 4.9: Examples of two 10 minute xx snapshot images before (left) and after (right) subtracting the whiskers from the visibilities (see text for description).

ments of the sky brightness  $\mathbf{s}'_i(\hat{\mathbf{r}}, \nu) = (I', Q', U', V')_i^T$ , the best estimate of the polarized sky brightness  $\tilde{\mathbf{s}}'(\hat{\mathbf{r}})$ , each with a different weight  $\mathbf{w}_i(\hat{\mathbf{r}}, \nu)$  can be constructed using

$$\tilde{\mathbf{s}}'(\hat{\mathbf{r}}, \nu) = \frac{\sum_{i=1}^n \mathbf{s}'_i(\hat{\mathbf{r}}, \nu) \circ \mathbf{w}_i(\hat{\mathbf{r}}, \nu)}{\sum_{i=1}^n \mathbf{w}_i(\hat{\mathbf{r}}, \nu) \circ \mathbf{w}_i(\hat{\mathbf{r}}, \nu)} \quad (4.11)$$

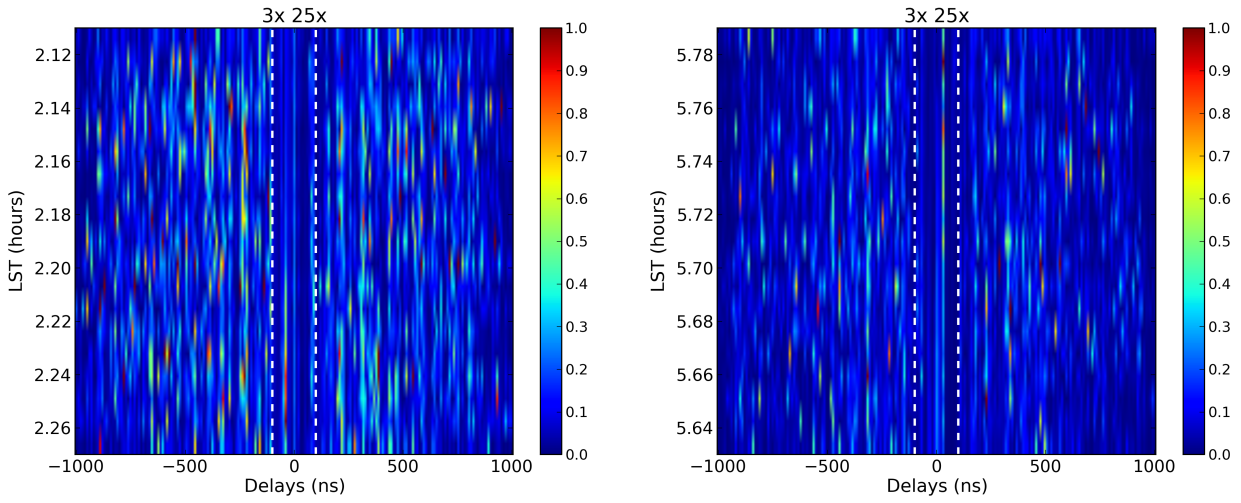


Figure 4.10: Ratios  $r_w$  obtained from the delay transformed visibilities of two snapshots at julian dates 2456617.36176 (left) and 2456617.50791 (right) using equation 4.10 for a 30 m east west baseline. The white dashed line denotes the horizon limit.

where  $\circ$  denotes the Hadamard product (applicable for multiplicative operations only). If the weights are taken to be the diagonal elements of the  $4 \times 4$  Mueller matrix used to describe the primary beam (chapter 3), equation 4.11 becomes

$$\tilde{s}'(\hat{r}, \nu) = \mathbf{D}^{-1} \left[ \sum_{i=1}^n s'_i(\hat{r}, \nu) \circ \text{diag}(\mathbf{A}_i(\hat{r}, \nu)) \right]. \quad (4.12)$$

where the normalization matrix  $\mathbf{D}$  can be written as follows:

$$\mathbf{D} = \sum_{i=1}^n [\text{diag}(\mathbf{A}_i(\hat{r}, \nu))] \circ [\text{diag}(\mathbf{A}_i(\hat{r}, \nu))]^* \quad (4.13)$$

We note that equation 4.12 applies optimal weights but neglecting the off diagonal terms of the primary beam matrix, it does not correct for leakage from any intrinsic Stokes parameters into any observed ones as it is done in Ord et al. (2010). At this stage of the analysis, we are interested in actually measuring the amount of leakage from total intensity in order to validate the primary beam models used in chapter 3. We therefore began by creating pseudo Stokes visibilities  $v^c = (v_I^c, v_Q^c, v_U^c, v_V^c)^T$  (in an analogical fashion to what is done in the power spectrum

analysis of PAPER in [Ali et al. \(2015\)](#)):

$$\begin{aligned} v_I^c &= 0.5(v_{xx}^c + v_{yy}^c); & v_Q^c &= 0.5(v_{xx}^c - v_{yy}^c) \\ v_U^c &= 0.5(v_{xy}^c + v_{yx}^c); & v_V^c &= 0.5i(v_{xy}^c - v_{yx}^c) \end{aligned} \quad (4.14)$$

where  $(v_{xx}^c, v_{xy}^c, v_{yx}^c, v_{yy}^c)^T$  is the four polarization correlator output defined in equation 3.3. In order for the visibilities to be added coherently, they were phased to a common right ascension. Individual  $36^\circ \times 36^\circ$  snapshot images were generated from the phased Stokes visibilities with uniform weighting. The multi-frequency synthesis algorithm ([Conway & Sault, 1995](#)) was used in order to provide a better  $uv$  coverage by taking advantage of the wide bandwidth. Stokes  $I$  snapshots were deconvolved down to a flux density threshold of 10 Jy. The snapshot images were then averaged together (equation 4.12) to produce the final images. Each final image included all the snapshots that were 1.2 hours before and after transit.

Our total intensity images (Figures 4.11, 4.12, 4.13) do not show bright diffuse Galactic emission similar to the structures observed by, for example, [Bernardi et al. \(2009\)](#), [Offringa et al. \(2016\)](#) and [Beardsley et al. \(2016\)](#). As we filter the shorter baselines where the diffuse emission is brighter, we do not observe diffuse emission in our total intensity images. Another plausible cause may be the combination of our limited  $uv$  coverage as well as the choice of weighting that significantly downweights short baselines. Emission is, therefore, mostly in the form of compact sources apart from Fornax A (bottom panel, Figure 4.11) and the Vela-Puppis complex (Figure 4.13). Pictor A (top panel, Figure 4.12) and the Crab Nebula (Figure 4.13) are the dominant compact sources.

The Stokes  $Q$  images are dominated by the leakage from unpolarized point sources (see top panels; Figure 4.14, 4.15 and 4.16 are examples). We proceeded by subtracting the instrumentally polarized sources from the phased visibilities and combining the snapshots using equation 4.12 in order to characterize the observed polarized sky in terms of Stokes  $Q$ . We modeled the polarized sources using CLEAN components by deconvolving the Stokes  $Q$  snapshots down to a flux density equivalent to 0.01 of the image peak, and subtracted them from the visibilities. The sources are fairly well subtracted (bottom panels; Figures 4.14, 4.15, and 4.16), for instance, the peak around Fornax A of about 3 Jy dropped to a rms noise of 0.4 Jy. The images now look

relatively featureless. The residuals are approximately of the same order as Figure 3.1. We leave the validation of our beam model using these observations for future work.

In the final preparation of this thesis, we corrected a mistake that initially gave high power in Stokes  $U$  and  $V$  images. Figures 4.17 and 4.18 now present the corrected images. We still present the RM synthesis carried out with Stokes  $Q$  only, we will leave the analysis including Stokes  $U$  for future work. The rms value in the resulting Stokes  $U$  (Figure 4.17) image is of the same order as that of Stokes  $Q$  (Figure 4.14) image and the rms value in Stokes  $V$  (Figure 4.18) image is half that of Stokes  $Q$  image (Figure 4.14). Moreover, Stokes  $U$  and  $V$  do not show any particular feature of leakage from the unpolarized sources as compared to Stokes  $Q$  in which instrumentally polarized sources follow morphologies similar to Stokes  $I$ . However, we attempted to subtract conservative models of the instrumentally polarized sources from Stokes  $U$  and  $V$  visibilities. Most of the distorted patterns, for example, around Fornax A (top panel, Figure 4.17 and Figure 4.18) disappeared after the subtraction. Note that we do not use Stokes  $U$  in the following analysis.

We measured the instrumental polarization as follows:

1. derived a Stokes  $I$  source catalogue (refer to §4.4.1 for details);
2. for each Stokes  $I$  source, searched for a corresponding peak greater than 5 times the rms noise. If no peak was found, we considered 5 times the rms noise to be the upper limit to the instrumental polarization associated with the source. The noise was evaluated as the rms of the pixel distribution taken within a 5 arcmins radius centered at the source.
3. divided both the extracted peaks and the upper limits by the corresponding Stokes  $I$  peaks.

The ratios are plotted in Figure 4.19.

The measurements were then averaged resulting in an instrumental polarization  $\langle \gamma_{\text{ins}} \rangle = 2.7\%$ . Given that upper limits were not included, this average can be considered as a conservative estimate of the instrumental polarization.

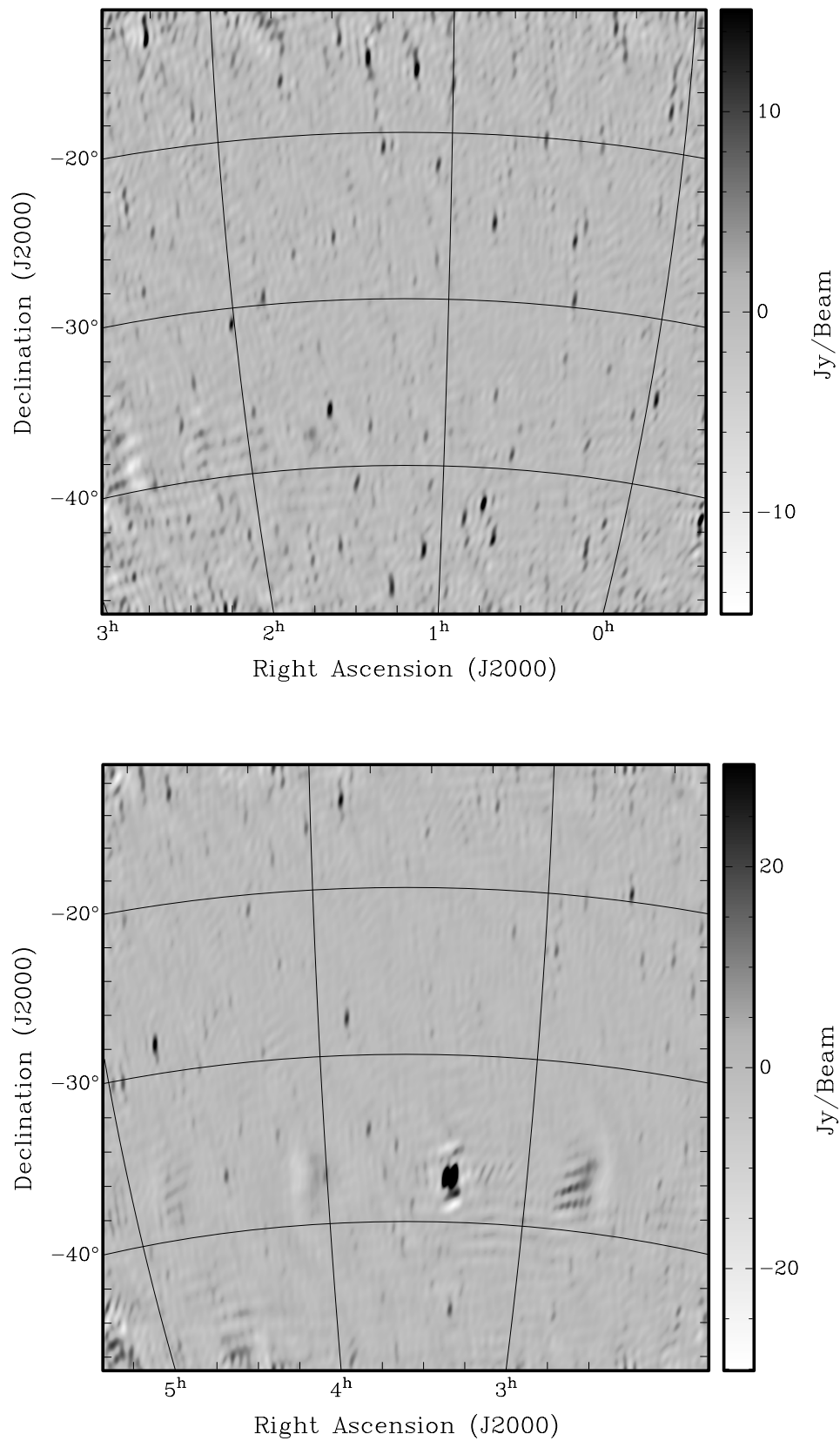


Figure 4.11: Stokes  $I$  maps generated including 40 days of observations with phase centers at LST = 1.2 hours (top) and 3 hours (bottom) respectively.

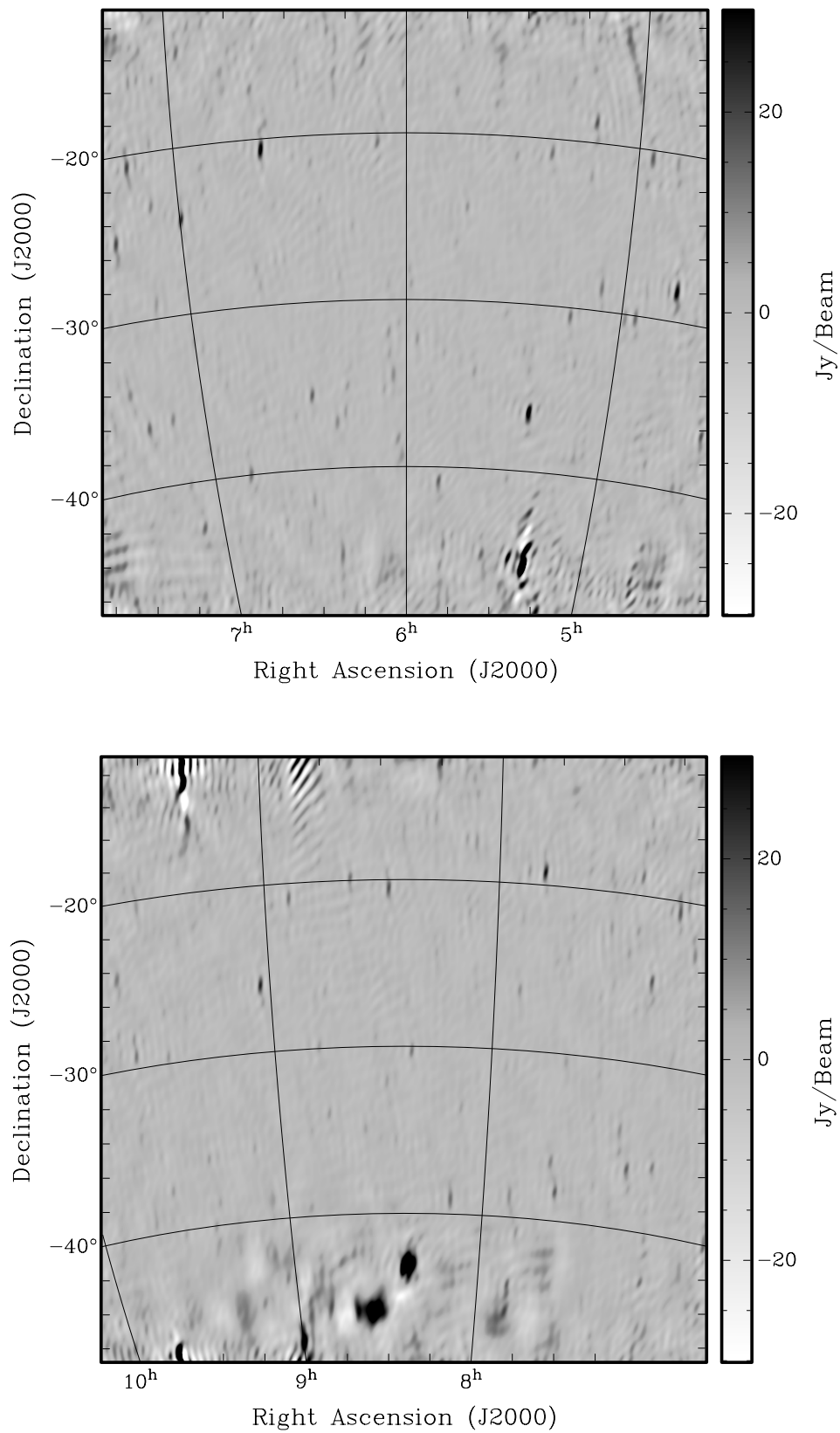


Figure 4.12: Same as Figure 4.11 but with phase centers at LST = 6.0 hours (top) and 8.4 hours (bottom) respectively.

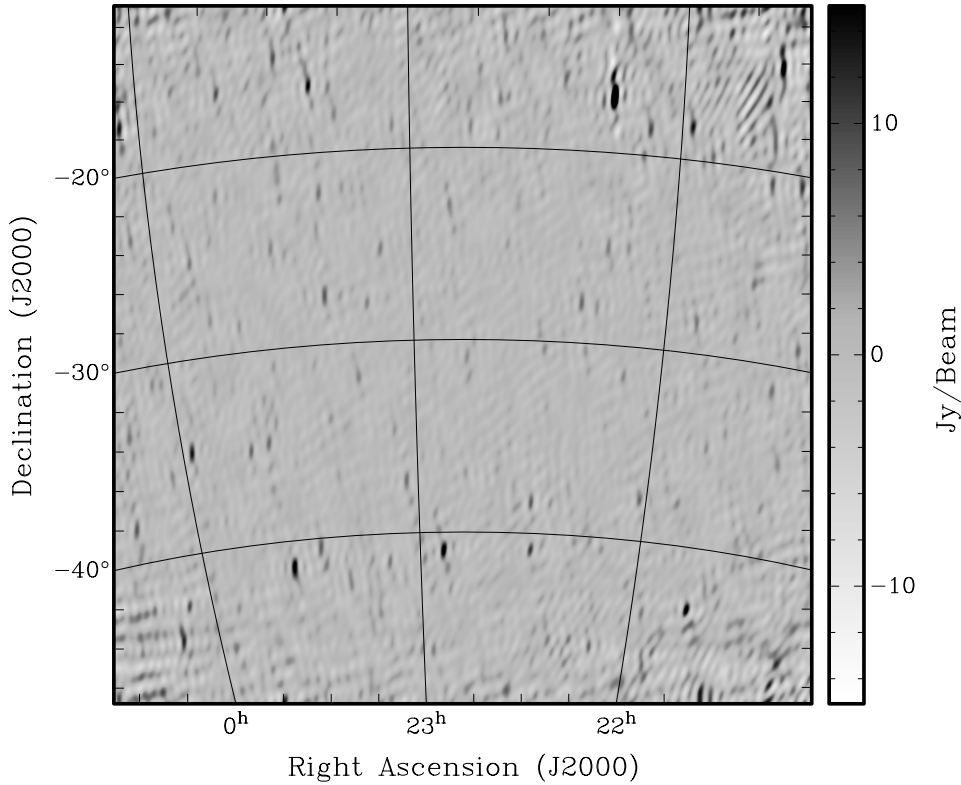


Figure 4.13: Same as Figure 4.11 but with phase center at LST = 22.8 hours.

### 4.3.1 Rotation Measure synthesis

Rotation Measure (RM) synthesis (Brentjens & de Bruyn, 2005) is a powerful tool to measure polarized emission, in particular, to recover weak polarized emission as a function of Faraday depth  $\phi$ . It utilizes the Fourier relationship between the polarized emission  $P(\lambda^2)$  and the Faraday depth distribution  $F(\phi)$

$$P(\lambda^2) = W(\lambda^2) \int_{-\infty}^{\infty} F(\phi) e^{-2i\phi\lambda^2} d\phi \quad (4.15)$$

where  $W(\lambda^2)$  is the weighting function and  $\lambda$  is the observing wavelength.

We used RM synthesis in this work to characterize polarized emissions from our observations as this technique successfully revealed widespread, weak polarized emission around the Perseus cluster (de Bruyn & Brentjens, 2005). In addition, it can be performed only on Stokes  $Q$  or  $U$ , though we lose information about the sign of the Faraday depth (Brentjens & de Bruyn, 2005).

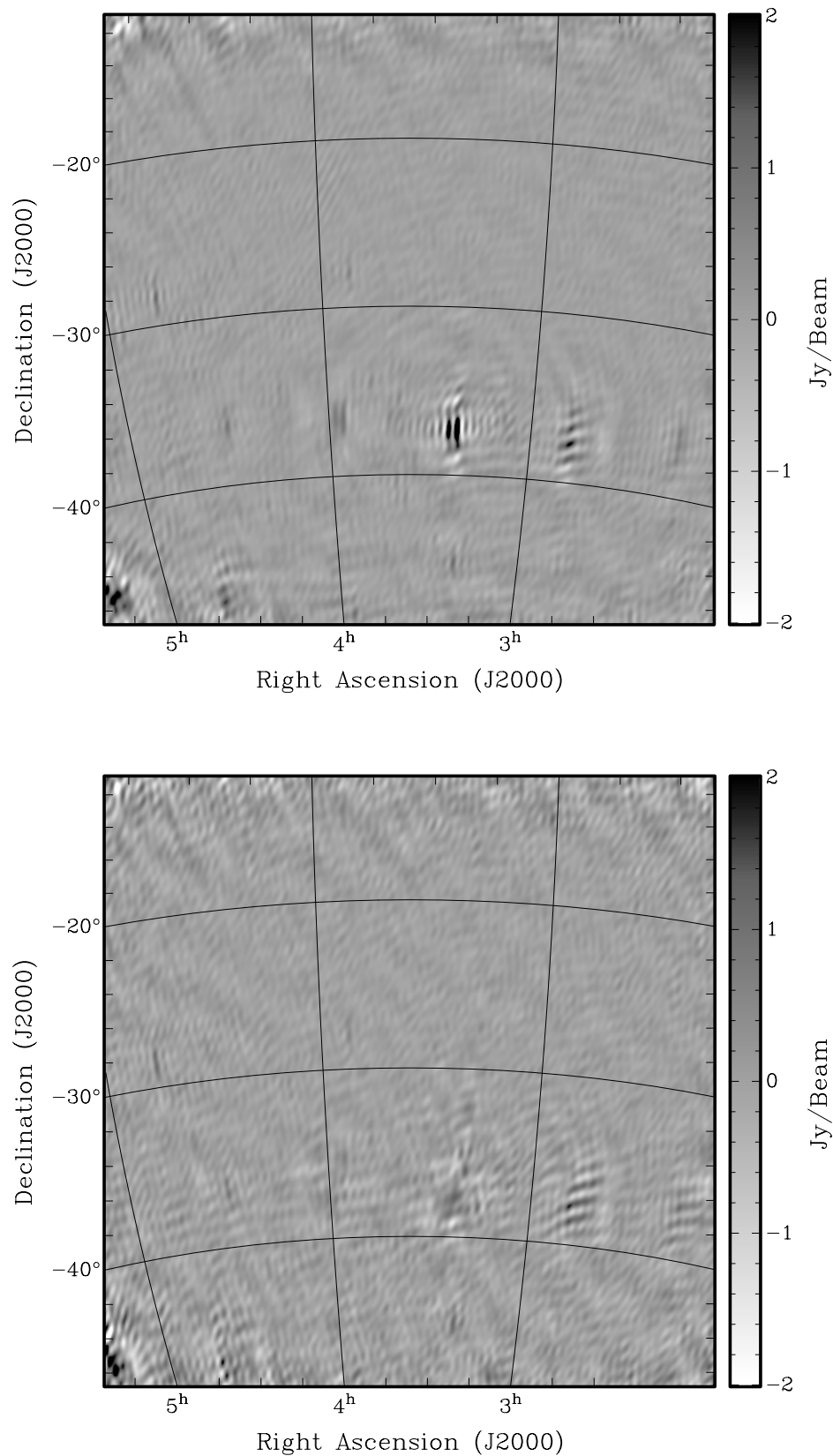


Figure 4.14: Stokes  $Q$  map generated including 40 days of observations with phase center at LST = 3 hours with before (top) and after (bottom) subtracting instrumental polarization from Fornax A.

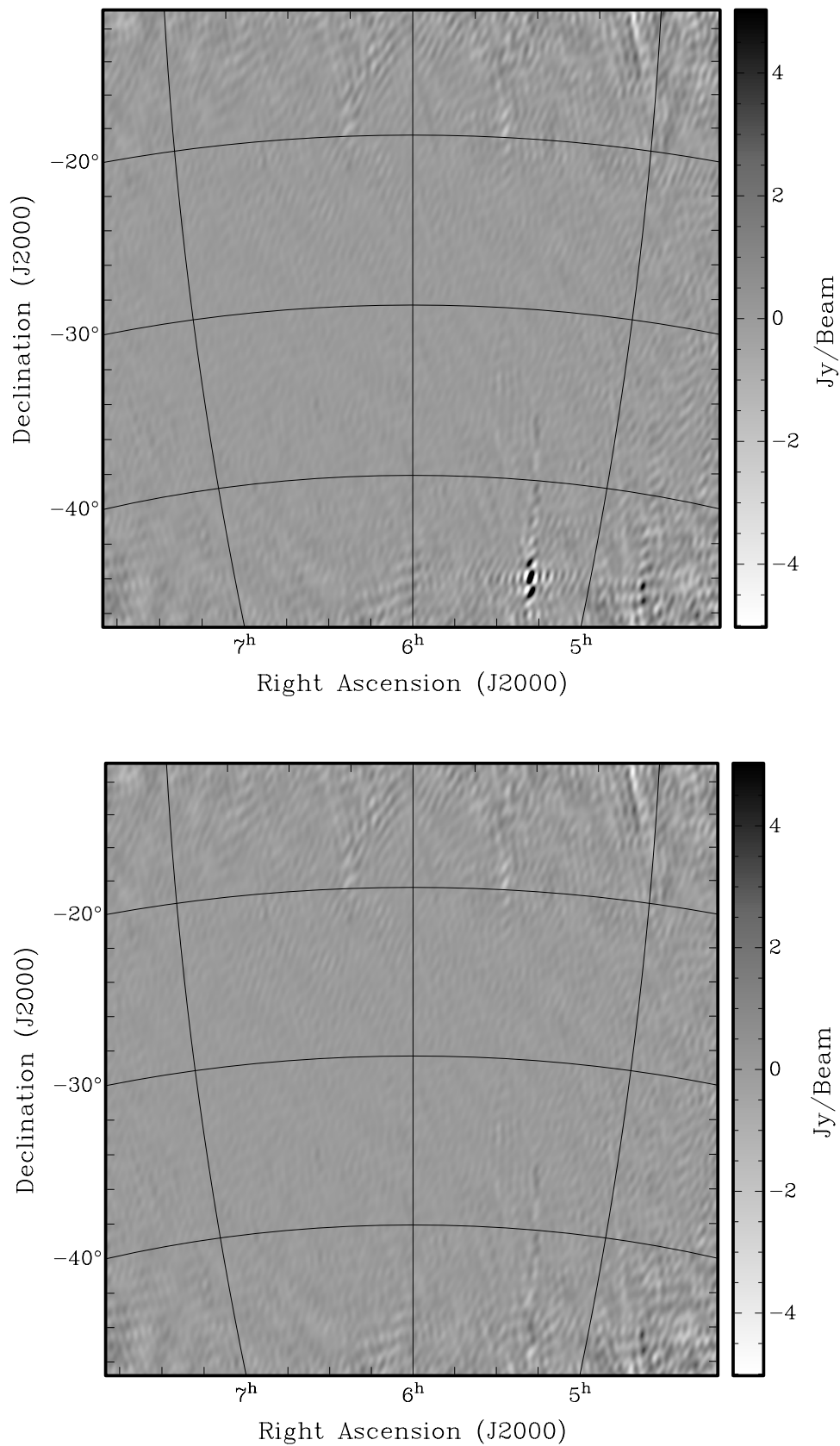


Figure 4.15: Stokes  $Q$  map generated including 40 days of observations with phase center at LST = 6 hours with before (top) and after (bottom) subtracting instrumental polarization from Pictor A.

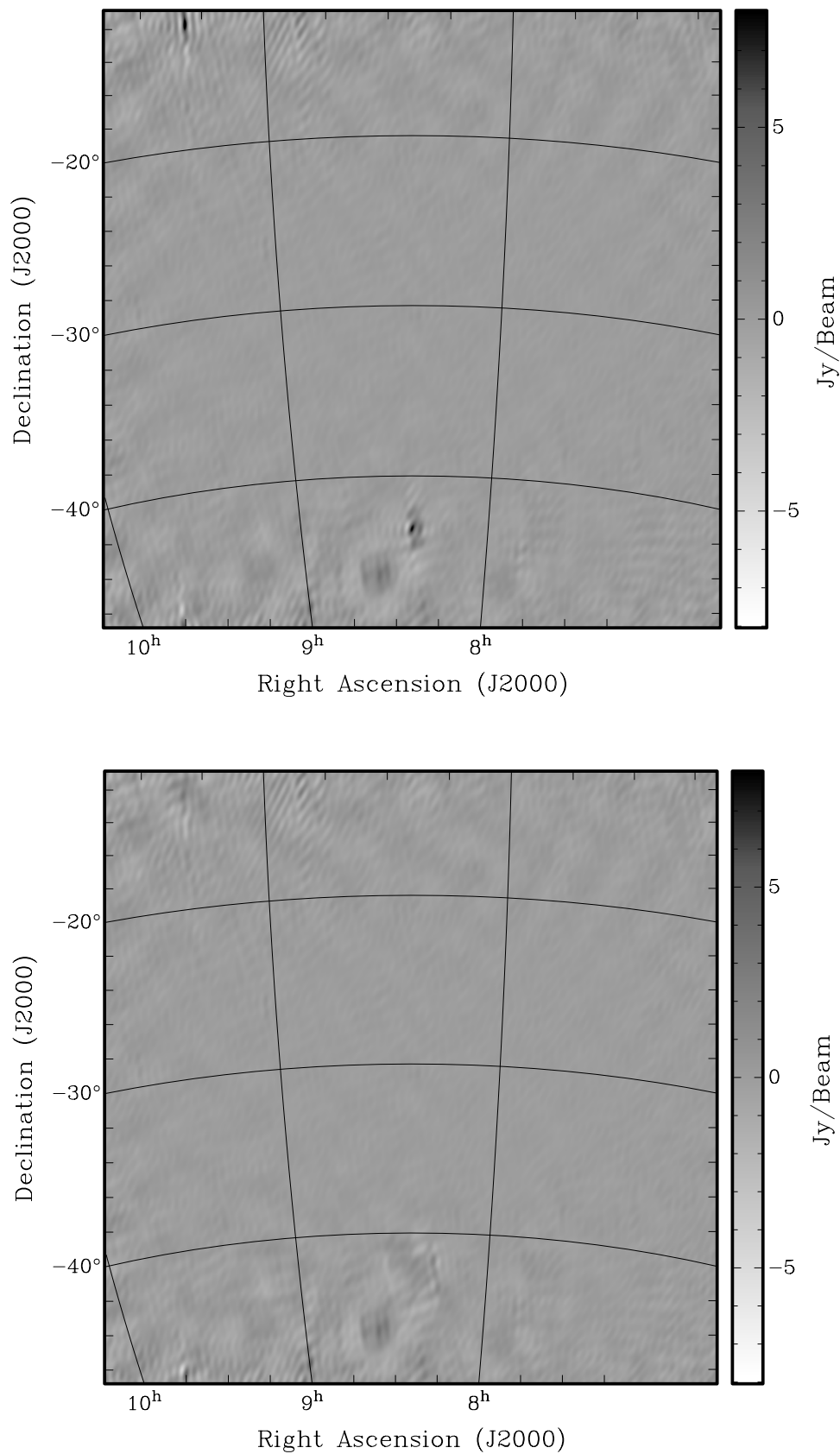


Figure 4.16: Stokes  $Q$  map generated including 40 days of observations with phase center at LST = 8.4 hours with before (top) and after (bottom) subtracting instrumental polarization from Puppis A and the Crab Nebula.

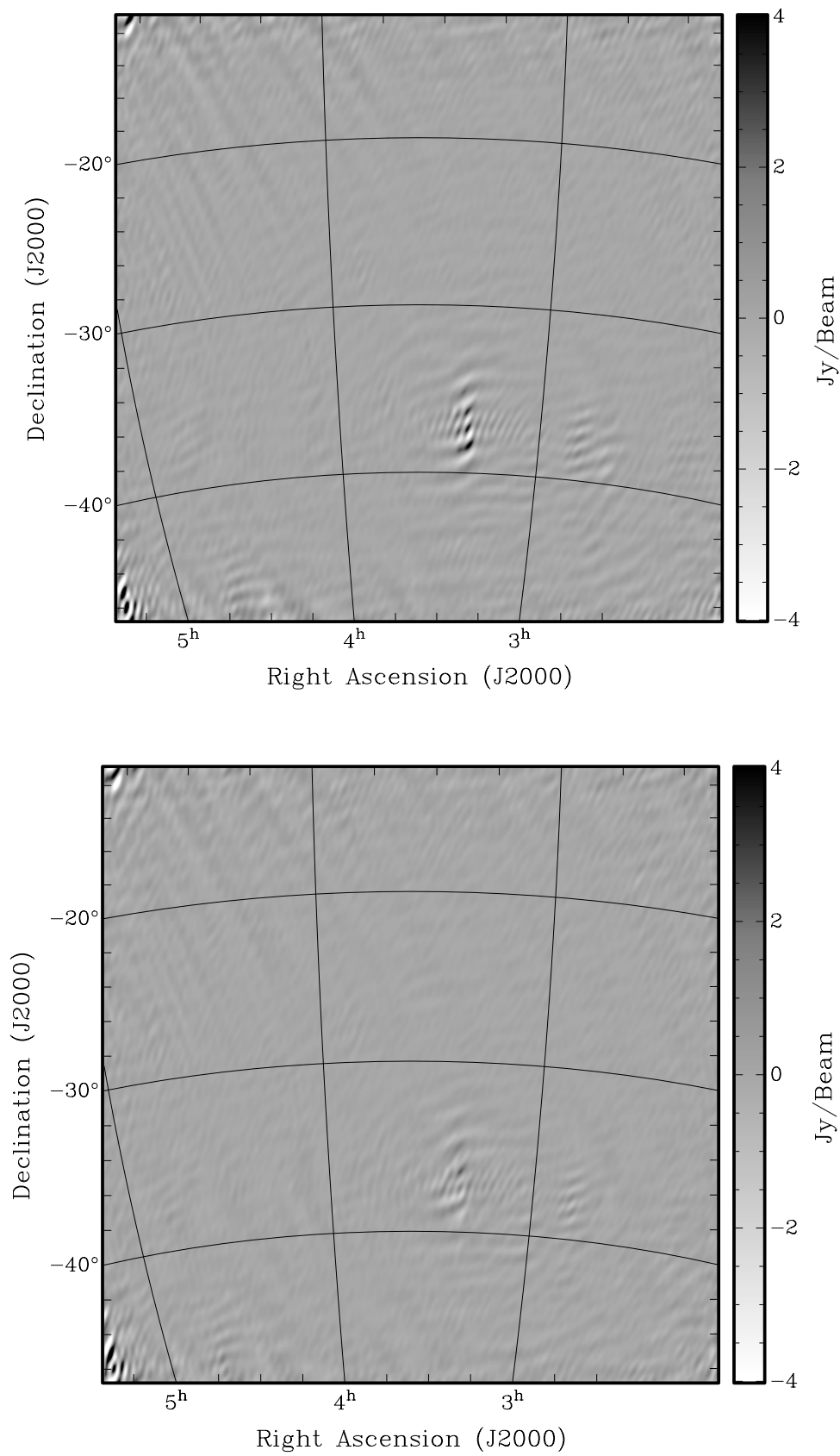


Figure 4.17: Stokes  $U$  map generated including 40 days of observations with phase center at LST = 3 hours (top) and after subtracting instrumental polarization from Fornax A (bottom)

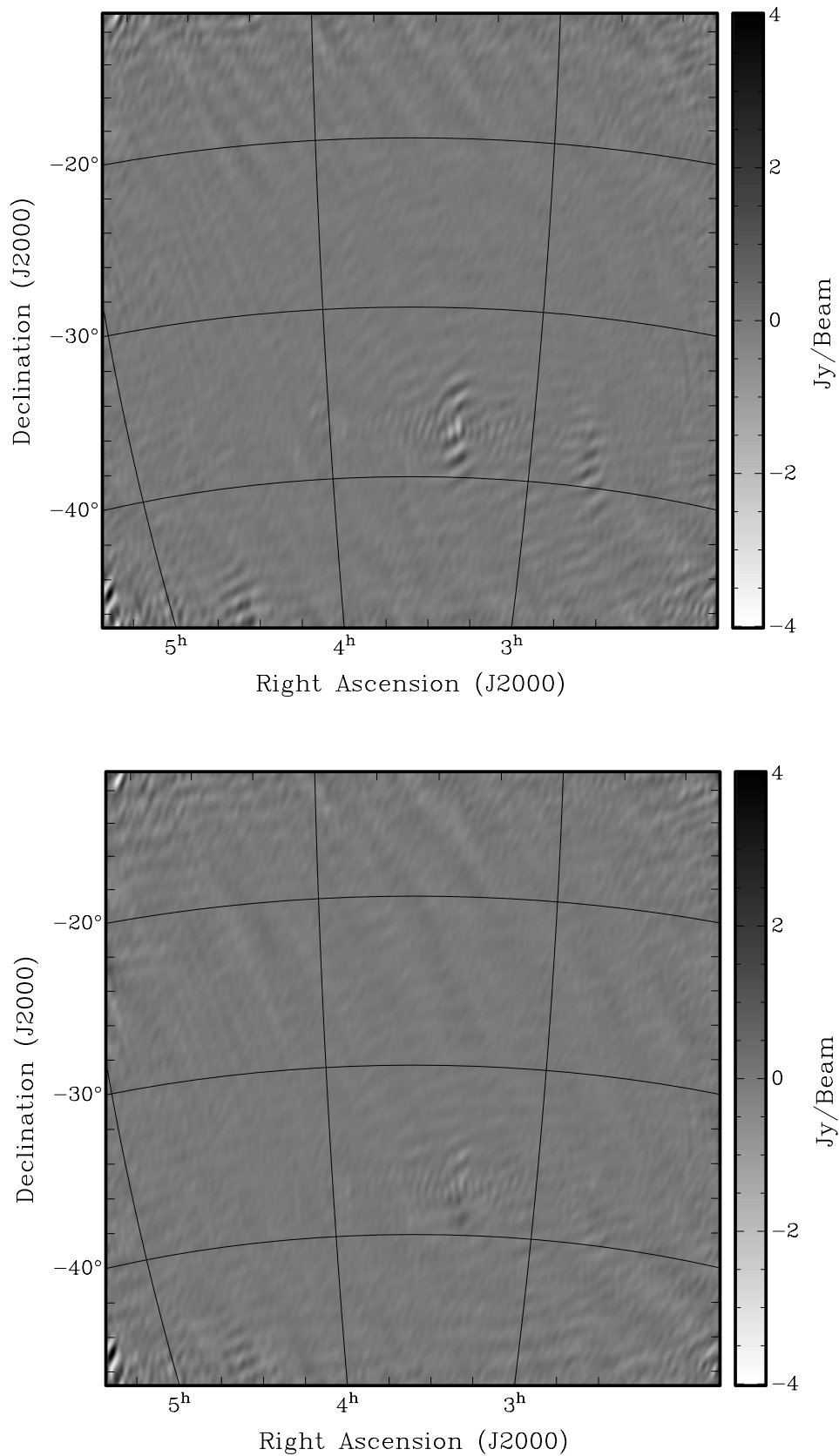


Figure 4.18: Stokes  $V$  map generated including 40 days of observations with phase center at LST = 3 hours (top) and after subtracting instrumental polarization from Fornax A (bottom)

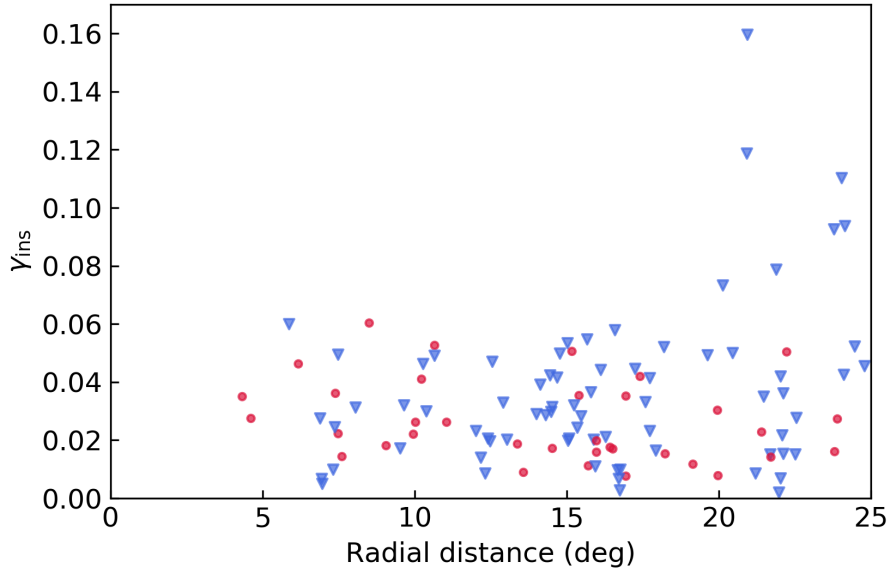


Figure 4.19: Instrumental polarization fraction  $\gamma_{ins}$  as a function of radial distance of the source from the phase center. Sources brighter than 5 Jy in Stokes  $I$  were included. Detections are denoted by the red dots and upper limits by the blue triangles.

The output of RM synthesis is a cube at selected values of Faraday depth. The resolution in Faraday depth is determined by the RM Spread Function (RMSF), which is the Fourier transform of  $W(\lambda^2)$ . We obtained a RMSF width of  $1.7 \text{ rad m}^{-2}$  from our frequency coverage. The sensitivity to the maximum RM, set by the channel width over which the visibilities are averaged, is  $155 \text{ rad m}^{-2}$ . We restricted the input to RM synthesis to Stokes  $Q$  only.

Given we have Stokes  $Q$  maps phased at five different LSTs, we obtained 5  $\phi$ -cubes as outputs. We do not observe significant Faraday structures across Faraday depths, similar to the features in (Bernardi et al., 2009; Jelić et al., 2015; Lenc et al., 2016). The level of polarized emission is much fainter at higher  $\phi$  values, as expected, as emission at high  $\phi$  values suffers from bandwidth depolarization (Bernardi et al., 2013; Jelić et al., 2015). The noise varies between 50–100 mJy across LSTs. Figure 4.20 shows two slices of the Faraday cubes across three LSTs:

- *top panel*: slices are relatively featureless, and do not depict any sky emission. The noise seems relatively higher at the edges;

- *middle panel*: the slice at the low  $\phi$  value is clearly dominated by Fornax A and its lobes;
- *bottom panel*: as we have few data points between  $0 < \text{LST} < 22$  hours, the slices have higher noise. The bright emission at the edges may be due to sidelobes from the Galactic center.

## 4.4 Results

We used measurements of the polarized emission to constrain the polarization models used in chapter 3 and, thus, estimated the expected polarization leakage into the EoR power spectrum.

### 4.4.1 Source Catalogue

We used the Python Blob Detection and Source Measurement (PyBDSM, [Mohan & Rafferty, 2015](#)) as our source finder to extract sources from the total intensity maps shown in Figures 4.11, 4.12, 4.13. The source finder identified source candidates in islands of pixels brighter than  $3\sigma$  (see Figure 4.21). A 2D Gaussian is then fitted to each island. As a result, PyBDSM found 88 possible source candidates from the search parameters we defined. The noise estimated by PyBDSM varies up to  $\sim 50\%$  from the Stokes  $I$  maps across different LSTs (Figure 4.22).

The catalogue of 88 unique sources were then compared with the Parkes–MIT–NRAO catalogue (PMN, [Wright & Otrupcek, 1990](#)). The reason for choosing the PMN catalogue is because it covers the sky from declination greater than  $+27^\circ$ . PAPER sources were matched with their PMN counterparts within a tolerance of 15 arcmins, and the closest one was chosen. We found that 30% of the sources do not match, which is unexpected. Future work will be done to improve source matching and cataloging. The catalogue of matched sources together with the unmatched sources, down to a minimum flux density of 5 Jy is listed in Table 4.2. The catalogue does not include Pictor A, Fornax A, the Crab Nebulae and Vela-Puppis. The format of the catalogue is as follows:

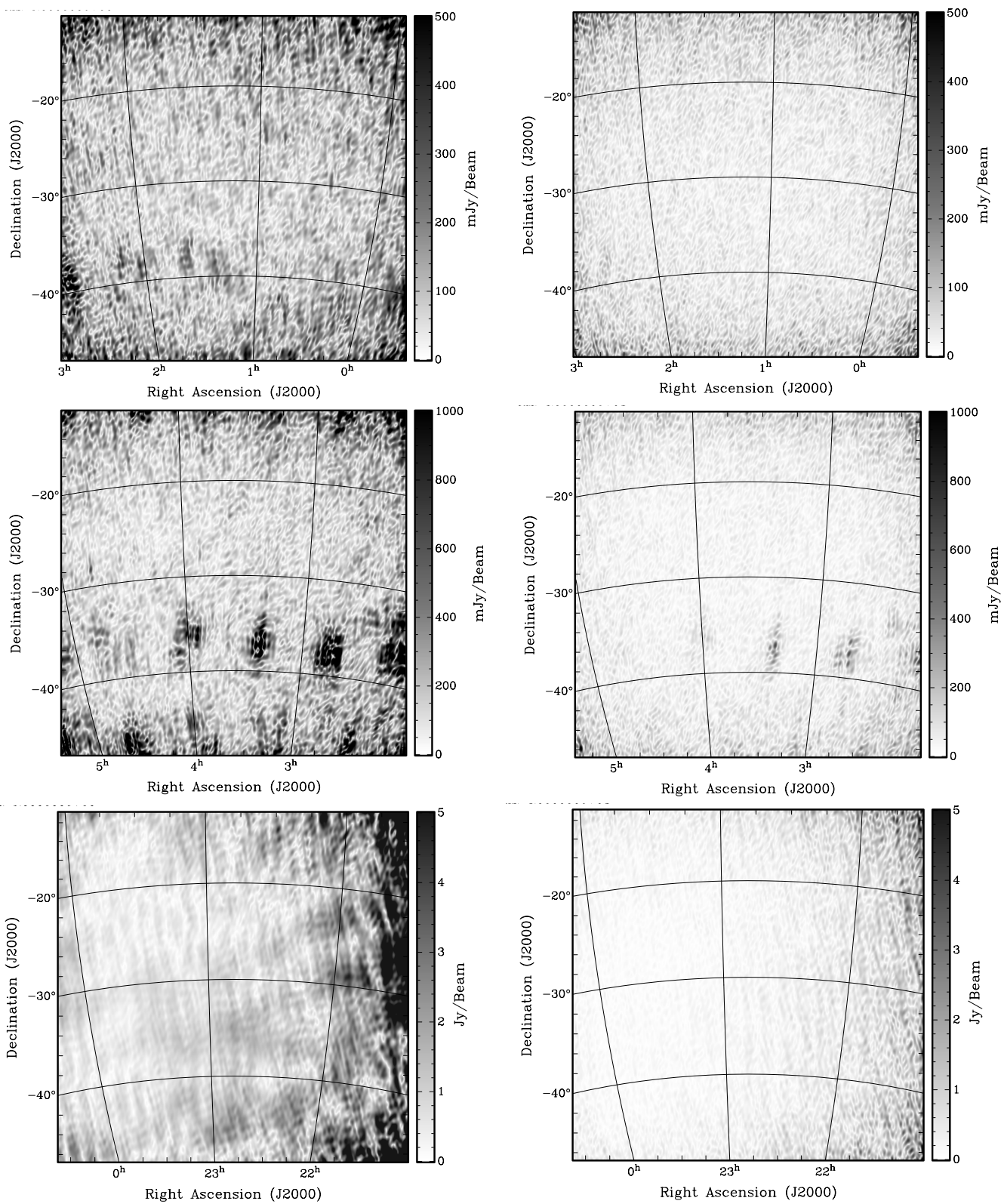


Figure 4.20: Polarized emission at Faraday depths 5 (left) and 40 ( $\text{rad m}^{-2}$ ) generated from averaged maps phased at LST 1.2 (top), 3.6 (middle) and 22.8 hours (bottom).

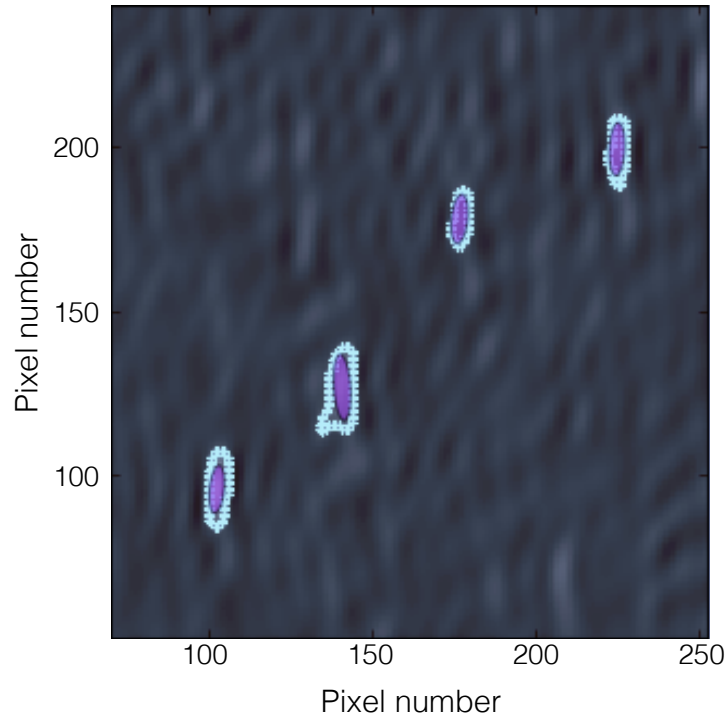


Figure 4.21: PyBDSM identifying potential source candidates in one of the final Stokes  $I$  maps. The axes are labeled in pixel numbers. The island boundaries that are identified are marked in cyan. The pink areas shows the pixels used in the Gaussian fit.

- Column 1: Source name <sup>2</sup>
- Column 2: Right ascension (J2000)
- Column 3: Declination (J2000)
- Column 4: Flux density (Jy) at 146.5 MHz

#### 4.4.2 Point source polarization analysis

Our  $\phi$  cubes did not reveal any polarized point source unlike [Bernardi et al. \(2013\)](#); [Lenc et al. \(2017\)](#) across LSTs (see Figure 4.23). Therefore, we used our measured polarized emission to

<sup>2</sup>Source names are taken from the PMN catalogue. Sources which fail to find an association with the PMN sources are named using the same convention as [Jacobs et al. \(2013\)](#).

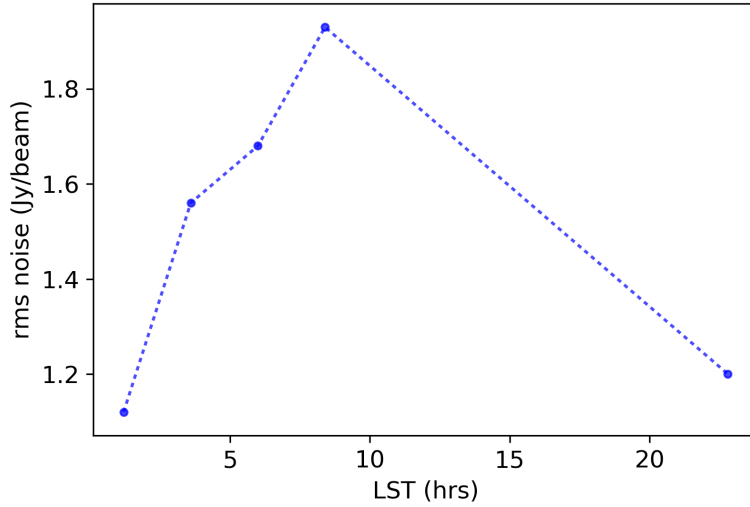


Figure 4.22: Rms noise calculated by PyBDSM for each Stokes map as a function of LST.

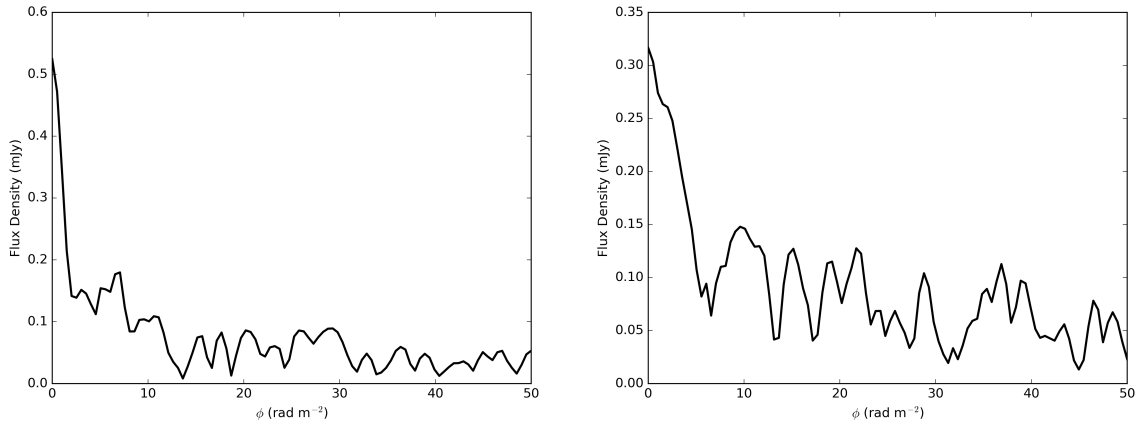


Figure 4.23: Slices through the  $\phi$  cubes at two of the polarized sources namely PMN J0351-2744 (left) and PKS J0636-2036 (right) detected by [Lenc et al. \(2017\)](#) at RM 34 and 50 rad m<sup>-2</sup>.

place constraints on the polarization model (see §3.3.2). We compared our Stokes  $I$  catalogue (Table 4.2) to [Taylor et al. \(2009\)](#) polarization catalogue, one of the most comprehensive polarization catalogue at 1.4 GHz to date within 15 arcmins. Out of 88 PAPER sources, 60 sources found their counterparts. Each of the 60 matched [Taylor et al. \(2009\)](#) sources were then compared with its neighboring sources within half synthesized beam, and the brightest ones were chosen

as they are more likely to be observed by PAPER. We then performed the following processes on each of the matched PAPER source:

1. selected a “cylindrical patch” formed by a circle of 5 arcmins centered around the source including three  $\phi$  values closest to the source;
2. evaluated the noise as the rms pixel distribution of the selected cylindrical patch. As no polarized source was detected, a conservative upper limit to the polarized flux density was taken to be five times the rms noise;
3. divided the upper limit by the corresponding Stokes  $I$  peak to obtain the observed polarization fraction.

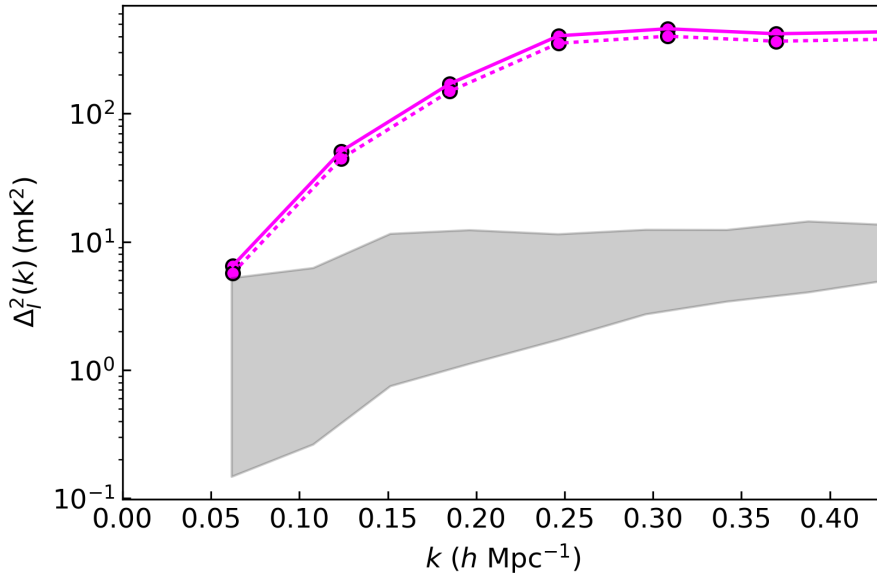


Figure 4.24: The solid line represents  $\Delta_I^2$ , the predicted leakage to the total intensity, estimated in chapter 3. The dashed line show the leakage when we assumed the polarization fraction to be distributed between 0 and 0.28%. The shaded gray region represents the power spectra of 21 cm models from (Lidz et al., 2008) whose HI neutral fraction ranges from 0.21 to 0.82.

We eventually averaged the evaluated observed polarization fractions and, estimated  $\langle \gamma_{\text{obs}} \rangle = 0.28\%$ . As discussed in chapter 3, the leakage into the EoR spectrum is directly proportional

to the square of polarization fraction. Therefore, we used  $\langle \gamma_{\text{obs}} \rangle = 0.28\%$  and constrained the prediction in chapter 3 to be lower by 12% (Figure 4.24).

## 4.5 Discussions and Conclusions

We presented a 8640 square degrees, Stokes  $I$ ,  $Q$ ,  $U$  and  $V$  survey at 146.5 MHz carried out with the 128-element configuration of PAPER. The survey spans  $0^{\text{h}} < \text{RA} < 13^{\text{h}}$  and  $21^{\text{h}} < \text{RA} < 24^{\text{h}}$ , centered at a declination of  $-30^{\circ}43'12''$ . It reaches a confusion limit of 50 mJy in polarized intensity. Our results can be summarized as follows:

- we explored widefield imaging with low-frequency dipoles arrays that generated full-polarization images through an optimal weighting scheme. We estimated a conservative instrumental polarization fraction of 2.7% over a  $36^{\circ}$  field of view.
- we did not observe any point source emission, which might be due to Faraday dispersion leading to depolarization, but we leave it for future work.
- we constrained the observed polarization fraction to be 0.28% at 146.5 MHz that predicted the leakage into the EoR window from a population of point sources to be 12% less than the one predicted in chapter 3. This upper limit of the leakage power spectrum is at similar level as reported by [Ali et al. \(2015\)](#) for  $k > 0.15 \text{ hMpc}^{-1}$ .
- PAPER observations are found to be limited by polarization leakage at  $k > 0.15 \text{ h Mpc}^{-1}$  in contrast to [Asad et al. \(2016\)](#) who found that the polarization leakage in LOFAR observations is  $<10\%$ .

Table 4.2: Source Catalogue extracted from PAPER-128

Source ID	RA	DEC	Flux (Jy)
0002-3413	00 <sup>h</sup> 02 <sup>m</sup> 36 <sup>s</sup>	-34°13'24"	14.8 ± 0.9
J0003-1727	00 <sup>h</sup> 03 <sup>m</sup> 59 <sup>s</sup>	-17°34'48"	5.4 ± 1.2
J0015-3804	00 <sup>h</sup> 15 <sup>m</sup> 48 <sup>s</sup>	-38°56'59"	9.8 ± 0.8
J0020-2014	00 <sup>h</sup> 20 <sup>m</sup> 57 <sup>s</sup>	-20°49'07"	8.2 ± 0.9
J0024-2928	00 <sup>h</sup> 24 <sup>m</sup> 52 <sup>s</sup>	-29°31'55"	12.5 ± 0.7
J0025-2602	00 <sup>h</sup> 26 <sup>m</sup> 16 <sup>s</sup>	-25°01'29"	14.8 ± 0.7
J0025-3303	00 <sup>h</sup> 26 <sup>m</sup> 16 <sup>s</sup>	-33°58'14"	7.2 ± 0.7
0025-4135	00 <sup>h</sup> 25 <sup>m</sup> 15 <sup>s</sup>	-41°35'16"	19.8 ± 0.9
J0035-2003	00 <sup>h</sup> 35 <sup>m</sup> 39 <sup>s</sup>	-19°00'02"	11.7 ± 0.9
0038-1635	00 <sup>h</sup> 38 <sup>m</sup> 23 <sup>s</sup>	-16°35'56"	16.0 ± 1.2
J0038-3859	00 <sup>h</sup> 38 <sup>m</sup> 45 <sup>s</sup>	-38°01'14"	10.0 ± 0.8
0039-2734	00 <sup>h</sup> 39 <sup>m</sup> 36 <sup>s</sup>	-27°34'07"	8.8 ± 0.7
J0042-4414	00 <sup>h</sup> 42 <sup>m</sup> 18 <sup>s</sup>	-44°52'21"	17.7 ± 1.0
J0044-3530	00 <sup>h</sup> 45 <sup>m</sup> 00 <sup>s</sup>	-35°28'57"	7.8 ± 0.6
J0046-4207	00 <sup>h</sup> 46 <sup>m</sup> 25 <sup>s</sup>	-42°52'11"	25.7 ± 0.8
J0047-2517	00 <sup>h</sup> 48 <sup>m</sup> 02 <sup>s</sup>	-25°46'38"	15.3 ± 0.8
J0052-4306	00 <sup>h</sup> 52 <sup>m</sup> 23 <sup>s</sup>	-43°51'51"	16.0 ± 0.9
0103-2109	01 <sup>h</sup> 03 <sup>m</sup> 14 <sup>s</sup>	-21°09'24"	11.7 ± 0.8
J0105-4505	01 <sup>h</sup> 05 <sup>m</sup> 26 <sup>s</sup>	-40°04'53"	21.6 ± 0.9
0106-4004	01 <sup>h</sup> 06 <sup>m</sup> 44 <sup>s</sup>	-41°35'16"	19.8 ± 0.9
J0108-1604	01 <sup>h</sup> 08 <sup>m</sup> 53 <sup>s</sup>	-16°56'31"	23.1 ± 1.5
J0116-2052	01 <sup>h</sup> 17 <sup>m</sup> 25 <sup>s</sup>	-20°12'29"	13.1 ± 0.8
J0120-1520	01 <sup>h</sup> 21 <sup>m</sup> 03 <sup>s</sup>	-15°40'15"	21.6 ± 1.5
J0126-4048	01 <sup>h</sup> 27 <sup>m</sup> 07 <sup>s</sup>	-40°00'40"	10.8 ± 0.9
0129-3839	01 <sup>h</sup> 29 <sup>m</sup> 57 <sup>s</sup>	-38°39'49"	8.6 ± 0.9
J0130-2610	01 <sup>h</sup> 30 <sup>m</sup> 59 <sup>s</sup>	-26°50'38"	10.2 ± 0.8
0130-4009	01 <sup>h</sup> 30 <sup>m</sup> 28 <sup>s</sup>	-40°09'25"	11.2 ± 1.0
J0133-3629	01 <sup>h</sup> 34 <sup>m</sup> 16 <sup>s</sup>	-36°31'38"	21.5 ± 0.8

Source ID	RA	DEC	Flux (Jy)
J0141-2706	01 <sup>h</sup> 41 <sup>m</sup> 59 <sup>s</sup>	-27°54'23"	7.5 ± 0.8
J0142-1628	01 <sup>h</sup> 43 <sup>m</sup> 10 <sup>s</sup>	-16°30'32"	12.6 ± 1.2
0145-1600	01 <sup>h</sup> 45 <sup>m</sup> 02 <sup>s</sup>	-16°00'57"	71.8 ± 1.6
J0150-2932	01 <sup>h</sup> 51 <sup>m</sup> 01 <sup>s</sup>	-29°28'33"	8.3 ± 0.7
J0200-3053	02 <sup>h</sup> 00 <sup>m</sup> 38 <sup>s</sup>	-30°06'54"	17.6 ± 0.7
J0215-1259	02 <sup>h</sup> 16 <sup>m</sup> 22 <sup>s</sup>	-12°01'24"	34.7 ± 1.7
0216-4346	02 <sup>h</sup> 16 <sup>m</sup> 18 <sup>s</sup>	-43°46'04"	21.4 ± 1.5
J0219-3625	02 <sup>h</sup> 19 <sup>m</sup> 32 <sup>s</sup>	-36°27'06"	9.9 ± 1.0
J0223-2819	02 <sup>h</sup> 24 <sup>m</sup> 08 <sup>s</sup>	-28°41'56"	9.6 ± 1.0
J0225-2312	02 <sup>h</sup> 25 <sup>m</sup> 39 <sup>s</sup>	-23°46'47"	12.8 ± 1.0
J0225-2215	02 <sup>h</sup> 25 <sup>m</sup> 43 <sup>s</sup>	-22°45'01"	10.1 ± 1.0
J0237-1932	02 <sup>h</sup> 38 <sup>m</sup> 18 <sup>s</sup>	-19°30'48"	25.8 ± 1.5
J0312-1450	03 <sup>h</sup> 13 <sup>m</sup> 27 <sup>s</sup>	-14°11'52"	15.1 ± 1.4
J0312-4510	03 <sup>h</sup> 21 <sup>m</sup> 16 <sup>s</sup>	-45°42'53"	18.6 ± 1.6
J0320-3821	03 <sup>h</sup> 21 <sup>m</sup> 27 <sup>s</sup>	-38°46'48"	24.6 ± 1.8
J0322-3712	03 <sup>h</sup> 22 <sup>m</sup> 33 <sup>s</sup>	-37°57'57"	27.9 ± 1.4
J0346-3422	03 <sup>h</sup> 46 <sup>m</sup> 55 <sup>s</sup>	-34°37'01"	16.3 ± 1.6
J0351-2744	03 <sup>h</sup> 52 <sup>m</sup> 06 <sup>s</sup>	-27°16'28"	23.8 ± 1.6
J0351-1429	03 <sup>h</sup> 52 <sup>m</sup> 12 <sup>s</sup>	-14°30'00"	31.6 ± 1.6
J0429-3630	04 <sup>h</sup> 30 <sup>m</sup> 00 <sup>s</sup>	-36°26'20"	16.4 ± 1.6
0431-4518	04 <sup>h</sup> 31 <sup>m</sup> 22 <sup>s</sup>	-45°18'20"	13.0 ± 1.7
0434-4514	04 <sup>h</sup> 34 <sup>m</sup> 11 <sup>s</sup>	-45°14'07"	10.1 ± 1.6
J0438-4736	04 <sup>h</sup> 38 <sup>m</sup> 05 <sup>s</sup>	-47°31'04"	10.5 ± 1.3
0438-4754	04 <sup>h</sup> 38 <sup>m</sup> 55 <sup>s</sup>	-47°54'39"	19.0 ± 1.3
0440-4626	04 <sup>h</sup> 40 <sup>m</sup> 57 <sup>s</sup>	-46°26'01"	22.8 ± 1.5
0441-4408	04 <sup>h</sup> 41 <sup>m</sup> 15 <sup>s</sup>	-44°08'33"	16.0 ± 1.6
0441-4511	04 <sup>h</sup> 41 <sup>m</sup> 38 <sup>s</sup>	-45°11'19"	5.0 ± 0.7
J0444-2809	04 <sup>h</sup> 45 <sup>m</sup> 02 <sup>s</sup>	-28°49'17"	37.7 ± 1.6
0447-1230	04 <sup>h</sup> 47 <sup>m</sup> 51 <sup>s</sup>	-12°30'11"	13.7 ± 1.6
0448-1135	04 <sup>h</sup> 48 <sup>m</sup> 48 <sup>s</sup>	-11°35'33"	17.0 ± 1.4

Source ID	RA	DEC	Flux (Jy)
J0455-3006	04 <sup>h</sup> 55 <sup>m</sup> 48 <sup>s</sup>	-30°52'57"	18.3 ± 1.5
J0455-2034	04 <sup>h</sup> 55 <sup>m</sup> 57 <sup>s</sup>	-20°33'04"	16.9 ± 1.7
J0510-1838	05 <sup>h</sup> 11 <sup>m</sup> 12 <sup>s</sup>	-18°18'48"	18.0 ± 1.7
0520-4226	05 <sup>h</sup> 20 <sup>m</sup> 05 <sup>s</sup>	-42°26'44"	20.4 ± 1.7
0521-4326	05 <sup>h</sup> 21 <sup>m</sup> 24 <sup>s</sup>	-43°26'49"	16.0 ± 1.3
J0522-3627	05 <sup>h</sup> 23 <sup>m</sup> 14 <sup>s</sup>	-36°33'14"	46.2 ± 1.7
0525-4542	05 <sup>h</sup> 25 <sup>m</sup> 06 <sup>s</sup>	-45°42'29"	39.4 ± 1.5
J0627-3529	06 <sup>h</sup> 27 <sup>m</sup> 28 <sup>s</sup>	-35°28'10"	16.1 ± 1.6
J0636-2036	06 <sup>h</sup> 37 <sup>m</sup> 12 <sup>s</sup>	-20°24'35"	39.3 ± 1.6
J0658-2417	06 <sup>h</sup> 59 <sup>m</sup> 32 <sup>s</sup>	-24°43'17"	25.4 ± 1.6
0744-4558	07 <sup>h</sup> 44 <sup>m</sup> 31 <sup>s</sup>	-45°58'35"	8.5 ± 1.9
J0747-1917	07 <sup>h</sup> 48 <sup>m</sup> 04 <sup>s</sup>	-19°50'55"	29.0 ± 1.8
0752-4638	07 <sup>h</sup> 52 <sup>m</sup> 02 <sup>s</sup>	-46°38'09"	14.5 ± 1.4
J0824-4259	08 <sup>h</sup> 24 <sup>m</sup> 05 <sup>s</sup>	-43°52'20"	97.5 ± 1.9
J0827-2026	08 <sup>h</sup> 27 <sup>m</sup> 57 <sup>s</sup>	-20°33'29"	18.2 ± 1.8
0848-1313	08 <sup>h</sup> 48 <sup>m</sup> 39 <sup>s</sup>	-13°13'09"	14.5 ± 1.4
0848-4543	08 <sup>h</sup> 48 <sup>m</sup> 46 <sup>s</sup>	-45°43'14"	16.4 ± 1.7
0849-1352	08 <sup>h</sup> 49 <sup>m</sup> 34 <sup>s</sup>	-13°52'17"	38.9 ± 1.3
0859-4609	08 <sup>h</sup> 59 <sup>m</sup> 36 <sup>s</sup>	-46°09'46"	18.9 ± 1.9
J0859-4731	08 <sup>h</sup> 59 <sup>m</sup> 29 <sup>s</sup>	-47°22'04"	25.4 ± 1.1
J0901-2555	09 <sup>h</sup> 02 <sup>m</sup> 21 <sup>s</sup>	-25°03'38"	26.3 ± 1.8
0914-1248	09 <sup>h</sup> 14 <sup>m</sup> 45 <sup>s</sup>	-12°48'39"	24.5 ± 0.9
0917-4700	09 <sup>h</sup> 17 <sup>m</sup> 07 <sup>s</sup>	-47°00'33"	17.1 ± 1.9
0918-1520	09 <sup>h</sup> 18 <sup>m</sup> 17 <sup>s</sup>	-15°20'03"	21.5 ± 1.9
0859-4638	07 <sup>h</sup> 52 <sup>m</sup> 02 <sup>s</sup>	-46°38'09"	14.5 ± 1.4
0944-4739	09 <sup>h</sup> 44 <sup>m</sup> 23 <sup>s</sup>	-47°39'12"	38.9 ± 0.9
2333-4253	23 <sup>h</sup> 33 <sup>m</sup> 44 <sup>s</sup>	-42°53'02"	14.6 ± 1.3
J2334-4125	23 <sup>h</sup> 34 <sup>m</sup> 41 <sup>s</sup>	-41°41'14"	35.0 ± 1.2
2355-1734	23 <sup>h</sup> 55 <sup>m</sup> 57 <sup>s</sup>	-17°34'00"	14.8 ± 1.3
J2357-3455	23 <sup>h</sup> 57 <sup>m</sup> 18 <sup>s</sup>	-34°18'01"	19.8 ± 0.9

## CHAPTER 5

---

### General conclusions

---

*T*he Epoch of Reionization is a milestone in modern cosmology, and is the last major phase transition of the intergalactic medium from neutral to ionized. Amongst the various probes, the redshifted 21 cm line is acknowledged to be the most promising one as it probes different depths in the Universe’s history by retaining the redshift information ([Furlanetto et al., 2006](#); [McQuinn, 2016](#)). Various experiments are currently dedicated towards measuring the power spectrum of 21 cm Hydrogen line while others are looking to detect the globally averaged 21 signal. Measurements of the 21 cm Hydrogen line require exceptional sensitivity, control over systematic errors and exquisite calibration accuracy in order to separate foreground emission that is a few orders of magnitude brighter than the 21 cm emission.

This work primarily addresses the leakage due to instrumental widefield effects in visibility-based power spectra measured with redundant arrays, in particular, the Donald C. Baker Precision Array to Probe the Epoch of Reionization (PAPER). We have developed a framework whereby the delay-transform approach in ([Parsons et al., 2012](#)) has been extended to include all polarizations. We used the 32-element imaging configuration of PAPER to simulate realistic full-sky observations and construct polarized power spectra. We predicted the contamination due to a

population of point sources to be higher than diffuse Galactic polarized emission at all  $k$  modes for a 30 m baseline. However, even under the worst conditions, we could define a foreground-free window for diffuse Galactic emission at  $k > 0.3 h \text{ Mpc}^{-1}$ .

Furthermore, we analyzed 40 days of data from the last observing season of PAPER in order to image the sky region  $11^\circ < \text{DEC} < 46^\circ$  South and,  $0 \text{ h} < \text{RA} < 13 \text{ h}$  and  $21 \text{ h} < \text{RA} < 24 \text{ h}$  at 146.5 MHz at an angular resolution of 26 arcmins. We applied an optimal beam weighting scheme and combined all the snapshots 1.2 hours before and after the transit to form final Stokes images. The resulting Stokes  $I$  images were used to derive a catalogue of 88 compact sources down to a flux density of 5 Jy, covering about 8640 square degrees. The Stokes  $Q$  images were used to estimate the instrumental polarization of PAPER, which was found to be 2.7% under conservative conditions. In addition, they were utilized as inputs to the RM synthesis, and the upper limit to the observed point source polarized fraction was estimated to be 0.28%. This new upper limit, in turn, lowers our leakage (due to a population of point sources) prediction of the EoR power spectrum by 12%. However, the leakage caused by instrumental widefield effects still remain problematic as it is 1–2 orders higher than the desired 21 cm signal.

---

## Bibliography

---

Aguirre, J. A., Kohn, S. A., Martinot, Z. E., & Washington, I. Q. in prep.

Ali, Z. S., Parsons, A. R., Zheng, H., et al. 2015, *ApJ*, 809, 61

Alonso, D., Ferreira, P. G., & Santos, M. G. 2014, *MNRAS*, 444, 3183

Asad, K. M. B., Koopmans, L. V. E., Jelić, V., et al. 2015, *MNRAS*, 451, 3709

—. 2016, *MNRAS*, 462, 4482

Barkana, R., & Loeb, A. 2001, *Physics Report*, 349, 125

Barry, N., Hazelton, B., Sullivan, I., Morales, M. F., & Pober, J. C. 2016, *MNRAS*, 461, 3135

Beardsley, A. P., Hazelton, B. J., Sullivan, I. S., et al. 2016, *ApJ*, 833, 102

Becker, G. D., Bolton, J. S., & Lidz, A. 2015, *ArXiv e-prints*, arXiv:1510.03368

Bennett, J., Donahue, M., Schneider, N., & Voit, M. 2005, *The essential cosmic perspective*  
(Addison-Wesley)

Bernardi, G., Carretti, E., Cortiglioni, S., et al. 2003, *ApJ*, 594, L5

- Bernardi, G., Mitchell, D. A., Ord, S. M., et al. 2011, *MNRAS*, 413, 411
- Bernardi, G., de Bruyn, A. G., Brentjens, M. A., et al. 2009, *aap*, 500, 965
- Bernardi, G., de Bruyn, A. G., Harker, G., et al. 2010, *A&A*, 522, A67
- Bernardi, G., Greenhill, L. J., Mitchell, D. A., et al. 2013, *ApJ*, 771, 105
- Bernardi, G., Zwart, J. T. L., Price, D., et al. 2016, *MNRAS*, 461, 2847
- Bowman, J. D., Morales, M. F., & Hewitt, J. N. 2009, *ApJ*, 695, 183
- Bowman, J. D., & Rogers, A. E. E. 2010, *NAT*, 468, 796
- Brederode, L. R., van den Heever, L., Esterhuyse, W., & Jonas, J. L. 2016, in *Proceedings of the SPIE*, Vol. 9906, *Ground-based and Airborne Telescopes VI*, 990625
- Brentjens, M. A., & de Bruyn, A. G. 2005, *A&A*, 441, 1217
- Bridle, A. H. 1967, *MNRAS*, 136, 219
- Bromm, V. 2013, *Reports on Progress in Physics*, 76, 112901
- Burn, B. J. 1966, *MNRAS*, 133, 67
- Burns, J. O., Bradley, R., Tauscher, K., et al. 2017, *ApJ*, 844, 33
- Callingham, J. R., Ekers, R. D., Gaensler, B. M., et al. 2017, *ApJ*, 836, 174
- Cane, H. V. 1979, *MNRAS*, 189, 465
- Carretti, E., Bernardi, G., Sault, R. J., Cortiglioni, S., & Poppi, S. 2005, *MNRAS*, 358, 1
- Carretti, E., Haverkorn, M., McConnell, D., et al. 2010, *MNRAS*, 405, 1670
- Carroll, B. W., & Ostlie, D. A. 1996, *An Introduction to Modern Astrophysics*
- Chapman, E., Zaroubi, S., & Abdalla, F. 2014, *MNRAS*, arXiv:1408.4695

- Chapman, E., Bonaldi, A., Harker, G., et al. 2015, *Advancing Astrophysics with the Square Kilometre Array (AASKA14)*, 5
- Ciardi, B., & Ferrara, A. 2005, *SSR*, 116, 625
- Cohen, A. S., Lane, W. M., Cotton, W. D., et al. 2007, *AJ*, 134, 1245
- Condon, J. J., Cotton, W. D., Greisem, E. W., et al. 1998, *The astronomical Journal*, 115, 1693
- Conway, J. E., & Sault, R. J. 1995, *VLBI and the VLBA ASP Conference Series*, 82, 309
- Cornwell, T. J. and Golap, K., & Bhatnagar, S. 2005, *Astronomical Data Analysis Software and Systems XIV ASP Conference Series*, 347, 86
- Dai, S., Hobbs, G., Manchester, R. N., et al. 2015, *MNRAS*, 449, 3223
- de Bruyn, A. G., & Brentjens, M. A. 2005, *AAP*, 441, 931
- DeBoer, D. R., Parsons, A. R., Aguirre, J. E., et al. 2017, *PASP*, 129, 045001
- DeBreuck, C., van Breugel, W., Rttgering, H. J. A., & Miley, G. 2000, *A&A Supplement Series*, 143, 303
- Dijkstra, M. 2014, *PASA*, 31, e040
- Dillon, J. S., Liu, A., Williams, C. L., et al. 2014, *Physical Review D*, 89, 023002
- Dillon, J. S., Neben, A. R., Hewitt, J. N., et al. 2015, *PRD*, 91, 123011
- Douglas, J. N., Bash, F. N., Bozyan, F. A., Torrence, G. W., & Wolfe, C. 1996, *The Astronomical Journal*, 111, 1945
- Ewall-Wice, A., Dillon, J. S., Liu, A., & Hewitt, J. 2017, *MNRAS*, 470, 1849
- Ewall-Wice, A., Dillon, J. S., Hewitt, J. N., et al. 2016, *MNRAS*, 460, 4320
- Fan, X., Carilli, C. L., & Keating, B. 2006, *Annual Review of A&A*, 44, 415

Field, G. B. 1959, *ApJ*, 129, 536

Foley, A. 2010, in 10th European VLBI Network Symposium and EVN Users Meeting: VLBI and the New Generation of Radio Arrays, 69

Fuller, G. M., Mathews, G. J., & Alcock, C. R. 1988, *Physical Review D*, 37, 1380

Furlanetto, S. R., Peng, Oh, S., & Briggs, F. H. 2006, *Physics Reports*, 433, 181

Gaensler, B. M., Dickey, J. M., McClure-Griffiths, N. M., et al. 2001, *ApJ*, 549, 959

Gaensler, B. M., Haverkorn, M., Burkhart, B., et al. 2011, Low-Mach-number turbulence in interstellar gas revealed by radio polarization gradients, arXiv:1110.2896

Geil, P. M., Gaensler, B. M., & Wyithe, J. S. B. 2011, *MNRAS*, 418, 516

George, E. M., Reichardt, C. L., Aird, K. A., et al. 2015, *ApJ*, 799, 177

Ginzburg, V. L., & Syrovatskii, S. I. 1965, *Annual Review of Astronomy and Astrophysics*, 3, 297

Górski, K. M., Hivon, E., Banday, A. J., et al. 2005, *ApJ*, 622, 759

Grobler, T. L., Nunhokee, C. D., Smirnov, O. M., van Zyl, A. J., & de Bruyn, A. G. 2014, *MNRAS*, 439, 4030

Hamaker, J. P., Bregman, J. D., & Sault, R. J. 1996, *A&A Supplement*, 177, 137

Harker, G., Zaroubi, S., Bernardi, G., et al. 2009, *MNRAS*, 397, 1138

Haslam, C. G. T., Salter, C. J., Stoffel, H., & Wilson, W. E. 1982, *A&A Supplement*, 47, 1,2,4

Haverkorn, M., Katgert, P., & de Bruyn, A. G. 2003, *A&A*, 403, 1045

Heald, G. H., Pizzo, R. F., Orrú, E., et al. 2015, *AAP*, 582, A123

Hurley-Walker, N., Morgan, J., Wayth, R. B., et al. 2014, *PASA*, 31, e045

- Hurley-Walker, N., Callingham, J. R., Hancock, P. J., et al. 2017, *MNRAS*, 464, 1146
- Iacobelli, M., Haverkorn, M., & Katgert, P. 2013, *A&A*, 549, A56
- Iliev, I. T., Shapiro, P. R., McDonald, P., Mellema, G., & Pen, U.-L. 2008, *MNRAS*, 391, 63
- Jacobs, D. C., Parsons, A. R., Aguirre, J. E., et al. 2013, *ApJ*, 776, 108
- Jacobs, D. C., Pober, J. C., Parsons, A. R., et al. 2015, *ApJ*, 801, 51
- Jelić, V., Zaroubi, S., Labropoulos, P., et al. 2010, *MNRAS*, 409, 1647
- . 2008, *MNRAS*, 389, 1319
- Jelić, V., de Bruyn, A. G., Mevius, M., et al. 2014, *A&A*, 568, A101
- Jelić, V., de Bruyn, A. G., Pandey, V. N., et al. 2015, *A&A*, 583, A137
- Jeon, M. 2015, in *American Astronomical Society Meeting Abstracts*, Vol. 225, American Astronomical Society Meeting Abstracts, 318.06
- Johnston, S., Hobbs, G., Vigeland, S., et al. 2005, *MNRAS*, 364, 1397
- Kajantie, K., & Kurki-Suonio, H. 1986, *Physical Review D*, 34, 1719
- Kamionkowski, M. 2007, *ArXiv e-prints*, arXiv:0706.2986
- Kohn, S. A., Aguirre, J. E., Nunhokee, C. D., et al. 2016, *ApJ*, 823, 88
- Kolb, E., & Turner, M. 1994, *The early universe*, Vol. 69 (Westview press)
- Kolb, E. W., Linde, A., & Riotto, A. 1996, *Physical Review Letters*, 77, 4290
- Koopmans, L., Pritchard, J., Mellema, G., et al. 2015, *Advancing Astrophysics with the Square Kilometre Array (AASKA14)*, 1
- Kraus, J. D. 1966, *Radio Astronomy*, 1st edn. (USA: McGraw-Hill)
- La Porta, L., Burigana, C., Reich, W., & Reich, P. 2006, *A&A*, 455, L9

Lawson, K. D., Mayer, C. J., Osborne, J. L., & Parkinson, M. L. 1987, *MNRAS*, 225, 307

Lenc, E., Gaensler, B. M., Sun, X. H., et al. 2016, *ApJ*, 830, 38

Lenc, E., Anderson, C. S., Barry, N., et al. 2017, *PASA*, 34, e040

Lidz, A., Zahn, O., McQuinn, M., Zaldarriaga, M., & Hernquist, L. 2008, *ApJ*, 680, 962

Linde, A. 2008, in *Inflationary cosmology* (Springer), 1–54

Linder, C. C. 1990, *Particle physics and inflationary cosmology* (CRC Press)

Liu, A., Parsons, A. R., & Trott, C. M. 2014a, *PRD*, 90, 023018

—. 2014b, *PRD*, 90, 023019

Liu, A., Tegmark, M., Bowman, J., Hewitt, J., & Zaldarriaga, M. 2009, *MNRAS*, 398, 401

Lyth, D. H., & Stewart, E. D. 1995, *Physical Review Letters*, 75, 201

Madau, P., Meiksin, A., & Rees, M. J. 1997, *ApJ*, 475, 429

Malaney, R. A., & Mathews, G. J. 1993, *Physics Reports*, 229, 145

Mathews, G. J., Meyer, B. S., Alcock, C. R., & Fuller, G. M. 1990, *The Astrophysical Journal*, 358, 36

Matteo, Di, T., Perna, R., Abel, T., & Rees, J. M. 2002, *ApJ*, 564, 576

McQuinn, M. 2016, *ARAA*, 54, 313

McQuinn, M., Zahn, O., Zaldarriaga, M., Hernquist, L., & Furlanetto, S. R. 2006, *ApJ*, 653, 815

Mellema, G., Iliev, I. T., Pen, U.-L., & Shapiro, P. R. 2006, *MNRAS*, 372, 679

Mesinger, A., Furlanetto, S., & Cen, R. 2011, *MNRAS*, 411, 955

Mitchell, D. A., Greenhill, L. J., Wayth, R. B., et al. 2008, *IEEE Journal of Selected Topics in Signal Processing*, 2, 707

- Mohan, N., & Rafferty, D. 2015, PyBDSM: Python Blob Detection and Source Measurement, Astrophysics Source Code Library, ascl:1502.007
- Monsalve, R. A., Rogers, A. E. E., Bowman, J. D., & Mozdzen, T. J. 2017, ApJ, 847, 64
- Moore, D., Aguirre, J. E., Kohn, S., et al. 2015, ArXiv e-prints, arXiv:1502.05072
- Moore, D. F., Aguirre, J. E., Parsons, A. R., Jacobs, D. C., & Pober, J. C. 2013, ApJ, 769, 154
- Morales, M. F., Bowman, J. D., & Hewitt, J. N. 2006, ApJ, 648, 767
- Morales, M. F., & Hewitt, J. 2004, ApJ, 615, 7
- Morales, M. F., & Matejek, M. 2009, MNRAS, 400, 1814
- Mortlock, D. J. 2015, ArXiv e-prints, arXiv:1511.01107
- Mulcahy, D. D., Horneffer, A., Beck, R., et al. 2014, A&A, 568, A74
- Noordam, J. E., & Smirnov, O. M. 2010, AAP, 524, A61
- Offringa, A. R., McKinley, B., Hurley-Walker, N., et al. 2014, WSClean: Widefield interferometric imager, Astrophysics Source Code Library, ascl:1408.023
- Offringa, A. R., Trott, C. M., Hurley-Walker, N., et al. 2016, MNRAS, 458, 1057
- Ord, S. M., Mitchell, D. A., Wayth, R. B., et al. 2010, PASP, 122, 1353
- Paciga, G., Chang, T.-C., Gupta, Y., et al. 2011, MNRAS, 413, 1174
- Paciga, G., Albert, J. G., Bandura, K., et al. 2013, MNRAS, 433, 639
- Parsons, A. R., & Backer, D. C. 2009, ApJ, 138, 219
- Parsons, A. R., Pober, J. C., Aguirre, J. E., et al. 2012, ApJ, 756, 165
- Parsons, A. R., Backer, D. C., Foster, G. S., et al. 2010, A.J., 139, 1468
- Parsons, A. R., Liu, A., Aguirre, J. E., et al. 2014, ApJ, 788, 106

- Patil, A. H., Zaroubi, S., Chapman, E., et al. 2014, *MNRAS*, 443, 1113
- Patil, A. H., Yatawatta, S., Zaroubi, S., et al. 2016, *MNRAS*, 463, 4317
- Patil, A. H., Yatawatta, S., Koopmans, L. V. E., et al. 2017, *ApJ*, 838, 65
- Patra, N., Subrahmanyam, R., Raghunathan, A., & Udaya Shankar, N. 2013, *Experimental Astronomy*, 36, 319
- Pentericci, L., Vanzella, E., Fontana, A., et al. 2014, *ApJ*, 793, 113
- Petrovic, N., & Oh, S. P. 2011, *MNRAS*, 413, 2103
- Pindor, B., Wyithe, J. S. B., Mitchell, D. A., et al. 2011, *PASA*, 28, 46
- Planck Collaboration. 2015, *ArXiv e-prints*, arXiv:1506.07135
- Planck Collaboration, Ade, P. A. R., Aghanim, N., et al. 2016a, *AAP*, 594, A13
- Planck Collaboration, Adam, R., Aghanim, N., et al. 2016b, *AAP*, 596, A108
- Pober, J. C., Parsons, A. R., Aguirre, J. E., et al. 2013, *The ApJ Letters*, 768, L36
- Price, D. C., Greenhill, L. J., Fialkov, A., et al. 2017, *ArXiv e-prints*, arXiv:1709.09313
- Pritchard, J., & Loeb, A. 2010, *Nature*, 468, 772773
- Pritchard, J. R., & Furlanetto, S. R. 2007, *MNRAS*, 376, 1680
- Pritchard, J. R., & Loeb, A. 2012, *Reports on Progress in Physics*, 75, 086901
- Procopio, P., Wayth, R. B., Line, J., et al. 2017, *PASA*, 34, e033
- Rafelski, J., & Birrell, J. 2014, in *Journal of Physics Conference Series*, Vol. 509, *Journal of Physics Conference Series*, 012014
- Reich, P., & Reich, W. 1988, *Astronomy and Astrophysics Supplement Series*, 74, 7
- Rengelink, R. B., Tang, Y., de Bruyn, A. G., et al. 1997, *AAPS*, 124, doi:10.1051/aas:1997358

- Santos, M. G., Cooray, A., & Knox, L. 2005, *ApJ*, 625, 575
- Sather, E. 1996, *Beam Line*, 26, 31
- Schnitzeler, D. H. F. M., Katgert, P., & de Bruyn, A. G. 2009, *ApJ*, 494, 611
- Seo, H.-J., & Eisenstein, D. J. 2005, *ApJ*, 633, 575
- Shaver, P. A., Windhorst, R. A., Madau, P., & de Bruyn, A. G. 1999, *A&A*, 345, 380
- Singh, S., Subrahmanyan, R., Udaya Shankar, N., et al. 2017, *ArXiv e-prints*, arXiv:1710.01101
- Smirnov, O. M. 2011a, *A&A*, 527, A106
- . 2011b, *AAP*, 527, A108
- Sokolowski, M., Tremblay, S. E., Wayth, R. B., et al. 2015, *PASA*, 32, e004
- Stark, D. P., Ellis, R. S., & Ouchi, M. 2011, *ApJ*, 728, L2
- Stefan, I. I., Carilli, C. L., Green, D. A., et al. 2013, *MNRAS*, 432, 1285
- Sullivan, I. S., Morales, M. F., Hazelton, B. J., et al. 2012, *ApJ*, 759, 17
- Taylor, A. R., Stil, J. M., & Sunstrum, C. 2009, *ApJ*, 702, 1230
- Tegmark, M., Eisenstein, D. J., Strauss, M. A., et al. 2006, *Physical Review D*, 74, 123507
- Thompson, A. R., Moran, J. M., & Swenson Jr, G. W. 2008, *Interferometry and synthesis in radio astronomy* (John Wiley & Sons)
- Thyagarajan, N., Parsons, A. R., DeBoer, D. R., et al. 2016, *ApJ*, 825, 9
- Thyagarajan, N., Udaya Shankar, N., Subrahmanyan, R., et al. 2013, *ApJ*, 776, 6
- Thyagarajan, N., Jacobs, D. C., Bowman, J. D., et al. 2015, *ApJ*, 807, L28
- Tingay, S. J., Goetze, R., Bowman, J. D., et al. 2013, *PASA*, 30, e007

- Trac, H., & Cen, R. 2007, *ApJ*, 671, 1
- Trac, H. Y., & Gnedin, N. Y. 2011, *Advanced Science Letters*, 4, 228
- Tribble, P. C. 1991, *MNRAS*, 250, 726
- Trott, C. M., Pindor, B., Procopio, P., et al. 2016, *ApJ*, 818, 139
- van Haarlem, M. P., Wise, M. W., Gunst, A. W., et al. 2013, *A&A*, 556, A2
- Vedantham, H., Udaya Shankar, N., & Subrahmanyam, R. 2012, *ApJ*, 745, 176
- Wang, X., Tegmark, M., Santos, M. G., & Knox, L. 2006, *ApJ*, 650, 529
- Wielebinski, R., & Shakeshaft, J. R. 1962, *NAT*, 195, 982
- Wieringa, M. H., de Bruyn, A. G., Jansen, D., Brouw, W. N., & Katgert, P. 1993, *A&A*, 268, 215
- Wouthuysen, S. A. 1952, *A.J.*, 57, 31
- Wright, A., & Otrupcek, R. 1990, in *PKS Catalog (1990)*, 0
- Yatawatta, S., de Bruyn, A. G., Brentjens, M. A., et al. 2013, *AAP*, 550, A136
- Yoshida, N., Hosokawa, T., & Omukai, K. 2012, *Progress of Theoretical and Experimental Physics*, 2012, 01A305
- Zaldarriaga, M., Furlanetto, S. R., & Hernquist, L. 2004, *ApJ*, 608, 622
- Zaroubi, S. 2013, in *Astrophysics and Space Science Library*, Vol. 396, *The First Galaxies*, ed. T. Wiklind, B. Mobasher, & V. Bromm, 45
- Zaroubi, S., de Bruyn, A. G., Harker, G., et al. 2012, *MNRAS*, 425, 2964
- Zheng, H., Tegmark, M., Buza, V., et al. 2014, *MNRAS*, 445, 1084
- Zheng, Q., Wu, X.-P., Gu, J.-H., Wang, J., & Xu, H. 2012, *MNRAS*, 424, 2562